

SELF-ASSEMBLY, GRAPHENE AND APPLICATIONS

A Dissertation

Presented to the Faculty of the Graduate School

of Cornell University

In Partial Fulfillment of the Requirements for the Degree of

Doctor of Philosophy

by

Wei Min Chan

February 2016

© 2016 Wei Min Chan

SELF-ASSEMBLY, GRAPHENE AND APPLICATIONS

Wei Min Chan, PhD

Cornell University 2016

Investigation of new fabrication techniques and materials properties are necessary to overcome power and cost constraints facing contemporary electronics as well as enabling new functionality. In this thesis, several experiments to investigate directed self-assembly and the unique properties of plasmons in graphene are described. We first introduce a method to reduce the inherent trade-off in dimension vs geometry present in block copolymer self-assembly. Next we show that the electronic properties of graphene vary from sample to sample and develop a dry transfer technique to reduce the effect of water at the substrate interface. We apply these techniques to investigate the dispersion of confined graphene plasmons in the far-IR. Using self-assembly we extend the frequency of the graphene plasmons into the mid-IR where we directly measure the losses due to phonon coupling and also observe an induced transparency. Finally we present measurements of the performance of a molybdenum disulphide photodetector. These experiments have contributed to our ability to fabricate nanoscale structures, improve the controllability as well as our understanding of the properties of new two dimensional materials.

BIOGRAPHICAL SKETCH

Wei Min was born in Penang Malaysia and went to Union Primary School and Chung Ling high school before attending Cornell University. There he studied Electrical and Computer Engineering. As an undergraduate, he participated in the underwater autonomous vehicle team as well as the orientation steering committee. In his senior year he developed an interest in semiconductors which led to the group of Professor Sandip Tiwari. There, Wei Min studied self-assembly and graphene plasmonics as well as theoretical computer science.

Dedicated to my parents

ACKNOWLEDGMENTS

This thesis would not have been possible without the guidance of my advisors and colleagues at Cornell who have accompanied me during my PhD through my trials and tribulations and to whom I am extremely grateful. I wish to thank Professor Sandip Tiwari for giving me the opportunity to develop as a researcher and for his example to always question with an open mind and avoid groupthink. Next I would like to thank Professor Farhan Rana for letting me work in his group and always encouraging us to be rigorous and fast. I would also like to thank Professor David Steurer and Prof Robert Buhman for agreeing to serve on my committee. Finally I would like to thank Charles Black, Derek Stewart and Christina Manolatu for giving me the chance to work with them.

I have been lucky enough to have worked with some of the brightest people and so I would like to thank in no particular order Ravishankar Sundaraman, Shriram Shivaraman, Jared Strait, Parinita Nene, Haining Wang, Arvind Kumar, Professor Ali Gokirmak, Professor Sufei Shi, Katy Bosworth, Evan Schwartz, Joshua Rubin, Jaeyoon Kim, MoonKyung Kim, Professor Dana Weinstein, Mark Levendorf, Hengky Chandrahahim, Norimasa Yoshimizu, Laura Faguely, Tiffany Cheng, Professor Alper Bozkurt, Professor Omeed Momeni, Hadi Hosseinzadegan, Rajeev Dokania, Xiao Wang, Suresh Sidaran, Lola Brown, Professor Arend van der Zande, Professor Kin Fai Mak, Amit Pharkya, Erdal, Yilmaz, Professor Yuerui Lu, Paul George, Professor Jahan Dawlaty, Faisal Ahmad, Obafemi Otaleja, Siva Pulla, Sarvani and everyone else for all the late nights in the lab.

I would like to thank Scott Coldren and Patricia Gonyea in the electrical and computer engineering department as well as John Treichler, Gary Bordonaro, Alan Bleier, Vince Genova, Michael Skarvla, Aaron Windsor and all the staff in the CCMR and CNF.

Finally this list would not be complete without thanking my parents and friends for all their love and support throughout the years.

TABLE OF CONTENTS

1.	Introduction	
2.	Directed Self-Assembly	
	2.1 Introduction	5
	2.2 Directed Self-Assembly Process	5
	2.3 Order Parameters	6
	2.4 Overcoming the trade-off between Geometry and Dimensions	12
3.	Graphene properties	
	3.1 Electrical Properties	16
	3.2 Mechanical Properties	19
	3.3 Wetting Properties	20
	3.4 Processing of Graphene	
	3.4.1 Graphene Exfoliation	21
	3.4.2 CVD Graphene	22
	3.4.3 Graphene Dry Transfer	25
	3.5 Graphene FETs	28
	3.6 FTIR Spectroscopy of Graphene	32
4.	Graphene plasmons in the far-IR	
	4.1 Introduction	35
	4.2 Device Fabrication	36
	4.3 Drude Model of Graphene Plasmons	40
5.	Graphene plasmons in the mid-IR	
	5.1 Introduction	55
	5.2 Self-Assembly Process for Plasmon Resonators	55
	5.3 Contribution to Damping from Self-Assembly Process	57
	5.4 Contribution to Damping from Phonon Coupling	62
	5.4.1 Damping from Substrate Phonons	66
	5.4.2 Damping from Graphene Phonons	68
	5.5 Phonon Induced Transparency in Graphene	71
6.	Time resolved measurements of Molybdenum Disulphide	
	6.1 Introduction	77
	6.2 TPCC Measurement	77
	6.3 Model of Molybdenum Disulphide Junction	81
	6.4 Conclusion	83

CHAPTER 1

INTRODUCTION

It is arguable that modern electronics is dominated by silicon technology mainly because of the silicon to silicon dioxide interface[1]. This interface can be formed at reasonable cost and supports a high mobility while allowing electrostatic control of the transistor channel. The second enabler was the ability to create controllable geometries out of silicon and to scale the fabrication infrastructure as well as the device dimensions with time therefore achieving better performance in terms of density, speed and cost[2]. There are several challenges to continued scaling of silicon technology.

The fundamental limitation to continued scaling is power[3]. In the past constant field scaling and now general scaling have kept power in check as feature sizes have shrunk by scaling the threshold voltage correspondingly. In order to preserve the on off ratio of cmos devices, the threshold voltage is limited by the sub-threshold swing which is 60mV/dec. The second issue is as the channel length shrinks, the gate has to be brought closer to the channel to compensate for the loss of electrostatic control. Ignoring gate leakage, the gate dielectric thickness is limited by the distance of the charge centroid from the interface due to the triangular well confinement of the 2DEG. Lastly as feature sizes has shrunk, there has been diminishing returns in terms of transistor speed since the mean free path of carriers in silicon is approximately 10nm. Hence the recent focus on applying strain to silicon such that more electrons occupy the valleys with lower

effective mass. If the gate length cannot be scaled anymore then density scaling will eventually be limited by the minimum drain source overlap.

Our ability to define features at the nanoscale is limited by cost. The main limiting tool used to define geometry at nanoscale is optical lithography, which is a parallel write technique. To resolve smaller dimensions, light of smaller wavelengths has to be used. Currently, extreme ultraviolet (EUV) light with a wavelength of 13.5nm is proposed for further CMOS scaling[4]. Since the electrons generated by photons inside the photoresist have a diffusion length, there is a lower limit to the resolution that can be achieved lithographically. The light source for euv lithography does not have the output power necessary to be economical. The other candidate to further scaling is multiple patterning, however the cost of multiple patterning is high and has very strict overlay requirements. Furthermore as devices get smaller process variations begin to dominate the electrical characteristics of each device. The threshold voltage is particularly sensitive to process variation due to short channel effects. For all these reasons, there is an incentive to examine materials and technologies, which may complement cmos and/or enable new devices.

Chapter 1 discusses self-assembly, a technology which enables us to produce dense nanoscale feature over large areas at low cost. The trade-off is that self-assembly is limited to very specific geometries. We apply orthogonal chemistry to self-assembly to reduce this trade-off since the design rule space will be severely restricted otherwise.

We demonstrate using our technique two different feature sizes on the same layer as well as the ability to perform additive and subtractive patterning.

In the following chapters we examine graphene, which is the first two-dimensional material isolated experimentally in 2004. It is difficult to identify and produce new materials with any combination of desired properties which among others included a high intrinsic mobility, a direct band gap and optical transparency hence the intense efforts in the following years by industry and academic research groups into ways to produce graphene, fabricate devices and investigate the mechanisms behind the device operation. Graphene is not suitable for conventional CMOS electronics. We know that in materials increasing the orbital overlap shall reduce the effective mass while decreasing the bandgap so most materials sit on a line with mobility inversely proportional to the bandgap. This is true for graphene as well, attempts to engineer a band gap into graphene for digital electronics have resulted in lower mobility than $1000 \text{ cm}^2/\text{Vs}$. Graphene mobility comes from the pi-bonds on its surface while a high capacitance comes from the dielectric polarization, so it is difficult to realize high mobility in the high field region. The contact resistance of graphene is very high, limited by current crowding as well as the low density of states near the Fermi level.

The THz region of the electromagnetic spectrum is of interest for sensing since many compounds exhibit a unique fingerprint in this region. One potential route is via plasmonics using high mobility materials. Plasmons allow strong confinement of light and this can be observed by comparing the dispersion curve of plasmons in different

materials to the dispersion of light in vacuum, for a given frequency the wavenumber of the plasmon is usually higher than the wavenumber of light in vacuum. Specifically, we investigate graphene plasmonic devices including how to fabricate them, their damping mechanisms and how to extend them into the mid-ir region. Previously plasmonic devices were made from metals, which have a low mobility and hence small damping time. Graphene plasmonics have a high mobility as well as tunability via electrostatic or chemical doping. In chapter 2 we introduce the material properties of graphene and techniques we use to fabricate and measure graphene plasmons. In chapter 3 we examine graphene plasmons in the far-ir and show that confined plasmons do not obey the bulk plasmon dispersion curve and introduce a drude model that more accurately describes the experimental data. We also show that the coupling of plasmons in graphene structures is significant. Finally in chapter 4 we put everything together by applying self-assembly to fabricate graphene plasmon resonators operating in the mid-ir and examine their damping due to phonon coupling.

CHAPTER 2

DIRECTED SELF-ASSEMBLY

2.1 Introduction

As discussed in the previous chapter, optical lithography is limited by the wavelength of available light sources and the accompanying optics. The formula for the resolvable resolution is given by $CD = k \frac{\lambda}{NA}$ where NA is the numerical aperture of the objective, k models the process such as proximity and photoresist and λ is the wavelength of the light source. Electron beam lithography on the other hand can exceed this limit since the wavelength of a high energy electron can be much smaller than the wavelength of an optical photon. However electron beam lithography is a sequential write technique and furthermore the tail of an electron is much longer than a photon typically in microns range, hence obtaining dense features is challenging.

2.2 Directed Self-Assembly Process

Self-organization has been suggested as a possible path to getting small dimensions where conventional optical lithography approaches break down[5,6]. We have explored BCP approaches which allow different periodic structural forms and dimensions between 5-50nm. Perpendicularly standing pore arrays of copolymer film are formed when the surface is energy neutral. This results in absence of preferential wetting from either block [7]. We graft the random copolymer to the substrate by annealing it in vacuum for 24 hours followed by rinsing with toluene to remove the excess random copolymers, forming a polymer brush on the surface. Polystyrene block co-methyl

methacrylate (PS(68k)-b-PMMA(33.5k)) is then spun coated at spin speeds from 1krpm to 5krpm onto the surface and annealed in vacuum at 180°C for 10 hours. Since toluene has a low vapor pressure, the concentration of the block copolymer solution is not stable and hence the thickness of the film varies. By spinning a range of thicknesses we can observe a trend using electron microscopy and determine the correct spin speed to obtain the thickness we want. Typically a trend can be observed as the film thickness varies unless the film dewets from the surface. In this instance the block copolymer film will form blobs and there will be no self-assembled pattern. If this happens the annealing oven and solution has to be investigated for contamination and the wafer surface as well as all labware has to be checked for cleanliness. A typical clean would be sonication in acetone and ipa followed by oxygen plasma. The raised temperature imparts mobility to the polymer. The polystyrene (PS) and poly(methyl methacrylate) (PMMA) blocks are covalently bonded to each other but are also immiscible to each other. In the presence of thermal energy, periodic array results from this repulsion. After the film has assembled we cross-link the PS and degrade the PMMA by deep ultraviolet exposure. The PMMA block can then be removed by rinsing in acetic acid. We now have a PS mask with a periodic array of holes.

2.3 Order Parameters

The periodic arrays have been analyzed in this effort to determine their order parameters. Figure 2.1 shows an example with $\text{area}_{\text{SEM}} \approx 3238.7 \times \text{area}_{\text{pore}}$. If for some reason there are regions on the substrate where the surface energy is not neutral there will be preferential wetting by one of the blocks. First we wish to quantify how many

PMMA cylinders are aligned parallel instead of perpendicular to the substrate due to this preferential wetting and also the spread in the center to center distance or domain spacing between all pores. In order to find the spread in the domain spacing, we use triangulation to first identify all the edges between pores. Figure 2.2 shows a histogram of all the edges. To quantify the defects in our sample, e.g., the places where we observe cylinders parallel instead of perpendicular pores we plot pores which are connected (Figure 2.3). Finally we calculate the translational and orientation correlation lengths. We observe from the Fourier transform of the micrograph (Figure 2.1 inset) that the intensity forms a ring denoting a more isotropic than crystalline ordering. Hence we use $|\vec{r}_0 - \vec{r}_1|$ as our order parameter for translational correlation. We calculate the distance between all pairs of pores, histogram using a bin size of 4 nm and plot the normalized distribution as 'o' in Figure 4. The order parameter for the orientation correlation is $\psi(\vec{r}) = e^{i6\theta(\vec{r})}$ [8]. We calculate for all pairs of pores, $\langle \psi(\vec{r}_0)\psi'(\vec{r}_1) \rangle$, ignoring dislocations with five or seven fold vertices and plot it in Figure 2.4 as ' Δ '. Finally to determine the translational and orientation correlation lengths we fit the translational correlation to $Ae^{-r/\xi_{tr}} + C$ and the orientation correlation to $Ae^{-r/\xi_{or}}$. The translational correlation length, ξ_{tr} is 52.63nm and the orientation correlation length ξ_{or} is 113.64nm. This points to largely a short range order.

The reason the PMMA block may have toppled over could be because it is too thick as the influence of the brush decays exponentially normal to the surface or that the brush did not anchor properly on the substrate at those points. We observe that with reference to the mean distance in Figure 1 the grain size is approximately 5-6 times the domain

spacing. The correlation length in BCP films grow with time under annealing due to topological defect annihilation at the grain boundaries causing the grain sizes to grow according to $\xi(t) \propto t^\gamma$, where the growth exponent γ is dependent upon molecular mobility [9]. By increasing the annealing time or by using techniques such as chemically pre-patterning the substrate, the grain sizes could be extended to several micro-meters, it has been argued that this approach reduces the annealing time as well because the molecules are oriented locally and do not have to move much [10]. We conclude that our BCP film is suitable for fabricating a device which is periodic over a distance of approximately 200nm and has a smallest dimension of around 20nm.

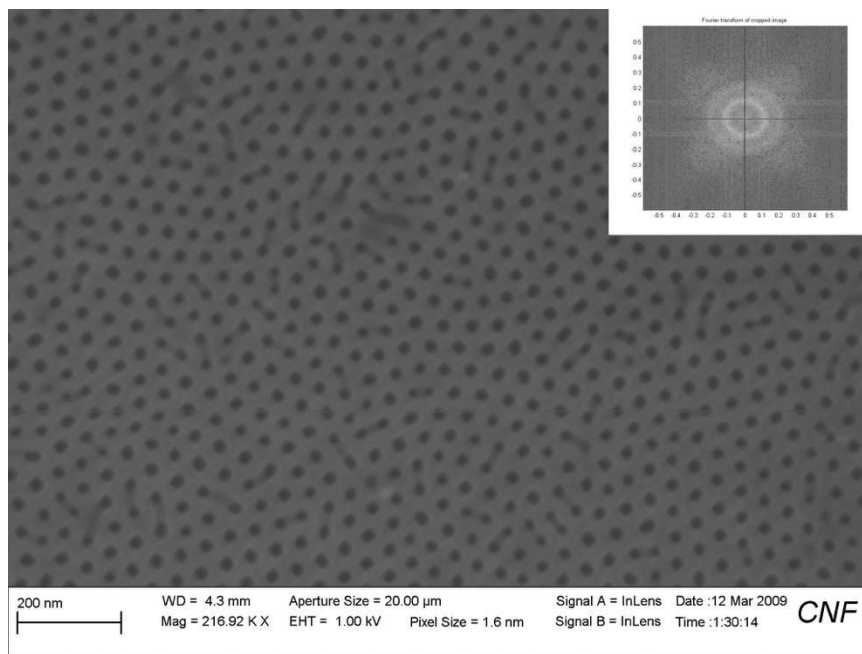


Figure 2.1: SEM picture of self-assembled PS-b-PMMA film, the black dots are the removed 36nm PMMA domains and the lighter region is the PS scaffold. The inset is a fourier transform of the SEM image indicating short range order.

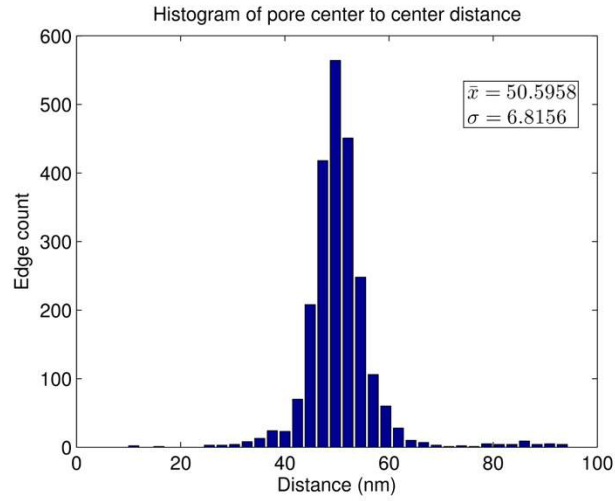


Figure 2.2 Histogram of center to center distance of two PMMA domains with mean 50.6nm and sigma of 6.8nm calculated by forming Delaunay triangulation and averaging over the edge lengths.

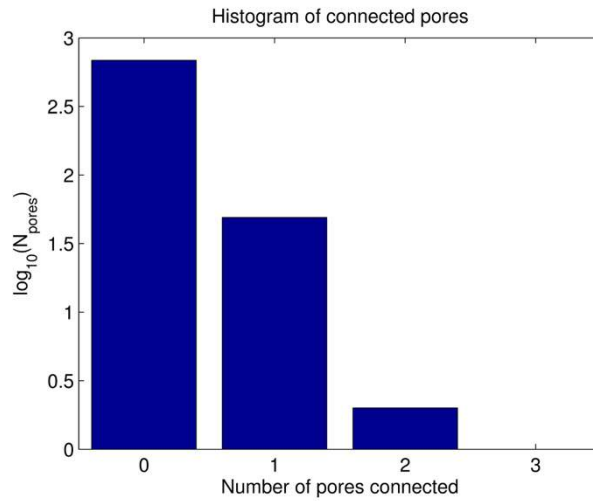


Figure 2.3: Histogram of connected pores indicating number of defects in the film

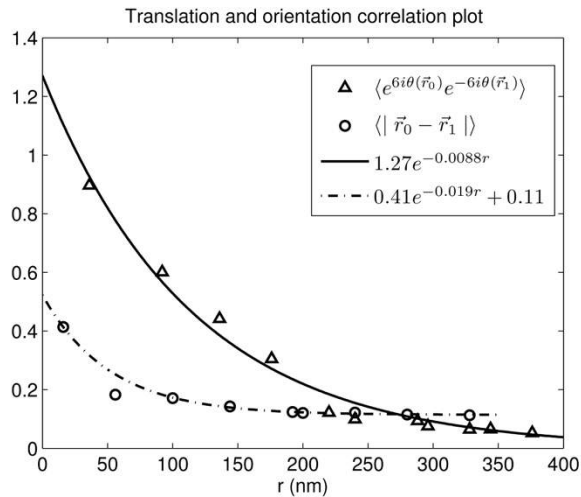


Figure 2.4: Plot showing the translation and orientation order parameters, obtained by averaging over all pairs of pores. The translation correlation length is 52.63nm and the orientation correlation length is 113nm.

The ability of self-assembly to form nanoscale structures beyond lithographic limits at low cost is of great interest, however there is a significant trade-off because block copolymer lithography is constrained to certain periodic geometries such as shown in the figure 2.5.

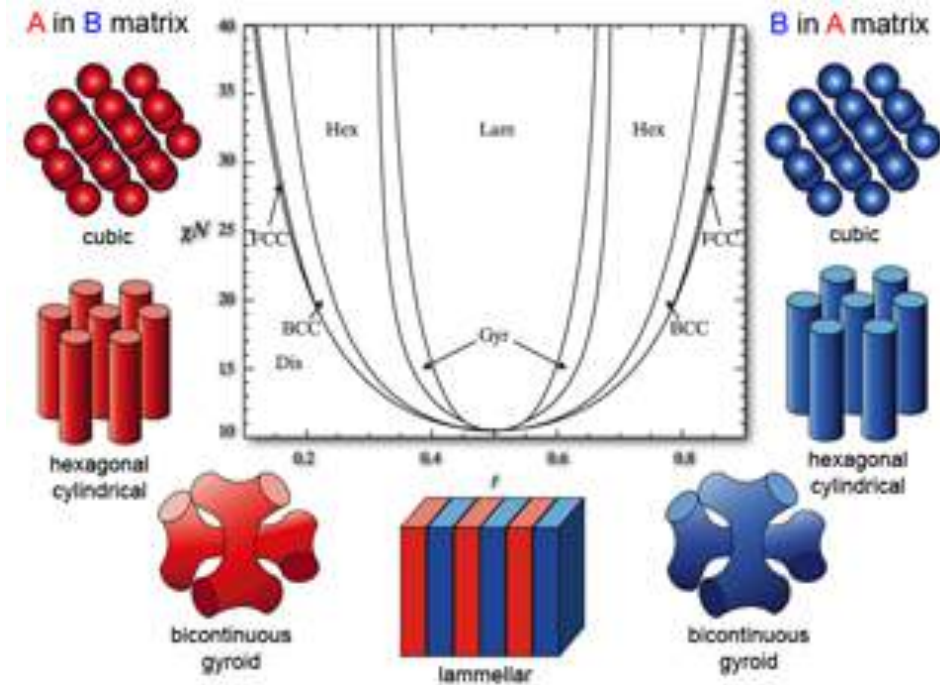


Figure 2.5: Phase transition diagram of diblock copolymers showing morphology as a function of florry huggins interaction parameter on the y-axis and volume fraction of the different blocks on the x-axis

In terms of the feature sizes, the sizes are bounded from below by the florry huggins interaction parameter and bounded from above by the mobility of the polymer chains as their molecular weight becomes large. The expression for feature size is given by[11]:

$$(2.1) \quad L_0 \propto a_0 N^{2/3} \chi^{1/6}$$

where a_0 is the monomer length usually around 0.7nm, N is the degree of polymerization and χ is the florry huggins interaction parameter which depends on the block copolymer. We plot the feature size vs molecular weight in the figure 2.6.

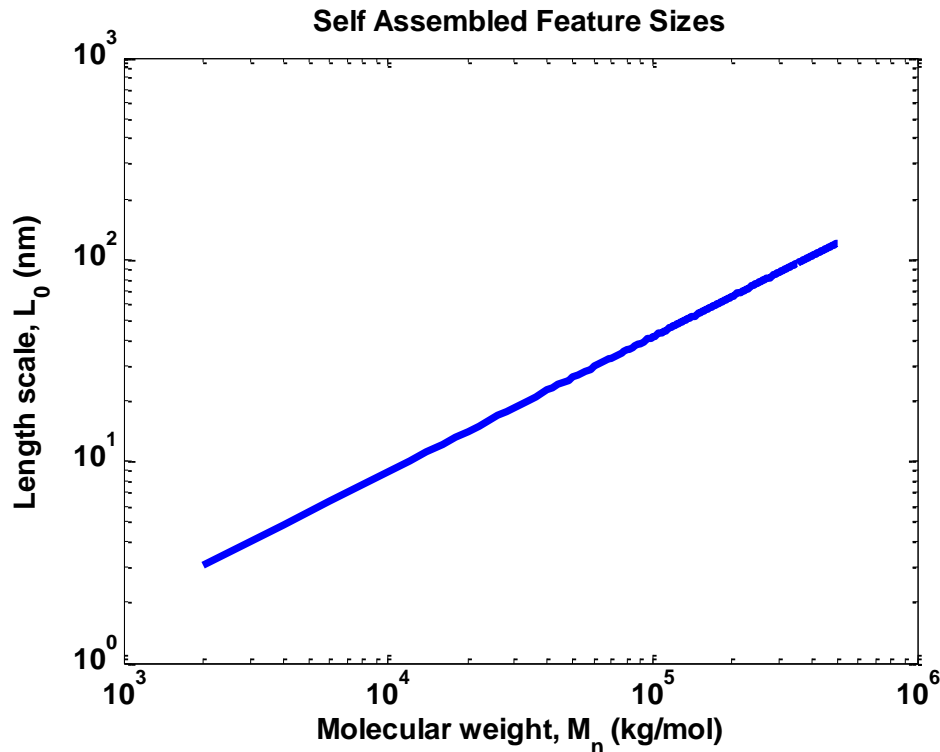


Figure 2.6: Plot of feature sizes as a function of molecular weight of the block copolymer chain

2.4 Overcoming the trade-off between Geometry and Dimensions

One way around the trade-off of restricted geometries is via orthogonal chemistry. Usually solvents are divided into polar and non-polar solvents and by tuning the degree of polarity we can ensure that both blocks of the block copolymer are miscible in the solvent for spin-coating. However by utilizing the functional group of the solvent in this case fluorine we are afforded a third degree of freedom in the form of hydroflouroethers (HFE)[12]. Combining hydroflouroethers with photoresists (OSCoR) miscible in them allows us to perform subtractive and additive patterning on block copolymer films. The process is summarized in the figure 2.7:

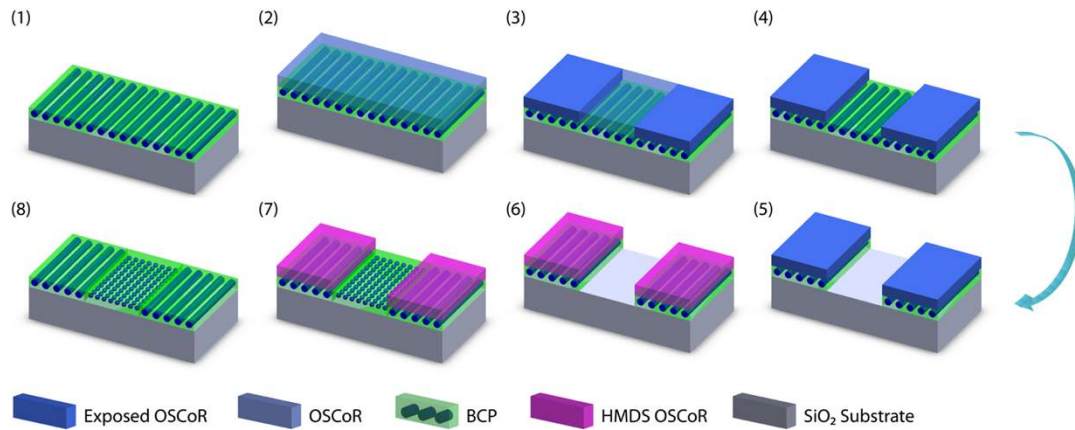


Figure 2.7: Process flow for orthogonal processing of block copolymers: 1) Deposit first block copolymer (BCP1), solvent anneal, crosslink 2) Deposit semi-fluorinated resist (OSCoR) on BCP1 3) Expose OSCoR to ultraviolet irradiation ($\lambda=365\text{nm}$), 4) Develop and remove unexposed OSCoR with fluorous solvent, 5) Etch underlying BCP1 with O_2 plasma to expose SiO_2 substrate, 6) hexamethyldisilazane (HMDS) vapor prime to restore OSCoR solubility to previously exposed regions, 7) Spin coat second block copolymer (BCP2), 8) Lift off OSCoR, solvent anneal BCP2.[13]

The challenge with this approach is that during the initial experiments a change in morphology was observed after removing the photoresist film as shown in the figure 2.8.

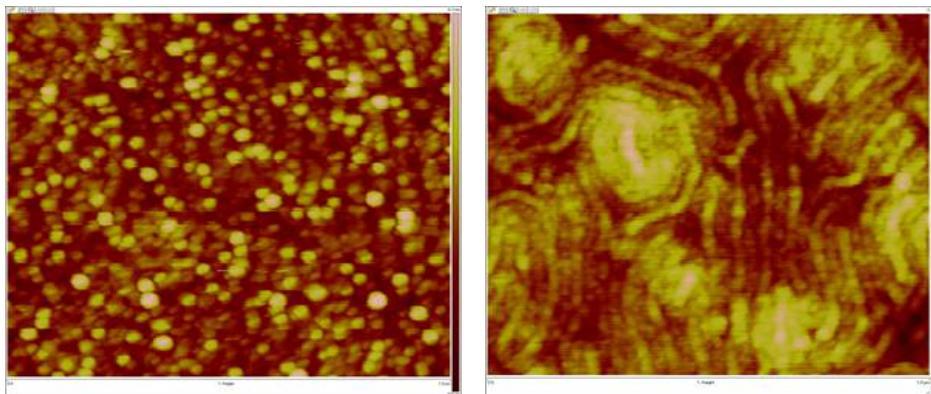


Figure 2.8: AFM phase image showing change in morphology of PHOST-b-PMMA from spherical to cylindrical after exposure to HFE rinse.

The origin of this change has to do with the polarity of the HFE solvent which was used to remove OSCoR. One way to rationalize this is if block A was more miscible than block B in a solvent then the stability of the film will be shifted more in the direction of A and the effective volume of A would be increased causing a resulting shift in the position in the phase diagram. HFE with different amount of IPA dissolved was used to test this hypothesis as shown in figure 2.9.

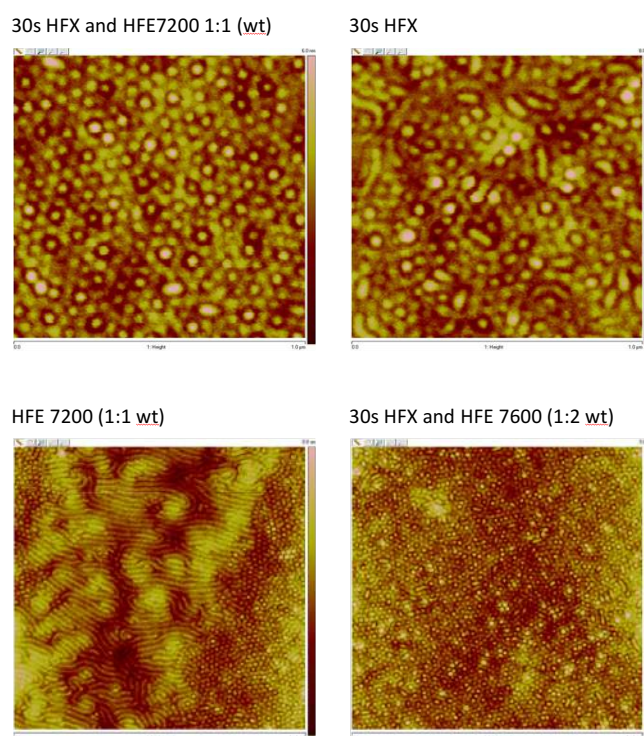


Figure 2.9: AFM phase images of PHOST-b-PMMA showing morphology change as a function of hydrofluoroether polarity. The solvent polarity increases in order from HFE7200 to HFE7600 to HFX.

We see that as the solvent gets more polar the morphology of the block copolymer film changes from cylindrical to spherical. In order to overcome this we reduced the amount of cross-linking of the photoresist by reducing the exposure dose so that it could be removed by a less polar solvent while simultaneously increasing the polarity of the developer essentially shifting the contrast curve. Another issue observed was that the

photoresist was not soluble in HFE after processing, however this issue was resolved by performing a HMDS vapor prime and the final results are shown in the figure 2.10.

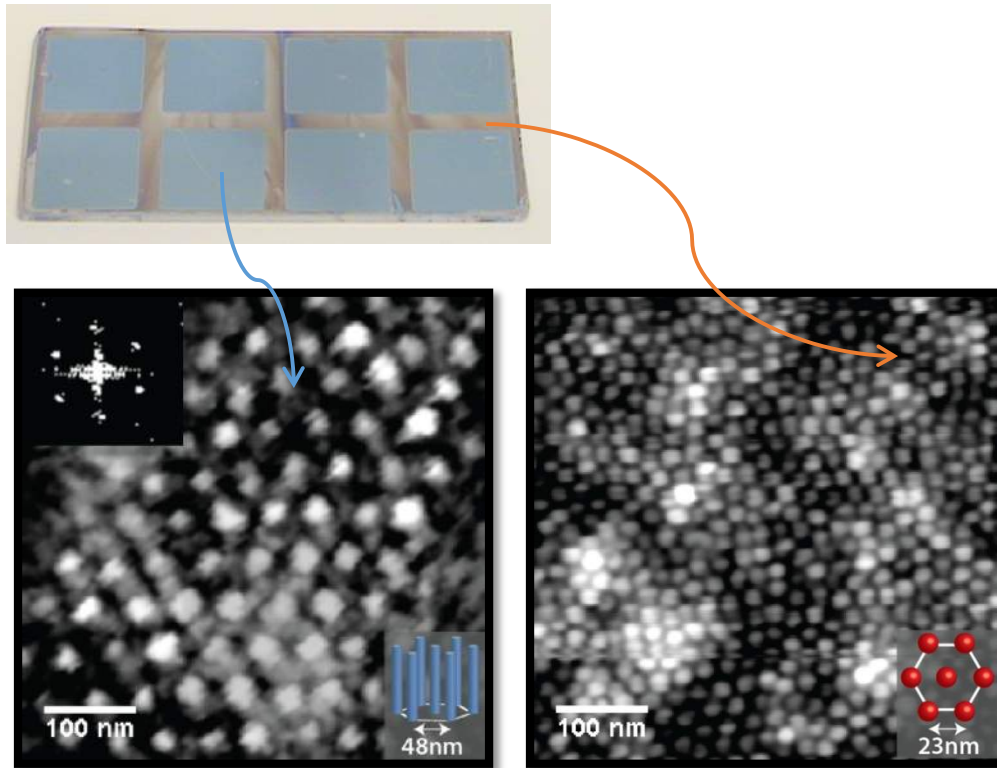


Figure 2.10: The upper figure is the cleaved wafer showing two regions due to the different dielectric constant of the two block copolymer films. The bottom left and right figures are AFM phase images of the corresponding regions with cylindrical morphology for the blue region and spherical morphology for the grey region.

CHAPTER 3

GRAPHENE PROPERTIES

3.1 Electrical Properties

We first discuss the electrical properties of graphene which is approximated using the tight binding technique. The assumption in tight binding is that the electrons are tightly bounded to the nucleus. Further it does not take into account electron electron interactions. Its advantage is that in semiconductors it is useful for constructing analytical models by extracting the overlap integrals from a much more expensive density functional theory calculation. Here we summarize the tight binding approach applied to graphene.[14]

Graphene is a 2d sheet of carbon atoms arranged in a honeycomb lattice. The crystal structure of graphene is a honeycomb bravais lattice with a 2 atom basis. The valence electrons of carbon are $2s^2 2p_x^1 2p_y^1$. In order to form a bond with its 3 nearest neighbours the s-orbital electron is first promoted to the p_z orbital so we now have $2s^1 2p_x^1 2p_y^1 2p_z^1$. Next hybridization of the 2s and 2 p electrons result in 3 sp^2 hybrid orbitals. Due to electrostatic repulsion between each other and out of plane repulsion by the remaining $2p_z$ orbital, these orbitals are separated 120 degrees apart in plane. The sp^2 hybridized orbitals form sigma bonds to 3 neighbouring carbon atoms. An observation here is that since the sigma bonds are held in plane between two carbon atoms they are localized. The remaining p_z orbital is overlapped with the p_z orbitals of 3 other carbon atoms so it is delocalized. Hence these p_z orbitals are responsible for the electrical conductivity of graphene.

Quantitatively we can minimize the coefficients of the final wavefunction wrt to energy to solve for the dispersion relation in graphene. We start with the real space basis vectors for the bravais lattice wrt to origin as:

$$(3.1) \quad a_1 = a \left[\frac{\sqrt{3}}{2} \vec{x} + \frac{1}{2} \vec{y} \right]$$

$$(3.2) \quad a_2 = a \left[\frac{\sqrt{3}}{2} \vec{x} - \frac{1}{2} \vec{y} \right]$$

where a is 2.46 Angstrom. Next we describe the hybridized orbitals:

$$(3.3) \quad \varphi_1(\vec{r}) \geq \frac{1}{\sqrt{3}} |\phi_{2s}(\vec{r}) \rangle + \frac{1}{\sqrt{6}} |\phi_{2px}(\vec{r}) \rangle + \frac{1}{\sqrt{2}} |\phi_{2py}(\vec{r}) \rangle$$

$$(3.4) \quad \varphi_2(\vec{r}) \geq \frac{1}{\sqrt{3}} |\phi_{2s}(\vec{r}) \rangle + \frac{1}{\sqrt{6}} |\phi_{2px}(\vec{r}) \rangle - \frac{1}{\sqrt{2}} |\phi_{2py}(\vec{r}) \rangle$$

$$(3.5) \quad \varphi_3(\vec{r}) \geq \frac{1}{\sqrt{3}} |\phi_{2s}(\vec{r}) \rangle - \sqrt{2/3} |\phi_{2px}(\vec{r}) \rangle$$

The coefficients are obtained by the s-orbital being equally distributed, p_x and p_y both contribute by the proportion of their angular projections in plane which is $\cos(30)$ for the p_y orbital and $\sin(30)$ for the p_x orbital and then normalizing the sum to 1.

Now define the basis vectors for the graphene atoms wrt to the bravais lattice as

$$(3.6) \quad d_1 = -\frac{a}{2\sqrt{3}} \vec{x}$$

$$(3.7) \quad d_2 = \frac{a}{2\sqrt{3}} \vec{x}$$

and the nearest neighbours as

$$(3.8) \quad n_1 = \frac{a}{\sqrt{3}} \vec{x}$$

$$(3.9) \quad n_2 = \frac{a}{\sqrt{3}} \left(-\frac{1}{2} \vec{x} + \frac{\sqrt{3}}{2} \vec{y} \right)$$

$$(3.10) \quad n_3 = \frac{a}{\sqrt{3}} \left(-\frac{1}{2} \vec{x} - \frac{\sqrt{3}}{2} \vec{y} \right)$$

Applying Bloch's theorem we write the trial wavefunction to the Schrodinger equation as

$$(3.11) \quad \psi_k(r) = \sum_m \frac{e^{ikR_m}}{\sqrt{N}} \left[C_{pzA}(k) e^{ikd_1} \phi_{pzA}(r - R_m - d_1) + C_{pzB}(k) e^{ikd_2} \phi_{pzB}(r - R_m - d_2) \right]$$

Substituting this into the schrodinger equation and making nearest neighbor approximation, we obtain

$$(3.12) \quad E_p C_{pzA}(\vec{k}) - C_{pzB}(\vec{k}) V_{pp\pi} (e^{ikn_1} + e^{ikn_2} + e^{ikn_3}) = E(\vec{k}) C_{pzA}(\vec{k})$$

$$(3.13) \quad E_p C_{pzB}(\vec{k}) - C_{pzA}(\vec{k}) V_{pp\pi} (e^{ikn_1} + e^{ikn_2} + e^{ikn_3}) = E(\vec{k}) C_{pzB}(\vec{k})$$

Finally we can solve for E(k) to get

$$(3.14) \quad E(k) = E_p \pm V_{pp\pi} (e^{ikn_1} + e^{ikn_2} + e^{ikn_3})$$

Now if we modify the previous two equations to include the overlap integral matrices then we obtain

$$(3.15) \quad E_p C_{pzA}(\vec{k}) - C_{pzB}(\vec{k}) V_{pp\pi} (e^{ikn_1} + e^{ikn_2} + e^{ikn_3}) = E(\vec{k}) C_{pzA}(\vec{k}) [1 - s(e^{ikn_1} + e^{ikn_2} + e^{ikn_3})]$$

$$(3.16) \quad E_p C_{pzB}(\vec{k}) - C_{pzA}(\vec{k}) V_{pp\pi} (e^{ikn_1} + e^{ikn_2} + e^{ikn_3}) = E(\vec{k}) C_{pzB}(\vec{k}) [1 - s(e^{ikn_1} + e^{ikn_2} + e^{ikn_3})]$$

We plot the resulting E(k) diagram in figure 3.1.

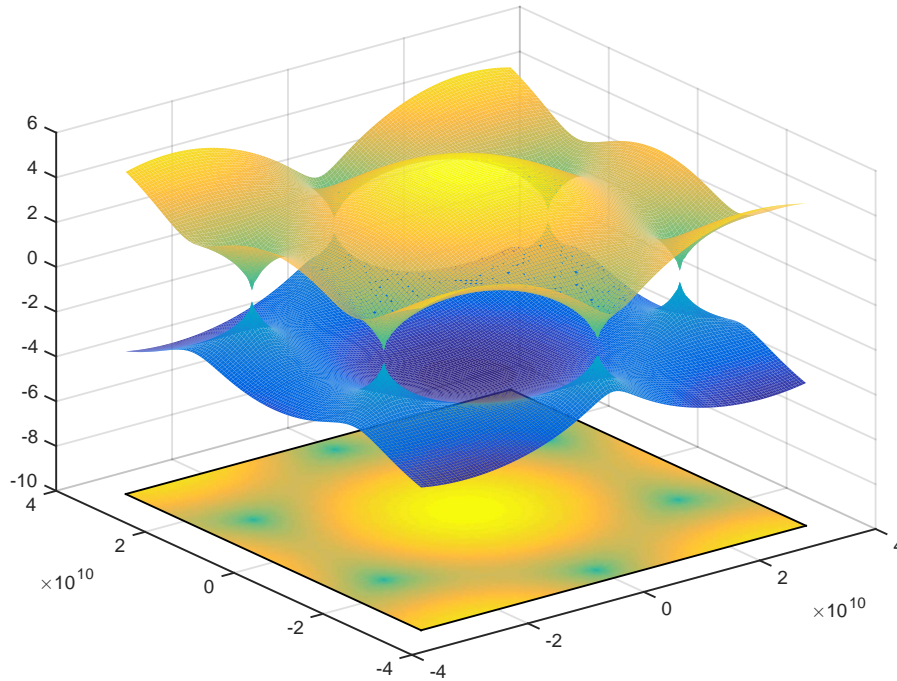


Figure 3.1: Electron dispersion in graphene assuming nearest neighbor tight binding

3.2 Mechanical Properties

Now we describe the phonon dispersion of graphene[15]. We apply Hooke's law and take the 5 nearest neighbours, these neighbours can be found by plotting a circle with different radii around the A and B carbon atoms. Further we assume small displacements around the equilibrium positions because we Taylor expand around the potential energy minima up to second order terms. We expect six phonon branches since there are two atoms per unit cell in graphene and each atom has three degrees of freedom: three acoustic branches and three optical branches. In the acoustic branches the A and B atoms move in phase while in the optical branches the A and B atoms move

out of phase. The high thermal conductivity of graphene comes from the out of plane acoustic branch and is reduced on substrates due to scattering.

3.3 Wetting properties

Finally we discuss the wetting and surface energy of graphene[16]. This topic is often neglected but plays an important role in the electrical properties in terms of contact resistance and dielectric gating. Fowkes first investigated this issue using Ceylon graphite from Sri Lanka. Metal graphene interface is usually modeled using DFT approaches because the classical electrostatic band alignment approach does not take into account the bonding which may range from weak van der waals to strong bonds. Furthermore in graphene it has been observed that most of the charge injection happens at the edges and not in the bulk of the contact[17]. Secondly wetting of graphene by other materials such as dielectrics and water are important. There have been studies indicating that graphene is hydrophobic due to exposure in air and that graphene is hydrophilic because there is a pi-hydrogen bond, surface defects in graphene and partial wetting transparency. Since copper and oxide are both hydrophilic, graphene on these materials should be hydrophilic as well.

In general graphene is not suitable for conventional electronics because despite its high mobility it has very low carrier density hence the RC time constant of electronics based on graphene will be higher than silicon.

3.4 Processing of Graphene

Graphene can be produced by exfoliation, CVD growth or epitaxial growth. In graphene exfoliation a piece of graphite typically HOPG Graphite or Kish graphite. We have found that it is much easier to exfoliate Kish graphite than HOPG graphite this could be because HOPG is mostly bernal stacked and Kish is not. Furthermore since Kish is a byproduct of steelmaking it contains more impurities and is not suitable for spin devices. For our purposes we have mainly used Kish graphite and a scotch tape. The technique is described next.

3.4.1 Graphene Exfoliation

First a small flake of Kish graphite is put on one end of a scotch tape secured face up on a table. Another piece of tape is then brought on contact with the graphite and shifted perpendicular to the tape so that a row of flakes is obtained on one edge of the tape. In the next step the tape is shifted parallel to the tape and the row is repeatedly exfoliated and stamped until the whole strip is populated. We repeat this around 20 times using a new piece of tape each time to thin down the graphene flakes.

The final piece of tape is then applied to a wafer coated with 90nm or 300nm of SiO₂. However depending on the project other dielectrics may be used and the thickness of the dielectric needs to be calculated to maximize the contrast. The calculation is based on interference between the graphene film and the oxide film. A plot of the contrast vs wavelength is shown below.

After applying the tape to the wafer, the back of a pen is used to gently rub the surface of the tape for a minute to loosen the single layer onto the substrate and let it adhere to

the substrate. Finally the tape is lifted up from the substrate at a very small angle to ensure that it does not break the flake and maximize the size of the transferred flake. Next using an optical microscope the positions of the flakes are recorded and raman spectroscopy is used to determine the number of layers of graphene.

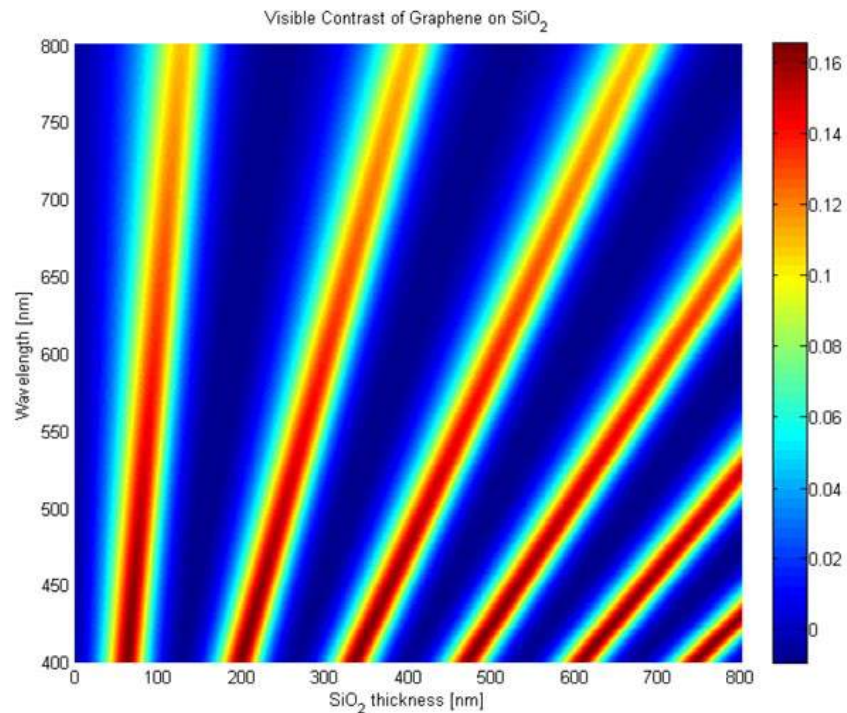


Figure 3.2: Visible contrast of graphene on SiO₂ computed assuming graphene has permittivity of 3.1 and thickness of 0.84nm. Graphene gives a higher contrast at certain thicknesses due to interference in the reflected light.[18]

3.4.2 CVD Graphene

CVD graphene is obtained by surface absorption of methane on copper or nickel and nucleating a growth site. In our work we use copper because the solubility of carbon in copper is lower than in nickel allowing us to obtain single layer graphene[19]. Chemical vapor deposition is dependent on the cleanliness of the copper and the growth tube as well as the methane and hydrogen. In the past copper foils have been purchased from

Alfa Aesar and Nilaco. First the copper foils are cleaned in acetone followed by IPA followed by water and then acetic acid and rinsed in water followed by IPA and dried to remove the native oxide on copper. The acetic acid step should be at least 10 minutes to ensure that the native oxide is removed.

Next the copper foil is transferred into a quartz tube and then annealed in hydrogen at 1000C at 10^{-6} torr for an hour to further remove any contaminants. The temperature depends on the activation energy for the graphene growth and ranges from 700C to 1100C which is close to the melting point of copper. A low vacuum pressure is important to ensure reduced number of contaminants, here the choice of a dry pump is necessary further since copper condenses on the pump during growth, it has a finite lifetime. The insulator for the heater is carcinogenic hence it would be helpful to be efficient in the number of growths per period. Now methane and hydrogen are flowed into the chamber at a ratio 100:1 sccm for larger grain growth and 36:2 sccm for smaller grain growth. During growth methane is first adsorbed on the copper surface and then dehydrogenation of methane occurs followed by diffusion of the carbon along the copper surface and finally the carbon is added to the graphene. In order to further slow down the growth and number of nucleation sites, the copper foil may be wrapped in another copper foil. The grain size of the graphene depends heavily on the number of nucleation sites which itself depends heavily on defects and impurities on the copper surface. Also at each nucleation site the graphene tends to be more than single layer e.g. bilayer or trilayer, hence a complete single layer growth is not possible. There is little literature on this issue except to minimize the number of sites but one explanation could

be that graphene solubility and surface energy at the nucleation sites promote growth of bilayer or trilayer graphene due to the presence of impurity or defects.

During the course of this work there were several contamination issues. The Dresselhaus group at MIT has examined contaminants on copper using energy dispersive x-ray spectroscopy (EDX) and Auger spectroscopy (AES) and determined that the cause of contamination are metal particules such as Si, Ca, Pt, Ru. The size of the particles range from nm to um and their density is typically on the order of 10um^{-2} . In the case of copper contamination, electropolishing of copper was attempted however this necessitated finding the IV region where uniform polishing and not deposition occurs in an electrochemical cell. An alternative is to grow the copper epitaxially by sputtering copper onto a 111 sapphire wafer and then electroplating up to the required thickness which is 0.025mm. In this second case there is a careful interplay between being able to peel the copper off the sapphire wafer and making sure the copper adheres to the wafer during electroplating. For the case of chamber contamination, one route is to perform a growth on the tube itself. This coats the tube with carbon and reduces the evaporation of material from the tube onto the copper foil.

Next we discuss graphene transfer. Before transfer the graphene has to be uniformly grown, if it is partially grown all the transfer techniques described here will have a much lower yield, around one in ten at best. In the wet transfer process, a layer of pmma is spun onto the graphene copper stack. In the next step the copper on the back of the graphene is etched away in plasma. The thickness of the pmma spun is as thin as possible to ensure easier removal but thick enough to not break up from the surface tension in

water and also able to protect the graphene from any leakage in plasma. Exposing pmma to plasma makes it harder to remove so an alternative is to use a kitchen scrub and scratch the graphene off the back of the foil so that it can be etched in this way graphene is not exposed to plasma.

The graphene is then etched in iron chloride FeCl_3 or ammonium persulfate NH_3PO_4 etchant. The etching mechanism of copper due to iron chloride is via reaction but persulfate etches via oxidation. Iron residue is a big cause of uncontrollable doping and impurity scattering after the copper etch partly because it diffuses into the pmma. Ammonium persulfate oxidizes the pmma as well making it harder to remove. In order to overcome this coating graphene with a layer of Au can be done before spin coating pmma. The Au can be removed using Au etch which does not contaminate graphene as much. In case persulfate is unavailable, a dilute RCA clean can remove the iron contaminants from iron chloride etchant.

3.4.3 Graphene Dry Transfer

For our work, we pursued a dry transfer technique which is much cleaner but also much less reproducible and there is an interplay between the graphene grown (e.g. grain size and coverage) and how successful the transfer is. The transfer hinges on the surface energy of graphene and the substrate. A graphene/pmma/pdms/glass slide is created and the stamp is pushed onto an oxide surface. If the van der Waals force between the graphene and oxide is higher than the van der Waals force between the pmma and pdms then the pdms will detach leaving behind graphene on the oxide surface with no trapped contaminants in between. After the stack is stamped onto the surface, it is placed on a

hotplate and then a tweezer is used to peel off the pdms. The reproducibility issue arises because we have poor control of the oxide and graphene surface energies. Further the graphene is not flat, the pmma retains some memory of the copper grains and folds, which is why the oven is necessary for relaxing the pmma on the substrate. Iron chloride etchant is used to etch copper for this transfer since persulfate oxidizes the pmma. One can usually obtain continuous graphene pieces ten times larger than exfoliated graphene around $100\mu\text{m}^2$ using this technique and not continuous pieces around a centimeter in size. We summarize the dry transfer process in figure 3.3 and show some results in figure 3.4

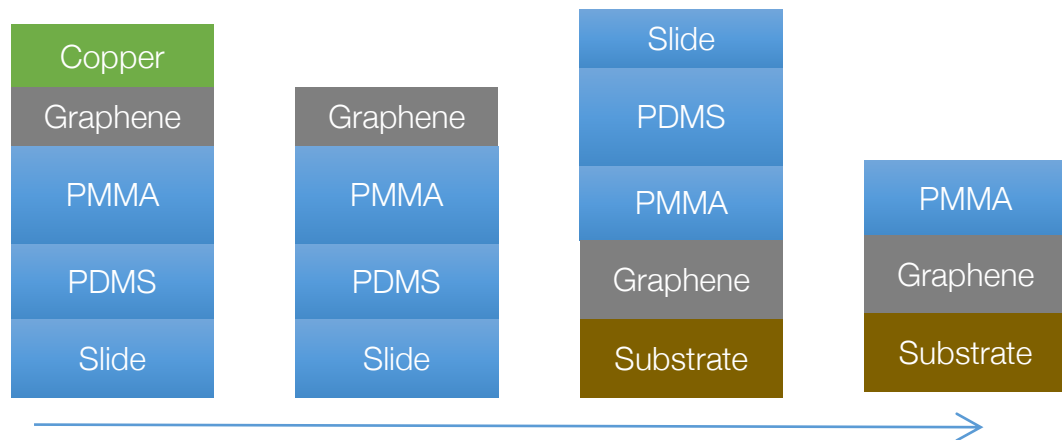


Figure 3.3: Summary of dry transfer process flow, from left to right; After spinning PMMA and attaching to PDMS/slide, after copper etching, applying the film stack on the substrate, after heating and removing the PDMS/slide

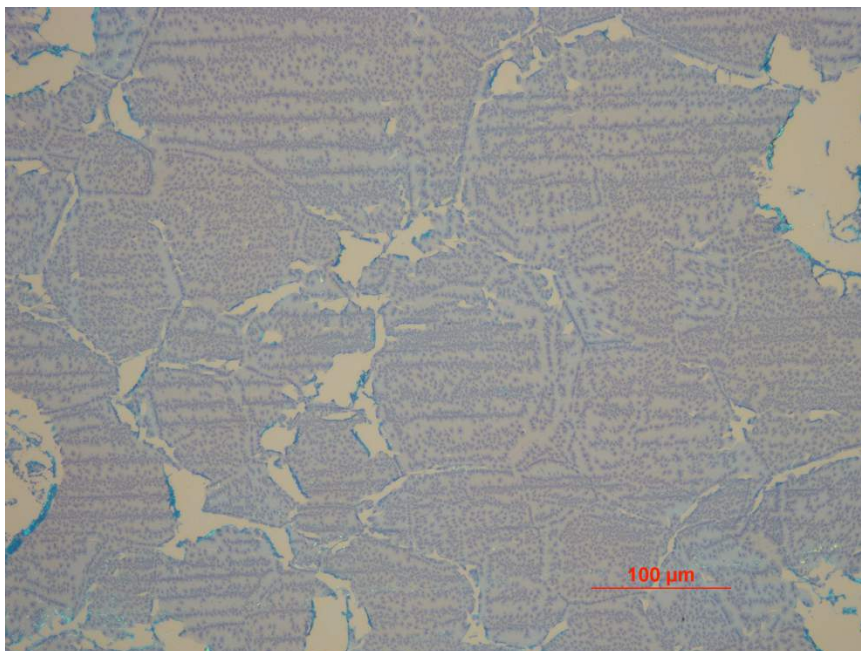


Figure 3.4: Graphene after dry transfer. The tears follow the grain boundaries of the copper which are raised, other tears come from the rippling in graphene film. The scale bar is calibrated using the focus plane of the microscope.

After the graphene is transferred to substrate, we perform raman spectroscopy on the graphene to determine the whether there are significant defects and also whether it is single layer. We excite the sample with a 488nm laser and then filter out the reflected laser line using a notch filter and the remaining reflected light is sent to a grating which resolves the reflection angle of the light based on wavelength and sends it to a thermoelectrically cooled CCD detector. The wavelength of the photons arriving at the CCD is a nonlinear function of pixel location. To compensate for this the grating is motorized and a slit is put in front of the CCD so our spectrum is obtained by scanning over the wavelengths. A typical raman spectrum of CVD graphene on SiO_2 substrate at room temperature we obtain is shown in figure 3.5:

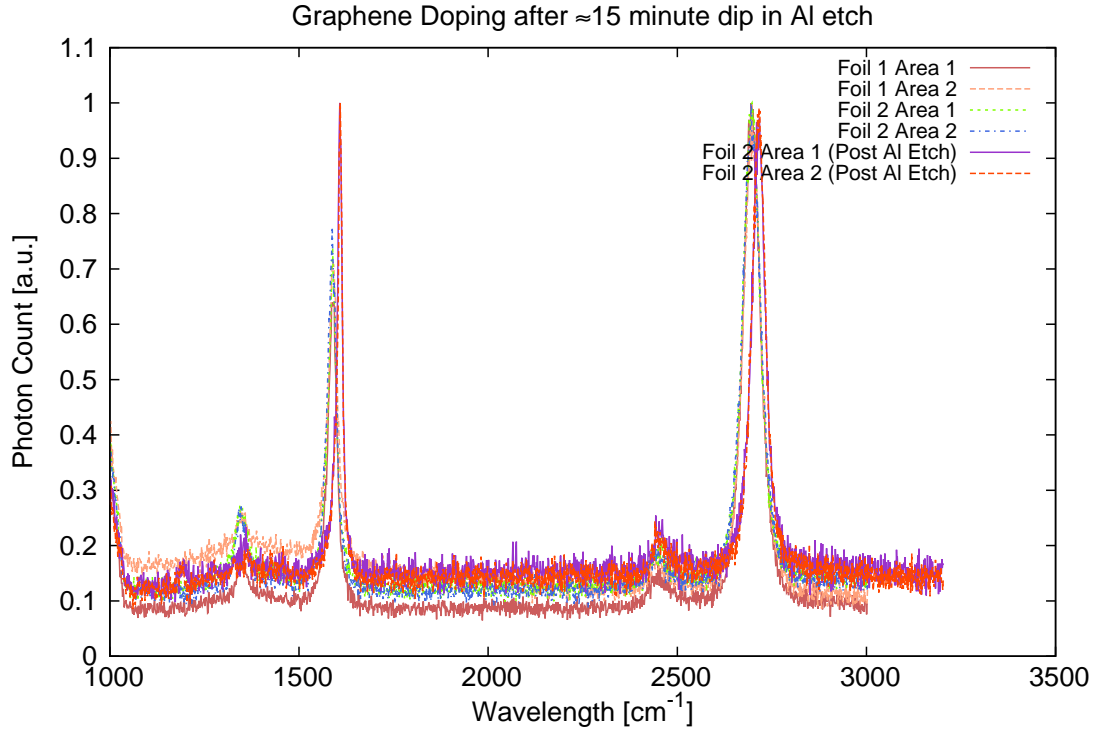


Figure 3.5: Raman scattering in the graphene film by shining 488nm laser on a transferred film through an objective. The small ratio between 2D peak at 2570cm^{-1} and G peak at 1580cm^{-1} indicates a high doping. The D peak at 1350cm^{-1} indicates that the sheet has defects likely due to the doping process since it intercalates the graphene.

We will mention the features that are relevant to determine the quality and doping of the graphene sheet[20]. The G-peak at 1580cm^{-1} corresponds to the high frequency E_{2g} phonon at the Gamma point, the D-peak at 1350cm^{-1} comes from TO phonons around the K point and requires a defect to activate. The 2D peak at 2690cm^{-1} arises from the D band overtone consisting of two phonons of opposite wave vector. The amount of defects in the graphene can be estimated by the intensity of the D peak while the amount of doping can be determined by the shift and intensity of the G-peak. During our work we discovered that the doping need not be from charged species to cause a shift in the G-peak, this is important for using raman spectrum to determine doping.

3.4 Graphene FETs

In contrast to raman spectroscopy electrical characterization is a direct but destructive measurement of the electrical properties of graphene. Temperature dependent field effect measurements were performed on CVD graphene using a polymer gate NFC 1400-3CP (JSR Micro, Inc.)[21]. We first perform a wet transfer as described previously, then spun the polymer on to the graphene. A lift-off is performed the form contacts to the graphene sheet and finally we apply a gate dielectric consisting of the NFC polymer and the hafnium oxide.

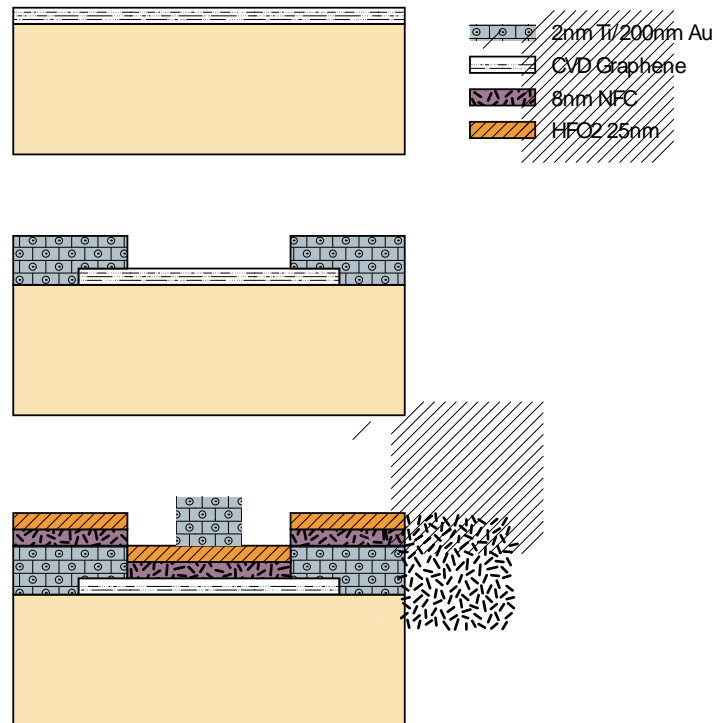


Figure 3.6: Summary of process to fabricate a top gate on graphene. First a layer of NFC polymer is spun on graphene which serves as a precursor attachment site for ALD Hafnium Oxide

We show a typical device characteristic in figure 3.7:

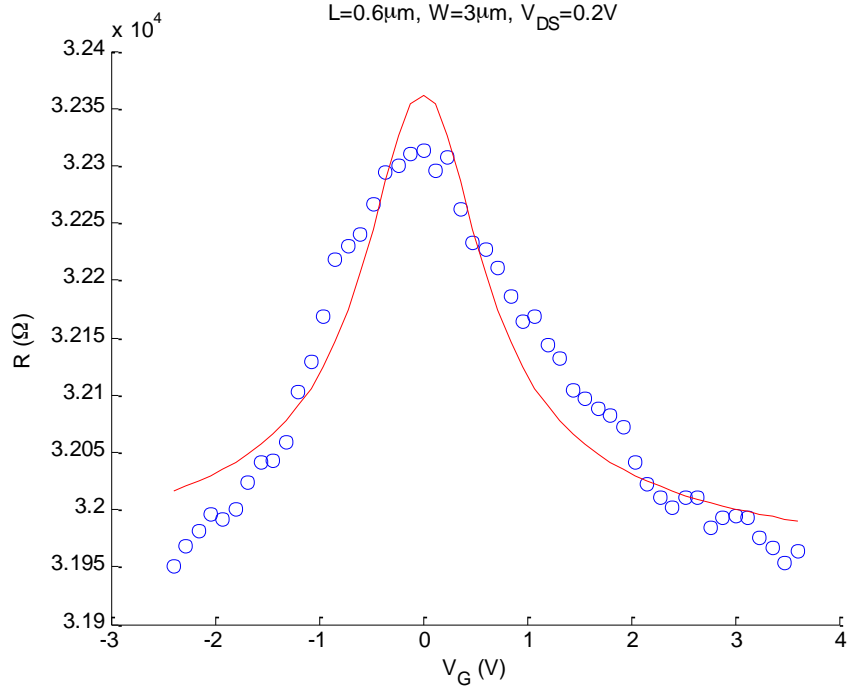


Figure 3.7: Drain current from sweeping the top gate of a graphene FET. The device is almost intrinsic since the minima is located near 0V

The device is fit to the equation 3.17[22]

$$(3.17) \quad R_T = R_S + \frac{L_G}{W e \mu_{FE} \sqrt{n_0^2 + n^2}}$$

where R_s is the contact resistance, n is the modulated carrier concentration and n_0 is the residual carrier concentration. For this device the extracted contact resistance was 31.8kΩ, the mobility was 3052 cm²/Vs and the doping was 9×10⁵ m⁻². We also plot the distribution of the other devices on the chip in figure 3.8 showing that most of the devices have a mobility around 1000 cm²/Vs and that graphene devices show a very large variation due to their large surface area compared to conventional devices where the bulk dominates.

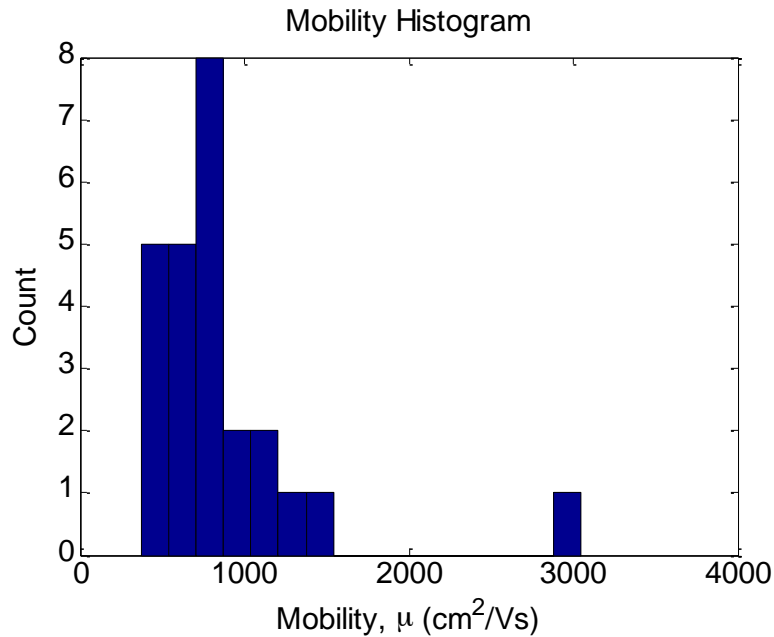


Figure 3.8: The mobility of all the devices on a single die from a 1inch by 1inch graphene sheet, devices which do not show any modulation are excluded. Most devices show mobility less than 1000cm⁻¹ with 1 device showing mobility greater than 3000cm⁻¹. These statistics are representative of our samples.

During electrical measurements of graphene devices there is always the presence of hysteresis even below 100K indicating that the hysteresis is not due to the presence of water. The hysteresis originates from the schottky contacts and also trapped charge in the region underneath the gate from adsorbed contaminants. Note that the hysteresis can be made to “disappear” by increasing the wait time during the measurement to a few RC constants of the largest capacitance in the circuit. Also the IV characteristic will appear steeper and result in a higher extracted mobility. Hence unusually high values of mobility reported in literature should be taken with a grain of salt. Another issue is the extracted mobility is heavily dependent on the thickness of the gate oxide and for graphene this is usually evaporated oxide since it is difficult to nucleate any sort of

dielectric on graphene as all the available bonds are saturated. Values of gate dielectric thickness read off the evaporator for example will give a different thickness than an ellipsometric measurement with fit of the dielectric constant using a Cauchy or Selmeier model. Our reported values here use a wait time of nanoseconds and an averaging time of microseconds. Some values reported in literature have used the steepest slope to extract mobility which is not accurate since the slope is nonlinear.

In our measurements we used a top gate, however using a back gate is also possible. In the event of using a back gate, careful oxide growth needs to be undertaken. During our oxide growth, we observed that there was a micro masking effect and after stripping the oxide and performing AFM measurements we see pits. The origin of the micro-masking is not clear as it is independent of the furnace tube used and the wafer source. A precaution with respect to the wafer box is to remove the wafers and store them in the blue Teflon containers as soon as the box is opened because outgassing from the boxes could be a potential source. Also annealing the furnace tubes before growth is another precaution. Growing oxide at a lower temperature if possible would also help as it is possible that the high temperatures together with the HCL gasses corrode the pipes causing material to be deposited on the wafers. Finally the choice of wafer doping helps to ensure the dopants do not diffuse into the oxide causing a reduction in breakdown voltage and the thickness helps to prevent probe from breaking the oxide during measurement and shorting out the substrate.

3.5 FTIR spectroscopy of graphene

Fourier transform infra red spectroscopy is used to study IR active compounds meaning compounds that can have an excited dipole and/or phonon modes that are IR active. Whether a phonon mode is ir-active or not is determined by the space group of its crystal, our current understanding is that graphene phonons are not ir-active. In order to study plasmons, ftir is useful to have because it allows access to IR wavelengths and the free space radiation couples into confined plasmons which are IR active.

An FTIR consists of a light source, a Michelson interferometer and a detector. The light source is usually a globar that is cooled during idle time to increase its lifetime. A Michelson interferometer takes light from a source and splits it into two arms, one static and one movable then by recombining them with an optical path difference. An interferogram is the intensity at the detector plotted against this path difference and the spectrum is the fourier transform of the interferogram. The resolution of the scan is determined by the maximum travel of the mirror in the movable arm. The range of the spectrum is determined by the step size of the travel. Since graphene has a 2% absorption it is necessary to average over several scans and also the drude peak is close to the the water absorption peaks for 1um sized features, it is important to purge the chamber thoroughly. In the event drift is negligible we would perform few averages of long scans. The sources of error in the FTIR come from drift due to the light source and also from the travel motor especially for long measurements so we perform many averages of short scans. In order to setup a measurement we need to select an optical velocity and gain. The optical velocity is twice the mirror velocity or the speed of travel and the gain sets the amplification of the detector signal. Lastly, it is difficult to

determine a priori the position of the drude peak, hence we need to scan over a broad range of wavelengths. We use a nitrogen cooled MCT photodetector with a KBr beamsplitter for mid-ir measurements from $370\text{-}7800\text{cm}^{-1}$ and a silicon bolometer for far-ir measurements. Below we show a scan of a dry transfer sample as a function of temperature.

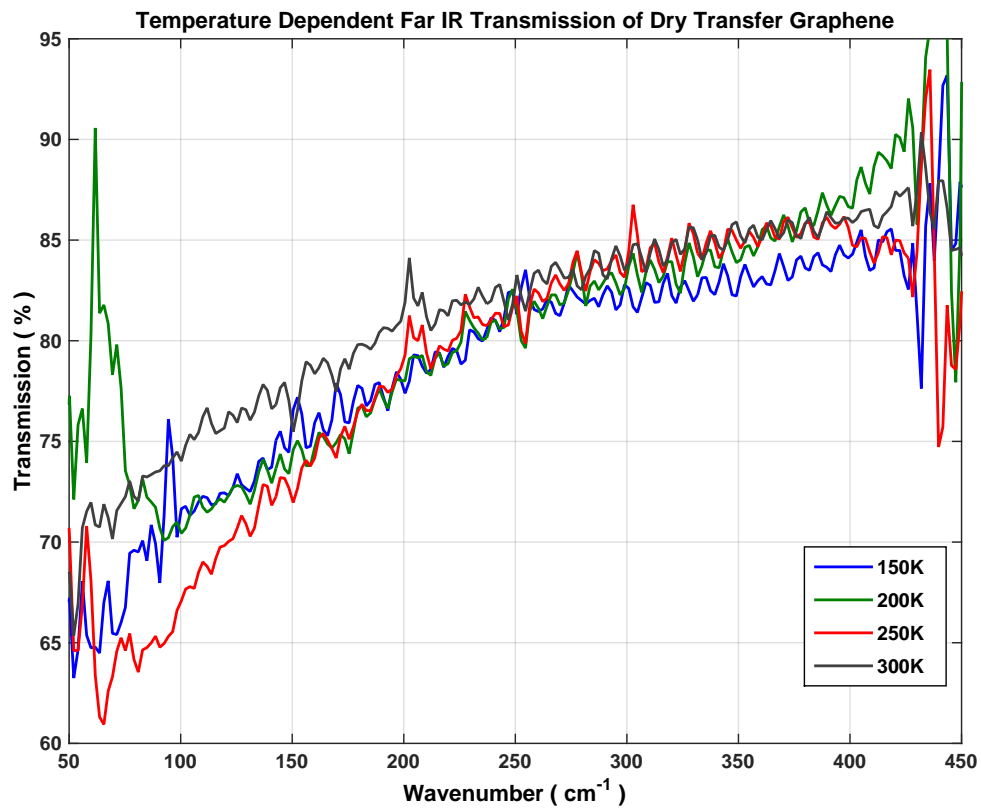


Figure 3.9: Absorption spectra of graphene in the far IR showing drude peak at 3 different temperatures. Due to the dry transfer there is no water trapped under the graphene which provides a route to temperature dependent measurements

CHAPTER 4

GRAPHENE PLASMONS IN THE FAR-IR

4.1 Introduction

Plasmons are collective charge oscillations, which have applications in enhancing existing technologies by confining light to very small volumes. Examples of potential applications of plasmons being investigated are in increasing the efficiency of thin film photovoltaics by light trapping, reducing the write and read current of non-volatile memories by heating and for biological and chemical sensing by surface functionalization. In the past plasmons have been investigated in metals because the carrier density is high, however the damping time is small. Here we investigate plasmons in graphene because of its high mobility and the ability to tune the plasmon resonances by tuning the Fermi level.

We first describe the optical absorption in graphene. In intrinsic graphene the optical absorption is due to interband transitions and from a golden rule view, since the frequency and the Fermi velocity cancel out in the product of the transition matrix element, the density of states and the photon energy, the absorption is independent of frequency. Hence designing a graphene spectral imager based on photoelectric response is challenging despite its ability to access difficult parts of the spectrum. In hole doped graphene, interband transitions below twice the fermi level are forbidden and this leads to a decrease in higher energy interband absorption and an increase in lower energy intraband absorption.

Quantitatively, we can describe the plasmon dispersion using the Lindhard formula and integrate it over the first Brillouin zone numerically. A plot of the plasmon dispersion is given below

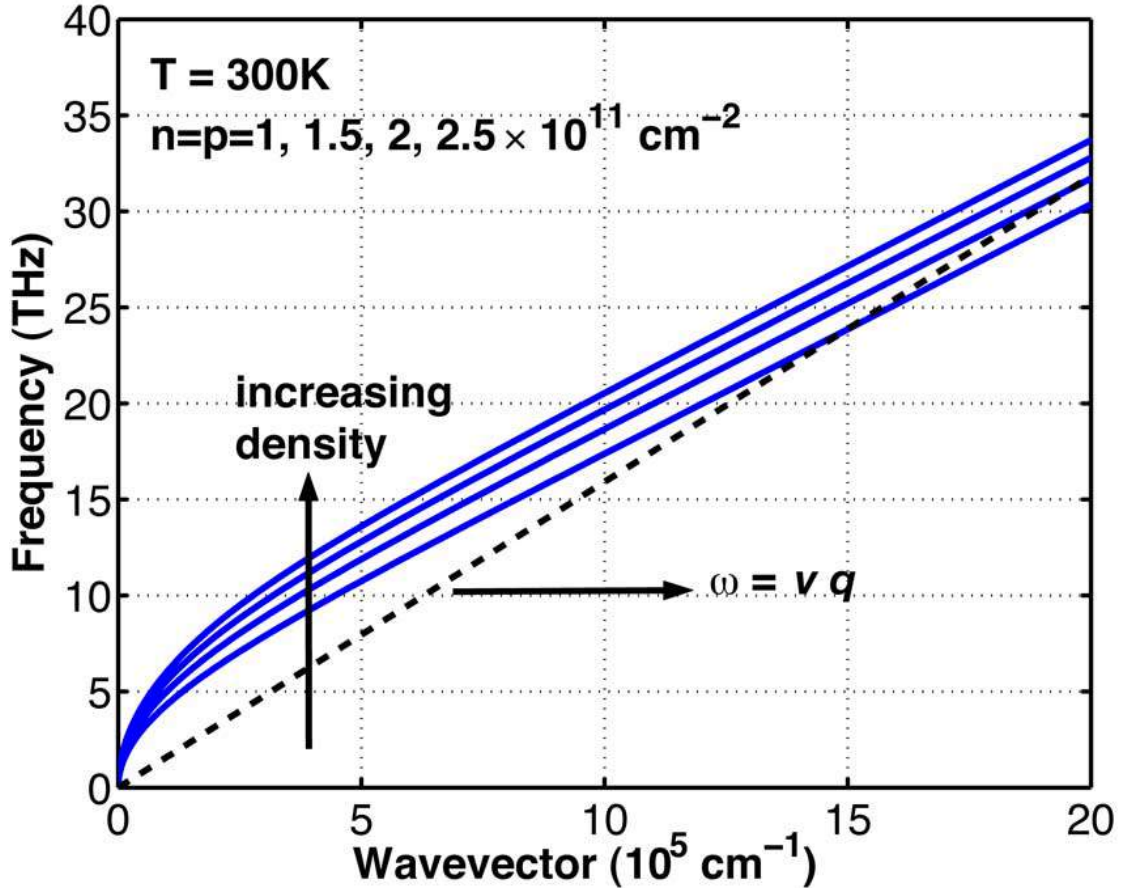


Figure 4.1: Plasmon dispersion relation in graphene for different carrier densities at 300K [23]

If we design a plasmon resonator with frequency corresponding to wave number k , and this model is correct, we would expect to measure a point on this plasmon dispersion curve with frequency ω .

4.2 Device Fabrication

To investigate this, we first designed a gated structure of varying strip sizes so that we could adjust the Fermi level while performing the measurement. We explored several

options to gate the device, however gating the device proved challenging because a doped substrate was not transparent in the IR region, neither was a top gate with metal thicker than a few nm considering our absorption of 2%. Secondly, we needed the strips to have a high aspect ratio because the beam spot was millimeters and the strips were microns in length. The key here was leveling a quarter wafer in the stepper to obtain the focus we needed. We experimented with top gating, however the evaporated oxide even when covered in atomic layer deposited oxide was always leaky since just a few pinholes over a mm sized region was enough to short the device contacts to the gate. An alternative is to use an ion-gel[24]. Ion-gel gates work by inducing a dipole directly on to the graphene sheet with a contact that can be placed away from the sample. By ensuring that the IR active features of the ion-gel are far away from the drude peak, ion-gel gating can be used to tune the Fermi level.

An alternative solution is to dope the graphene chemically[25]. Here after the graphene is patterned and etched we dip the sample into nitric acid. The limitations are a reduced mobility. We also found that since graphene is hydrophobic either due to pmma residue and/or since its surface is non-polar it was difficult to wet the graphene with the nitric acid. Hence several samples had to be produced to ensure the graphene was doped. If graphene is not immersed long enough the graphene is undoped but if it is left too long, the nitric acid intercalates the graphene and causes tears and cracks on the strips. The concentration of the nitric acid determines the amount of doping for the graphene. By varying the nitric acid concentration and immersion period, we found that a time of 30 seconds and nitric acid concentration of 30% works best. We fabricated arrays of

graphene strips with widths of 0.75, 1, 2 and 3 μm on a high resistivity wafer ($>10\text{k}\Omega\text{ cm}$) with 300nm of thermally grown oxide as shown in the figure 4.1. The pitch of the strips was chosen as twice the width. The doping of the strips was estimated to be $4.5\text{-}5.0 \times 10^{12}\text{ cm}^{-2}$ by raman measurement of the G peak. A microscope image of the device is shown in the figure 4.2.

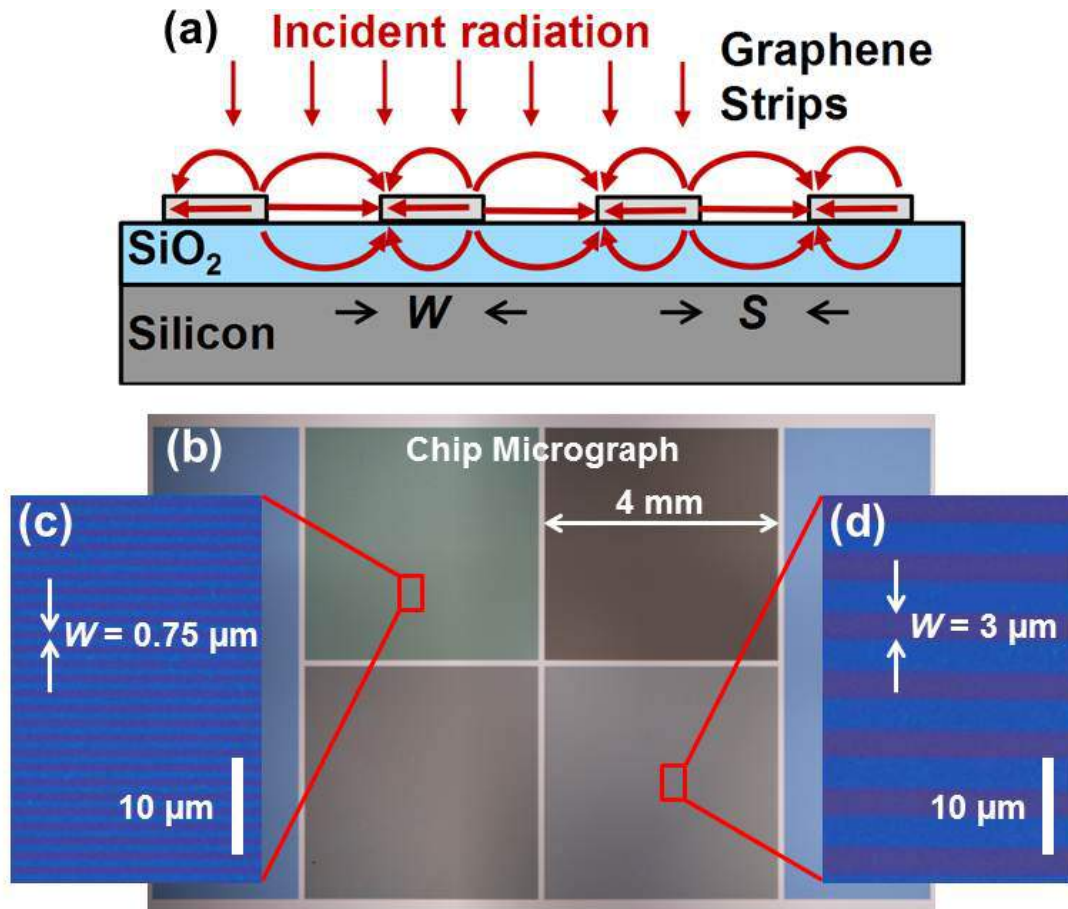


Figure 4.2: (a) cross section of the device. (b) microscope image of top view of device consisting of high aspect ratio 0.75, 1, 2, 3 μm strips. The purple areas in the inset are SiO₂ and the blue areas are graphene due to photoresist residue on them.

Plasmon resonances of arrays of graphene strips were measured at room temperature using Fourier-transform infrared spectroscopy (FTIR). We plot the transmission spectrum in the figure 4.3. For incident radiation of parallel orientation we see the drude-like frequency dependence,

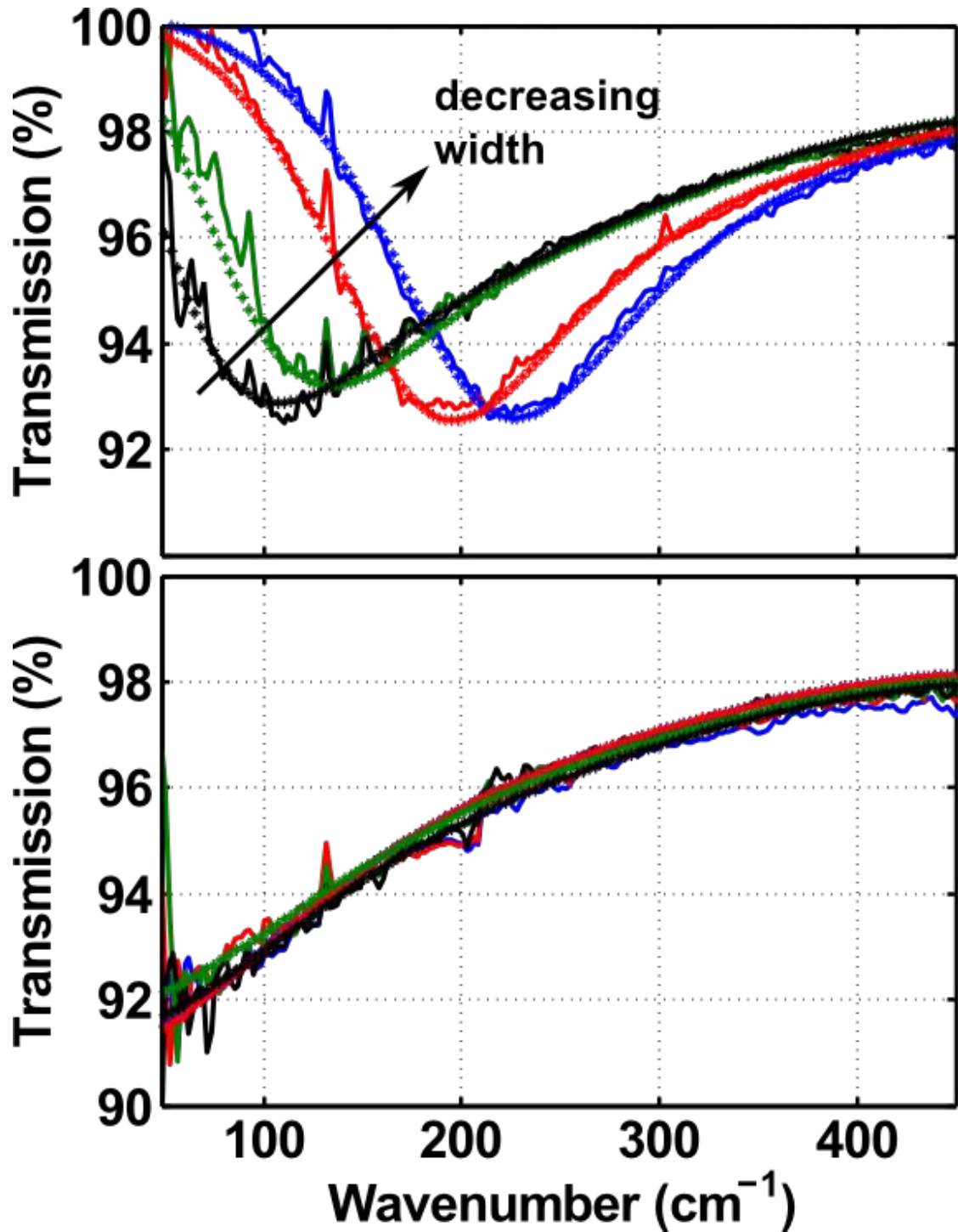


Figure 4.3: (Solid) Measured transmission of radiation polarized (a) perpendicular and (b) parallel to graphene strips is plotted for four different strip widths $W=0.75, 1, 2,$ and $3\mu\text{m}$. For all devices, the spacing S between strips is equal to the width. A bare SiO_2/Si substrate is used as reference. (Dots) FDTD simulation fits to the measured results. Extracted resonance frequencies are $226, 197, 135,$ and 112 cm^{-1}

The transmission of incident radiation polarized parallel to the strips decreases monotonically at long wavelengths, showing the expected Drude-like frequency dependence. At DC the electrons move in phase with the electric field and as the frequency is increased they slowly move out of phase until they become transparent to the electric field. There is no dependence on the strip width. Transmission spectra of incident radiation polarized perpendicular to the strips show plasmon resonances. When the frequency of incident radiation matches the cavity mode we see a maxima in absorption. The asymmetry in the peak is due to the fact that at low frequencies the cavity dimensions limit the plasmon oscillations and at high frequencies the oscillations are limited by the carrier mobility. This can be seen from the trend of the asymmetry getting less as the cavity size decreases.

4.3 Drude Model of Graphene Plasmons

The measured spectra can be described using a damped harmonic oscillator model[26],

$$(4.1) \quad \frac{T_{\epsilon}(\omega)}{T_{ref}(\omega)} = \left| 1 + \frac{\eta_0 f \sigma(\omega=0)}{1+n_{sub}} \frac{i\omega/\tau}{\omega^2 - \epsilon\omega_p^2 + i\omega/\tau} \right|^{-2}$$

Where η_0 is the free space impedance σ_0 is the dc conductivity of bulk graphene, f is the fill factor of the strips, n_{sub} is the refractive index of the substrate, τ is the Drude scattering time, ω_p is the plasmon frequency and $\epsilon = 0$ for incident radiation polarized parallel or 1 for incident radiation polarized perpendicular to the strips. According to the graphene plasmon dispersion described previously, the bulk plasmon frequency for small wave vectors is given by the expression[27]

$$(4.2) \quad \omega_p(q) = \sqrt{\frac{\sigma(\omega=0)q}{2\epsilon_{avg}\tau}}$$

where q is the magnitude of the plasmon wave vector and ϵ_{avg} is the average dielectric constant surrounding the graphene sheet. Using $q = \pi/W$, we find that the equation for bulk plasmon frequency significantly overestimates the plasmon frequencies compared to the experimental values. For example using the previous equation to fit the transmission spectra of $W = 1\mu\text{m}$ arrays for parallel polarizations ($\epsilon=0$), we find that the average value of $\sigma(\omega=0)$ and τ to be 0.95 mS and 31.5 fs respectively. Equation 4.2 then gives a plasmon frequency of $\approx 245\text{ cm}^{-1}$ which is significantly higher than the plasmon frequency of $\approx 197\text{ cm}^{-1}$. Such a large error suggests that better models are needed to understand confined plasmon modes in patterned graphene structures.

We first present an analytic technique that captures the essential physics of the problem and results in an eigenvalue equation for the plasmon modes. Assuming a Drude-like frequency dependence of the graphene conductivity[28], we start with the time derivative of the equation for the current density \vec{K} ,

$$(4.3) \quad \frac{\partial^2 \vec{K}}{\partial t^2} + \frac{1}{\tau} \frac{\partial \vec{K}}{\partial t} = \frac{\sigma(\omega=0)}{\tau} \frac{\partial}{\partial t} (\vec{E}_{\text{inc}} + \vec{E}_d)$$

Here \vec{E}_{inc} is the incident electric field and \vec{E}_d is the depolarization field that results from the plasmon charge density. Only field components in the plane of the graphene sheet are included in the equation. Physically the incident electric field induces a depolarization field in the graphene and we want to relate the depolarization field to the sheet current density. The derivation here expands on the derivation in the paper. Starting with the expression for electrostatic potential due to the charges in graphene,

$$(4.4) \quad \phi(\vec{r}, t) = \int d^3 \vec{r}' \frac{\rho(\vec{r}', t)}{4\pi\epsilon|\vec{r}-\vec{r}'|}$$

where ρ is the charge density and ϵ is the average dielectric permittivity of the dielectric surrounding the graphene sheet. We define the depolarization field as $\vec{E}_d(\vec{r}, t) = -\vec{\nabla}\phi(\vec{r}, t)$. So taking the gradient with respect to r of equation and substituting it into E_d we have

$$(4.5) \quad E_d(\vec{r}, t) = \int \frac{d^3\vec{r}'}{4\pi\epsilon} \frac{\vec{s}}{|\vec{s}|^3} \rho(\vec{r}', t)$$

Here the separation vector $\vec{s} = \vec{r} - \vec{r}'$. By charge continuity equation,

$$(4.6) \quad \vec{\nabla}_{\vec{r}'} \cdot \vec{K}(\vec{r}', t) = -\frac{\partial \rho(\vec{r}', t)}{\partial t}$$

The charge in the graphene sheet can be related to the sheet current, we take the derivative of equation wrt time and substitute it into equation to obtain

$$(4.7) \quad \frac{\partial E_d(\vec{r}, t)}{\partial t} = -\int \frac{d^2\vec{r}'}{4\pi\epsilon} \frac{\vec{s}}{|\vec{s}|^3} \vec{\nabla}_{\vec{r}'} \cdot \vec{K}(\vec{r}', t)$$

Integrating by parts we get

$$(4.8) \quad \frac{\partial E_d(\vec{r}, t)}{\partial t} = \int \frac{d^2\vec{r}'}{4\pi\epsilon} (\vec{K}(\vec{r}', t) \cdot \vec{\nabla}_{\vec{r}'}) \frac{\vec{s}}{|\vec{s}|^3}$$

The additional term goes to zero because at $|\vec{s}| = \infty$ it goes to 0. We can then simplify the expression above into

$$(4.9) \quad \frac{\partial E_d(\vec{r}, t)}{\partial t} = -\int \frac{d^2\vec{r}'}{4\pi\epsilon} \frac{1}{|\vec{s}|^3} \left[\mathbb{I} - \frac{3\vec{s}\otimes\vec{s}}{|\vec{s}|^2} \right] \cdot \vec{K}(\vec{r}', t)$$

where \mathbb{I} is the identity matrix and \otimes is the tensor product. Letting the tensor be $\vec{f}(\vec{r} - \vec{r}') = \left[\mathbb{I} - \frac{3\vec{s}\otimes\vec{s}}{|\vec{s}|^2} \right] / |\vec{s}|^3$, the depolarization field can be related to the current density by

$$(4.10) \quad \frac{\partial \vec{E}_d(\vec{r}, t)}{\partial t} = \frac{-1}{4\pi\epsilon_{avg}} \int d^2\vec{r}' \vec{f}(\vec{r} - \vec{r}') \cdot \vec{K}(\vec{r}', t)$$

$\vec{f}(\vec{r} - \vec{r}')$ is related to the Green's function that relates the field to the polarization density and can be computed for more complicated geometries than considered in this work. We see that if $[\sigma(\omega = 0)/\tau] \frac{\partial \vec{E}_d}{\partial t} = -\omega_p^2 \vec{K}$, then in the absence of E_{inc} and dissipation, the current density will oscillate at the frequency ω_p . Comparing with equation it follows that the current density associated with the plasmon mode satisfies the following eigenvalue equation,

$$(4.11) \quad \frac{\sigma(\vec{r}, \omega=0)}{4\pi\epsilon_{\text{avg}}\tau} \int d^2\vec{r}' \vec{f}(\vec{r} - \vec{r}') \cdot \vec{K}(\vec{r}') = \omega_p^2 \vec{K}(\vec{r})$$

The above equation can be solved for the current densities \vec{K}_m and the frequencies ω_{pm} associated with the plasmon modes in any graphene structure. The modes satisfy the orthogonality condition,

$$(4.12) \quad \int d^2\vec{r} \vec{K}_m(\vec{r}) \cdot \vec{K}_p(\vec{r}) / \sigma(\vec{r}, \omega = 0) \propto \delta_{mp}$$

For the case of bulk plasmons, equation reproduces the result of equation. Solving the eigenvalue equation numerically for the case of a single infinitely long graphene strip, we obtain the following result for the frequency of the two lowest plasmon modes,

$$(4.13) \quad \omega_{p0} \approx \sqrt{\frac{\sigma(\omega=0)1.156}{\epsilon_{\text{avg}}\tau W}}$$

$$(4.14) \quad \omega_{p1} \approx \sqrt{\frac{\sigma(\omega=0)2.751}{\epsilon_{\text{avg}}\tau W}}$$

The computed current and charge densities for the two lowest two plasmon modes are shown in figure 4.4

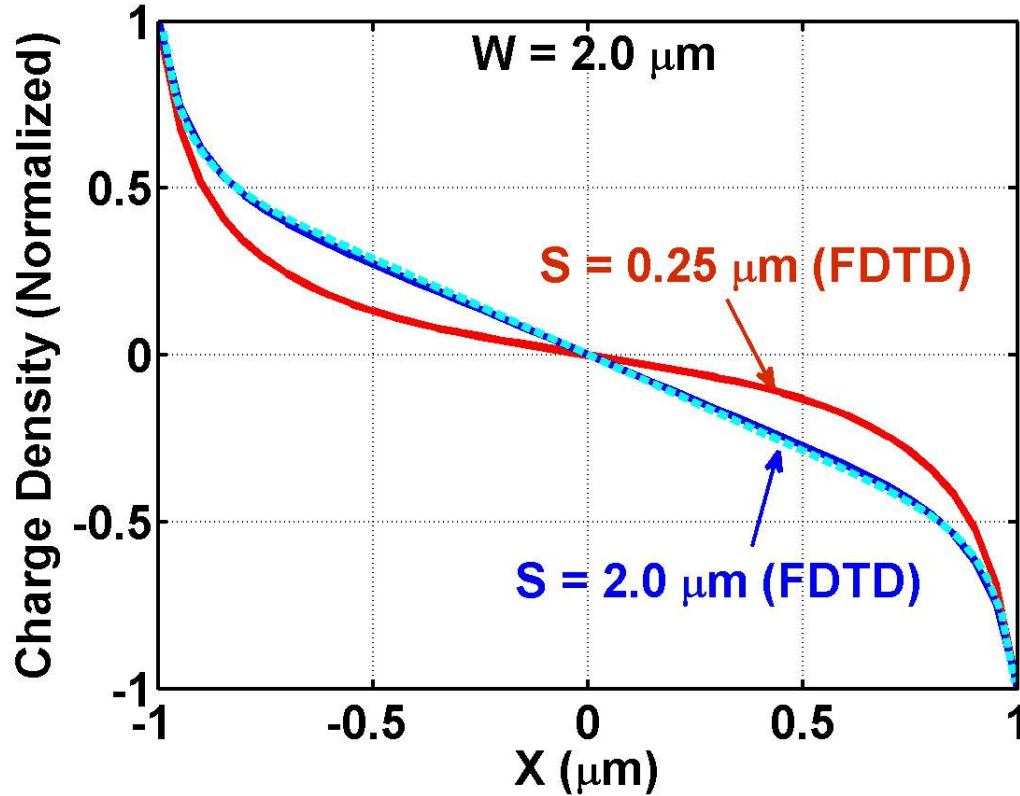


Figure 4.4: The computed charge densities for the lowest plasmon mode in an isolated graphene strip ($S/W \gg 1$) and in an array of strips with $S/W = 0.25$ are plotted. The charge densities were computed using FDTD ($S/W \gg 1$ and $S/W = 0.25$) and the eigenvalue equation (Eq.4.11) ($S/W \gg 1$).

Although all even plasmon modes (0,2,4,...) will couple with normally incident radiation, only the lowest plasmon mode will couple appreciably. The scaling of the plasmon frequency with $1/\sqrt{W}$ is in perfect agreement with our data. For the case $W = 1 \mu\text{m}$, using equation and the extracted values of $\sigma(\omega = 0)$ and τ , $\omega_p 0$ is $\approx 211 \text{ cm}^{-1}$. The eigenvalue equation more accurately models the plasma resonance than Equation with $q = \pi/W$ but it still overestimates the measured resonance frequency by $\approx 6.5\%$. We next address the possible origins of this discrepancy.

Interactions among plasmon modes in neighboring strips can be included by solving equation using $\sigma(\vec{r}, \omega = 0)$ appropriate for an array of graphene strips. Interactions lift

the degeneracy among strips and result in a band of plasmon modes that are the supermodes of the array. The computed current density for the lowest five modes of an array containing nine strips is shown in figure. Only the lowest supermode couples appreciably to the normally incident radiation, and it is the frequency of this supermode that is measured in our transmission experiments. Unfortunately the matrix eigenvalue equation obtained from equation is not sparse so obtaining solutions for large arrays is computationally prohibitive. Starting from the lowest plasmon mode of a single strip, the perturbation technique can be used to obtain an expression for the frequency $\omega_p(n,N)$ and the current density $\vec{K}(n,N)(\vec{r})$ of the n^{th} supermode ($n=0,\dots,N-1$) of an N -strip array,

$$(4.15) \quad \omega_p^2(n,N) \approx \omega_{p0}^2 \left(1 - 2\Delta_1 \cos \left(\pi \frac{n+1}{N+1} \right) \right)$$

$$(4.16) \quad \vec{K}(n,N)(\vec{r}) \approx \sum_{j=1}^N \vec{K}_0(\vec{r} - j(S+W)\hat{x}) \sin \left(\pi j \frac{n+1}{N+1} \right)$$

where Δ_1 is the first-nearest-neighbour interaction parameter. Including second-nearest-neighbour interactions, $\omega_p^2(0,\infty) = \omega_{p0}^2(1 - 2\Delta_1 - 2\Delta_2)$. Where Δ_1 and Δ_2 are given by the expression

$$(4.17) \quad \Delta_\theta = - \frac{\int d^2\vec{r} \int d^2\vec{r}' \vec{K}_0(\vec{r}) \cdot \vec{f}(\vec{r}-\vec{r}') \cdot \vec{K}_0(\vec{r}'-\theta(S+W)\hat{x})}{\int d^2\vec{r} \int d^2\vec{r}' \vec{K}_0(\vec{r}) \cdot \vec{f}(\vec{r}-\vec{r}') \cdot \vec{K}_0(\vec{r}')}$$

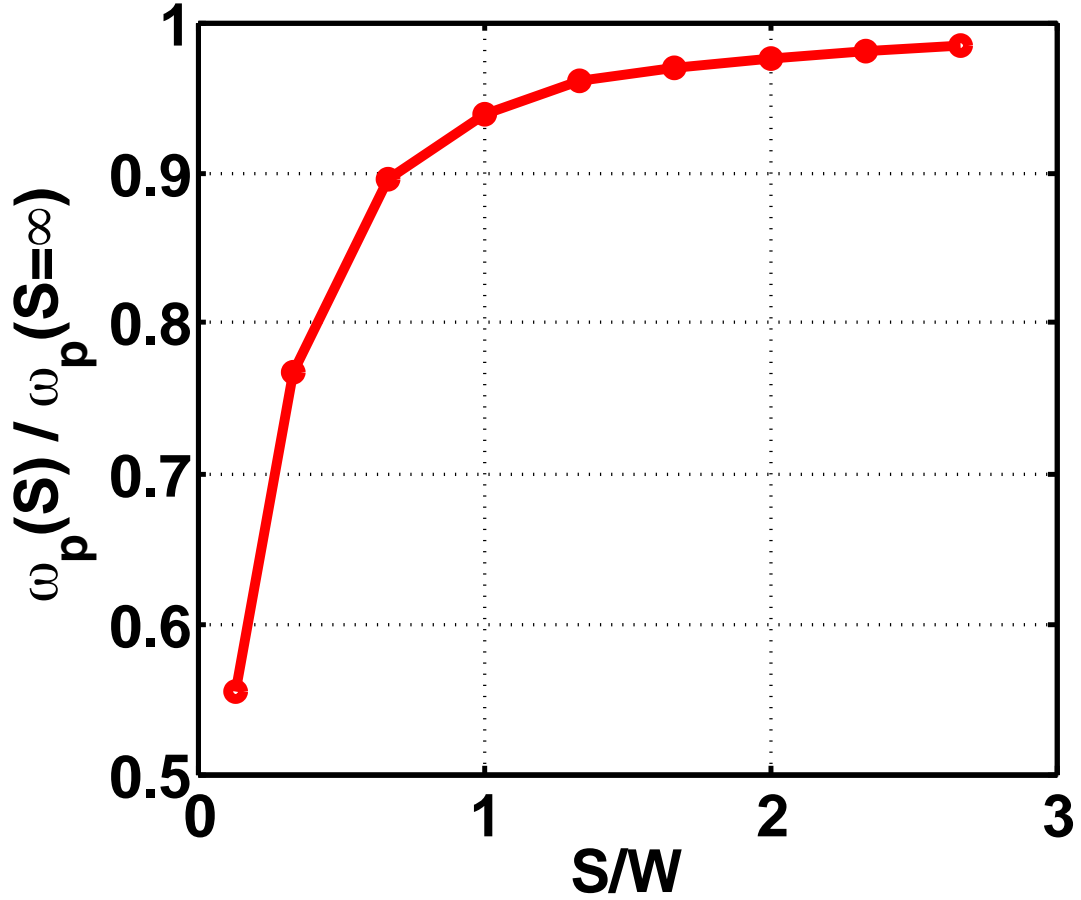


Figure 4.5: The frequencies of the lowest plasmon supermode $\omega_p(0,\infty)$ of an infinite graphene strip array calculated using perturbation theory and FDTD are plotted as a function of the ratio S/W .

Figure 4.5 shows the calculated values of $\omega_p^2(0,\omega)$ as a function of strip spacing S assuming first and second nearest neighbor interactions. The plasmon frequency is reduced as a result of the interactions among neighbouring strips. For $S = W = 1 \mu\text{m}$, the values of $\Delta 1$ and $\Delta 2$ are 0.035 and 0.009 respectively, resulting in a $\approx 4.5\%$ decrease in the value of $\omega_p(0,\infty)$ compared to ω_{p0} . In this case, $\omega_p(0,\infty)$ is approximately 202 cm^{-1} , which is closer to the measured 197 cm^{-1} than ω_{p0} alone. These results suggest that interactions cannot be ignored between nearby graphene plasmonic structures.

The eigenvalue equation does not include retardation effects which could be important for large arrays since the field wavelength would be comparable to the length of the resonator and it is possible for the sheet charge to change over one period. It also does not account for the discontinuity in the field at the oxide/silicon interface (screening by the silicon substrate). A technique is needed that incorporates these effects, can be used to determine the accuracy of equation and can also compute the spectra more accurately than equation. For example equation predicts $T_{\xi=0}(\omega = 0) = T_{\xi=1}(\omega = \omega_p)$, but the measured values in figure differ by $\approx 1.5\%$. The discrepancy arises because the transmission through the gaps in the strip array cannot be modeled simply with a fill factor f , especially when the incident radiation is polarized perpendicular to the strips and $S \leq W$.

4.4 Numerical modeling of graphene plasmons

We use the finite difference time domain method, which lies between the quasi-static method and the ray-tracing method. In the FDTD method[29] we discretize maxwell's equations in time and space so as to obtain an update equation which we can then compute on a mesh. In terms of implementation we use two different arrays, one for the electric field and one for the magnetic field so it is more efficient computationally. An important parameter is the Courant number which has to do with the update coefficients and determines the stability of the simulation. Essentially the wave should propagate less than a mesh grid point over one time step so that errors do not accumulate over the course of the simulation. This places a constraint on the duration of the simulation and the domain size of the simulation. In order to model plasmons, we include an auxiliary equation for the graphene current density (Eq 4.3 without the extra time derivative) and

step the equations using Yee's leap-frogging algorithm[29]. This approach naturally handles interactions and electromagnetic retardation. A challenge in the FDTD technique is the range of length scales important to the problem. The radiation frequencies of interest have free-space wavelengths extending up to 300 μm , but the corresponding plasmon wavelengths are on the order of 1 μm . Furthermore, it is important for the modeled graphene thickness to be much less than the plasmon wavelength. Therefore, the length scales of importance span three orders of magnitude, necessitating a highly non-uniform mesh, with grid steps varying from 0.01 – 0.5 μm . The computational domain spans more than 200 by 200 μm^2 and is surrounded by perfectly matched layer boundaries. We use the values of $4\epsilon_0$ and $12\epsilon_0$ for the THz dielectric constants of SiO_2 and Si respectively. Plasmonic structures are excited at zero angle of incidence with a broadband (0.5-15 THz) pulse of electromagnetic radiation. The transmission spectra for fields polarized parallel and perpendicular to the strips are obtained by Fourier-transforming the time-domain transmitted pulse. Values of $\sigma(\omega=0)$ and τ used in simulations were iteratively improved until the simulated transmission spectra for both polarizations optimally fit the measured spectra.

The FDTD simulation results shown in figure 4.3 accurately fit the measurements. Extracted values of $\sigma(\omega=0)$ and τ lie in the range 0.91-0.95 mS and 29.5-31.5 fs, respectively. Using the expression for graphene conductivity in [28], these values correspond to doping densities of $5.0\text{-}5.2 \times 10^{12} \text{ cm}^{-2}$, consistent with the densities determined using the raman technique. Small variations in the parameters across the CVD graphene sample are consistent with those measured by terahertz spectroscopy in similar samples[30]. The ability of the FDTD technique to quantitatively fit the depth

and width of the plasmon resonances, while also predicting their center frequencies to an accuracy within one percent, underscores its usefulness as a tool for modeling graphene plasmonic structures.

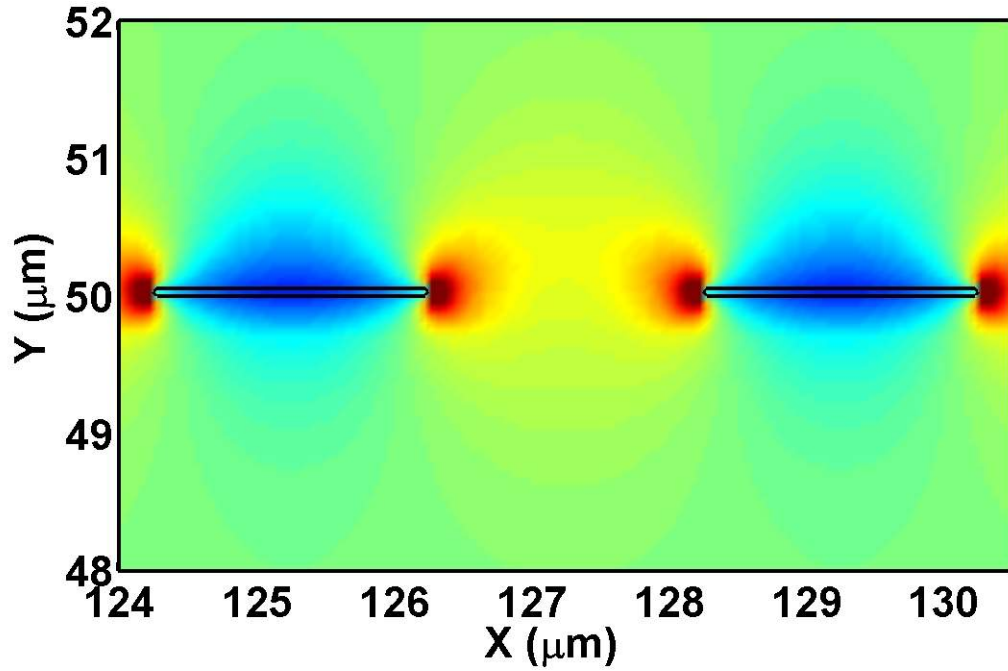


Figure 4.6(a): FDTD simulation result for x-component of electric field for the lowest order plasmon supermode in graphene strips of spacing $2\mu\text{m}$

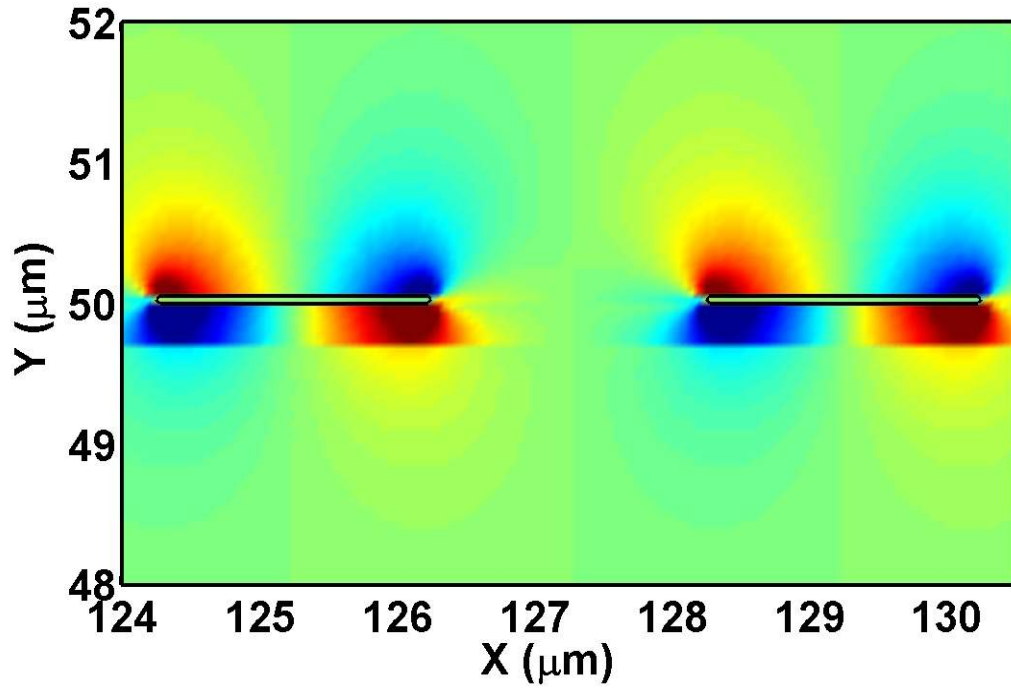


Figure 4.6(b): FDTD simulation result for y-component of electric field for the lowest order plasmon supermode in graphene strips of spacing $2\mu\text{m}$

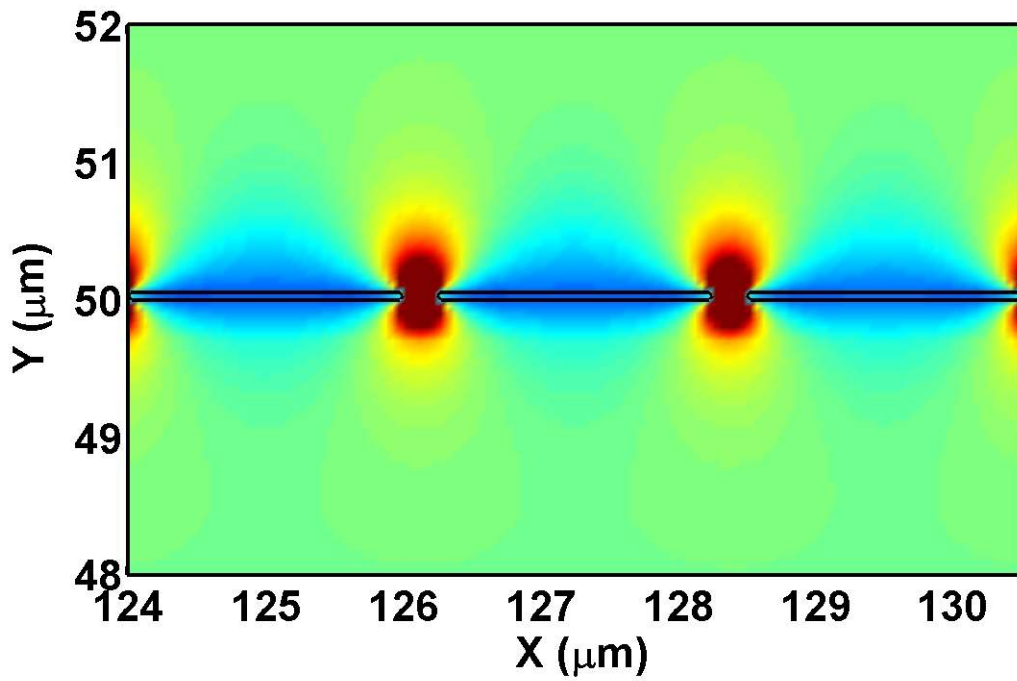


Figure 4.6(c): FDTD simulation result for x-component of electric field for the lowest order plasmon supermode in graphene strips of spacing $0.25\mu\text{m}$

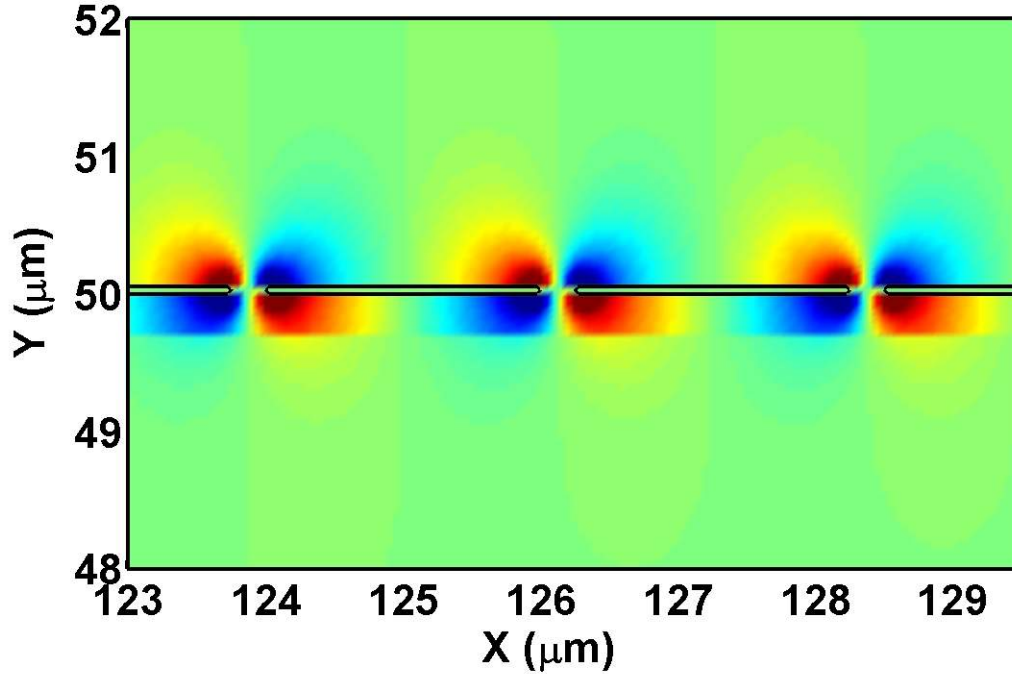


Figure 4.6(d): FDTD simulation result for y-component of electric field for the lowest order plasmon supermode in graphene strips of spacing $0.25\mu\text{m}$

The computed x and y-components of the electric field for the lowest plasmon supermode are shown in Fig 4.6. For arrays of graphene strips with two different spacings ($S=2, 0.25 \mu\text{m}$ and $W = 2 \mu\text{m}$). The locations of the graphene strips are indicated by the thin black lines at $y = 50 \mu\text{m}$. The dashed lines indicate the locations of the silicon/oxide and oxide/air interfaces. The field is highly localized near the graphene sheet, extending a distance on the order of the plasmon wavelength. The discontinuity in the normal (y) component of the field at the silicon/oxide interface is also visible. In contrast with the $S = 2.0 \mu\text{m}$ case, when $S = 0.25 \mu\text{m}$, the field in the gaps between the strips is stronger than the field in the center of the strips. This effect helps to reveal the

physical origins of the interaction between neighbouring strips. The plasmon charge density that accumulates at the edges of an isolated strip generates a depolarization field \vec{E}_d with $\omega_{p0}^2 \propto |\vec{E}_d|$. In a strip array, this edge charge density is partially imaged on the neighboring strips, as depicted in Fig 4.2(a). This effect increases the depolarization field in the gaps between strips but reduces the field within each strip. Equivalently, the depolarization fields from neighbouring strips are in-phase in the gaps between strips but out-of-phase in their centers. Therefore, $\omega_p(0,\infty) < \omega_{p0}$. In contrast, in the highest supermode of the array, the current density oscillations in neighbouring strips are out of phase so $\omega_p(N,\infty) > \omega_{p0}$.

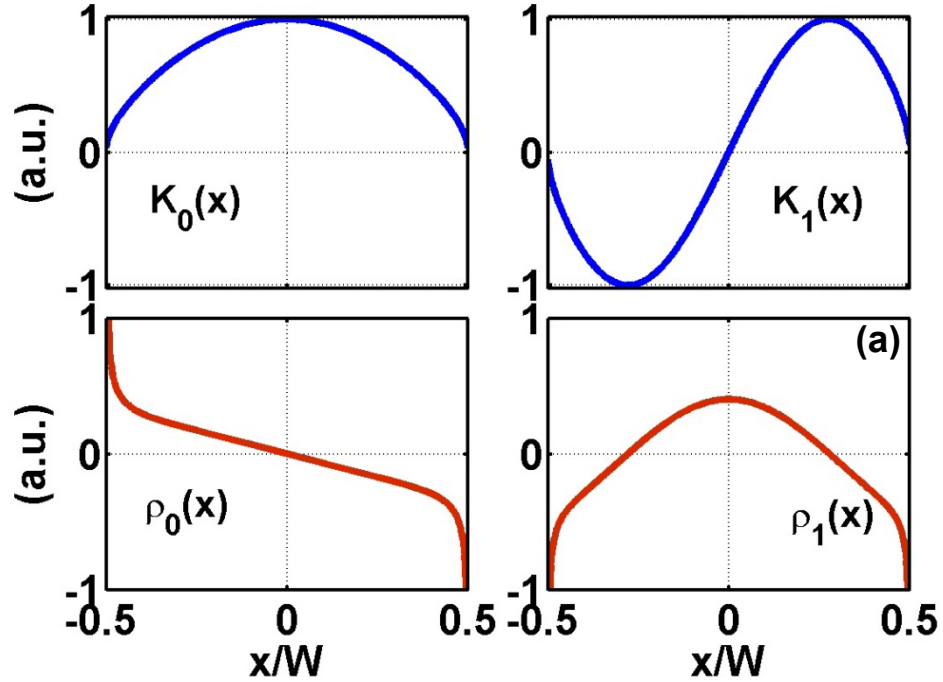


Figure 4.7: The computed current densities $\vec{K}(x)$ (top) and charge densities $\rho(x)$ (bottom) for the lowest two plasmon modes of a graphene strip are plotted.

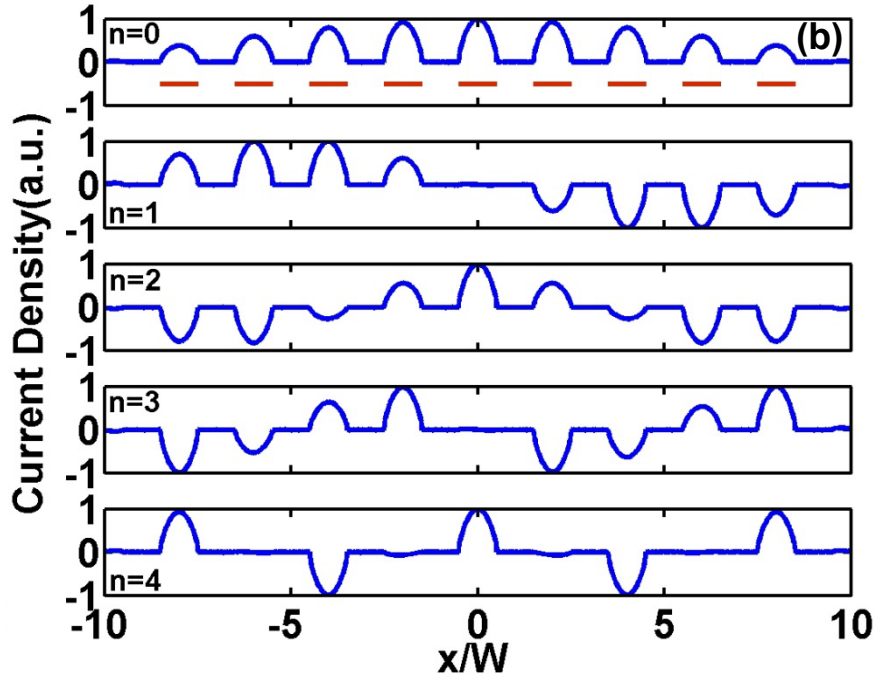


Figure 4.8: The computed current densities are plotted for the first 5 supermodes of an array consisting of 9 graphene strips ($W=S$). Locations of the strips are indicated by the red horizontal lines.

FDTD simulation can serve to evaluate the perturbation theory as shown in Fig 4.5. The two methods are found to agree when $S/W > 1$, but not when $S/W \ll 1$. For example, when $S = W$ in Fig 4(a), the FDTD calculated $\omega_p(0, \infty)$ is lower than ω_{p0} by $\approx 6.5\%$, in contrast with the $\approx 4.5\%$ reduction predicted by the perturbation technique. This behavior can be understood by examining the plasmon charge density. Fig 4.3 shows the FDTD computed charge density in a strip for the lowest order supermode with $S/W \gg 1$ and $S/W = 0.25$. Also shown is the charge density obtained by solving Eq 4.5 for $S/W \gg 1$, which is nearly identical to the FDTD result. But when $S/W \ll 1$, the FDTD calculation reveals that the charge density is significantly modified as a result of interactions; the charge density increases near the strip edges to screen the fields of the neighbouring strips. Since the perturbation theory assumed that the charge and current

densities are unmodified from the lowest plasmon mode of an isolated strip, the results became inaccurate when $S/W \ll 1$. The good agreement obtained between the FDTD method and the analytic model for $S/W > 1$ suggests that retardation effects do not play a significant role in the structures considered in this work.

4.5 Conclusion

To conclude, we presented experimental and theoretical results for the confined plasmon modes in graphene microstructures. We presented an analytic model which captures the essential physics and gives us an eigenvalue equation for computing plasmon modes. We also presented a universally applicable FDTD technique. The theoretical models presented show good agreement with the measurements, and demonstrate the importance of interactions in plasmonics structures. The present work, to the best of our knowledge is the first time that theoretical and numerical models have been presented and tested against experiments for confined plasmon modes in graphene microstructures. The techniques presented can be used to understand, model and design complex graphene plasmonic structures for applications ranging from IR detectors and chemical sensors to plasmonic radiation sources, oscillators, modulators and metamaterials.

CHAPTER 5

GRAPHENE PLASMONS IN THE MID-IR

5.1 Introduction

We wish to extend our study of graphene plasmonics into the mid-IR (wavelength from 3-8 μm) region because the molecular vibrations of many proteins, Lipids and DNA have a unique fingerprint in this region[32]. The phonon modes of graphene and silicon dioxide exist in this region as well, providing us access to some of the damping channels of graphene plasmons by observing plasmon phonon coupling. However studying graphene plasmons in the mid-IR region has been challenging due to the requirement of several tens of nanometer sized features over centimeter sized areas. In this regard several groups have employed expensive electron beam lithography or terahertz objectives which are lossy to get around this challenge[34,35,36,37]. In terms of applications these techniques are not scalable, therefore there is a need to investigate alternative technologies. We introduce a novel process to produce graphene plasmon resonators over large area using block copolymer self-assembly[38]. We measured our devices using FTIR spectroscopy in transmission configuration and confirmed our data by fitting it to a drude model.

5.2 Self-Assembly Process for Plasmon Resonators

We first describe the process flow. Graphene is first grown on CVD copper and transferred to 90nm SiO₂ on a double side polished high resistivity substrate summarized in figure 5.1. The transferred graphene is then dipped in 50% nitric acid for 60 seconds and dried without further rinsing. Next 8nm of SiO₂ is evaporated using electron beam on to the graphene at 0.3 $\text{\AA}/\text{s}$ in 10⁻⁶ Torr vacuum. A 2% random

copolymer in toluene from Polymer Source is spun coat at ramp 10000 rpm and spin speed 2000 rpm on to the SiO₂ and annealed overnight for 24 hours in 30" Hg vacuum at 180C to graft the random copolymer brush on to the evaporated oxide. The backside of the sample is cleaned using acetone to ensure we can obtain a high enough transmission signal through the sample. After that the excess brush is rinsed off by spinning the substrate at 2000 rpm while spraying toluene on to the sample. The sample is then blow dried using nitrogen and a 2% PS-b-PMMA is spun coat on to the brush at 2000 rpm. The PS-b-PMMA, random copolymer brush, oxide, graphene film stack is then annealed overnight for 24 hours in 30" Hg vacuum at 180C. During annealing the PS and PMMA domains phase separate to form perpendicularly aligned cylinders. Since TMAH wets the pmma domain more readily than the PS domain, we infuse the pmma cylinders with alumina by flowing TMAH in a semi-static ALD chamber for an hour. Finally using the alumina pillars as an etch mask, we etch through the PS scaffold and oxide/graphene stack using CF₄/O₂ RIE to produce a substrate with 35nm graphene dots of 20nm spacing.

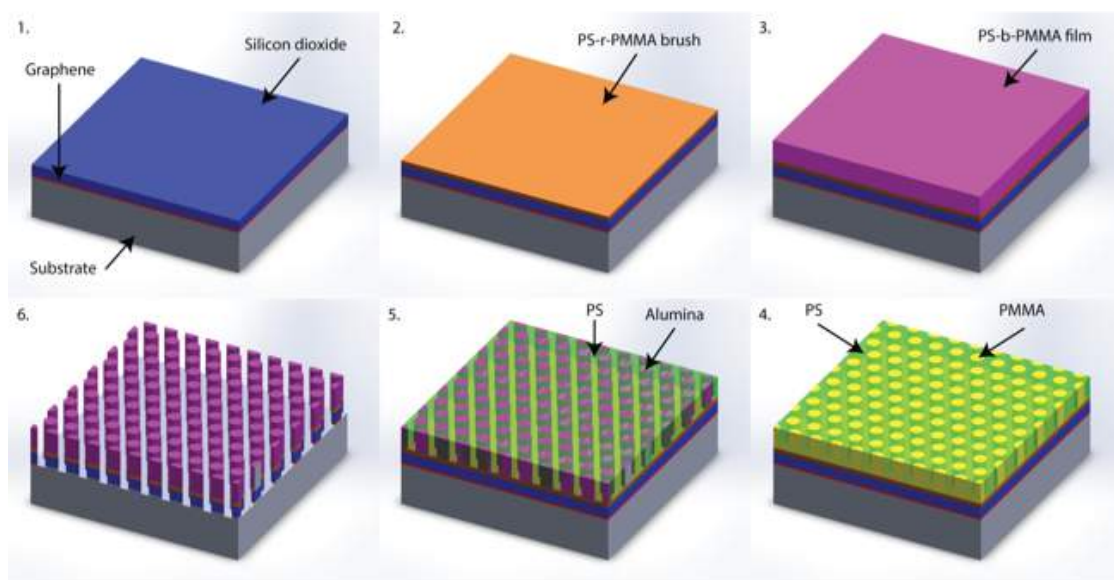


Figure 5.1: Summary of process flow for self-assembled graphene dots

We performed SEM microscopy to demonstrate the uniform distribution of the dots over large areas as shown in Figure 5.2.

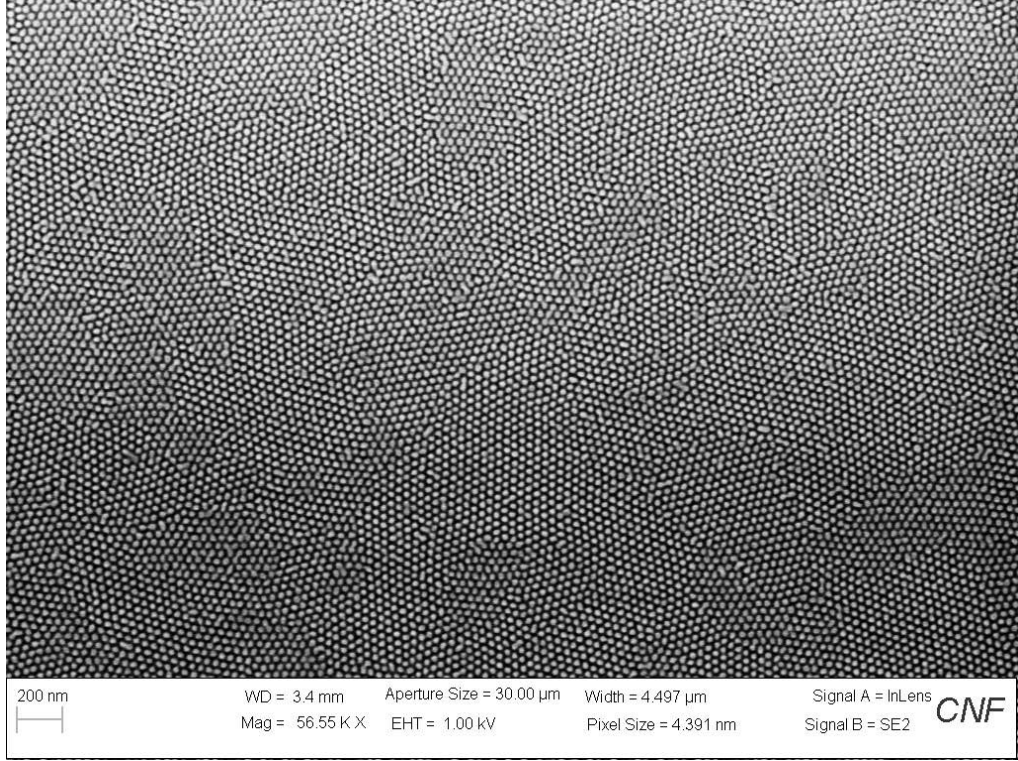


Figure 5.2: SEM image of self-assembled 36nm resonators covering 1cm by 1cm area

5.3 Contribution to Damping from Self-Assembly Process

Following the previous chapter we model graphene by solving for the sheet current density $\vec{K}(\vec{r})$ in the graphene which satisfies

$$(5.1) \quad \frac{\partial^2 K_i(\vec{r})}{\partial t^2} + \frac{\partial K_i(\vec{r})}{\partial t} = \frac{\sigma_0 s(\vec{r})}{\tau} \left[\frac{\partial E_{inc,i}(\vec{r})}{\partial t} - \frac{1}{\epsilon_{avg}} \int d\vec{r}' f_{ij}(\vec{r} - \vec{r}') K_j(\vec{r}') \right]$$

and which can be simplified and rearranged in frequency domain to

$$(5.2) \quad \int d\vec{r}' \left[\frac{1-i\omega\tau}{\sigma_0} \delta_{ij} \delta(\vec{r} - \vec{r}') - \frac{s(\vec{r}) f_{ij}(\vec{r}-\vec{r}')}{i\omega\epsilon_{avg}} \right] K_j(\vec{r}') = s(\vec{r}) E_{inc,i}(\vec{r})$$

Here σ_0 is the zero-frequency conductance of graphene, τ is the relaxation time of

carriers in graphene, ϵ_{avg} is the average dielectric constant of the surrounding medium, and \vec{E}_{inc} is the incident electromagnetic field. The shape function $s(\vec{r})$ is 1 where graphene is present and 0 otherwise, and the depolarization kernel is given by

$$(5.3) \quad f_{ij}(\vec{r} - \vec{r}') = \partial_i \partial_j \frac{1}{|\vec{r} - \vec{r}'|}$$

Briefly, the above equation is obtained from Maxwell's equations and the constitutive relation for graphene after neglecting magnetic fields and retardation effects. This model is an excellent approximation for small graphene resonators and allows us to treat assemblies of such resonators much larger than possible with direct electromagnetic simulations.

Expanding the sheet current density and incident field in a set of orthonormal basis functions $\vec{b}_\alpha(\vec{r})$. We can discretize the above equation within the Bobunov-Galerkin approach to

$$(5.4) \quad \left[\frac{1-i\omega\tau}{\sigma_0} \delta_{\alpha\beta} - \frac{1}{i\omega\epsilon_{\text{avg}}} F_{\alpha\beta} \right] K_\alpha = E_{\text{inc},\alpha}$$

where

$$(5.5) \quad F_{\alpha\beta} = \int d\vec{r} \int d\vec{r}' s(\vec{r}) b_{\alpha i}^*(\vec{r}) f_{ij}(\vec{r} - \vec{r}') b_{\beta j}(\vec{r}') s(\vec{r}')$$

and $K_\alpha, E_{\text{inc},\alpha}$ are the expansion coefficients of the $\vec{K}(\vec{r}), \vec{E}_{\text{inc}}(\vec{r})$ in the basis.

For the case of dots, a cylindrical basis centered on each dot is the most convenient choice. Neglecting retardation effects, the fields are curl-less and hence the basis functions are gradients of some scalar field. Therefore, we choose the basis

$$(5.6) \quad \vec{b}_{mn}(\vec{r}) = c_{mn} \nabla \left[J_m \left(\frac{y_{mn} r}{R} \right) e^{im\varphi} \right]$$

For a dot of radius R at the origin, where y_{mn} is the n^{th} root of $J'_m(x) = 0$ so as to impose the Neumann boundary conditions on $K(\vec{r})$ that arise from charge continuity.

Orthonormality of these basis functions constrains

$$(5.7) \quad c_{mn} = 1/\sqrt{\pi(y_{mn}^2 - m^2)J_m^2(y_{mn})}$$

We can analytically expand a unit incident polarized plane wave in this basis with the coefficients

$$(5.8) \quad E_{inc}^{mn} = \pi R c_{mn} \delta_{|m|1} J_m(y_{mn})$$

With a spatial fourier transform and exploiting the convolution theorem, we can simplify the depolarization field kernel coefficients $F_{\alpha\beta}$ to a one dimensional integral over dimensionless wave vector magnitude $g = kR$,

$$(5.9) \quad F_{mn,m'n'} = \frac{(2\pi)^2 \delta_{mm'}}{R} \int_0^\infty dg \beta_{mn}(g) \beta_{m'n'}(g)$$

which we perform numerically straightforwardly. Above, $\beta_{mn}(g)$ is related to the Fourier transform of $\nabla \cdot \vec{b}_{mn}(\vec{r})$ and simplifies analytically to

$$(5.10) \quad \beta_{mn}(g) = c_{mn} y_{mn}^2 \int_0^1 dx x J_m(gx) J_m(y_{mn}x) =$$

$$c_{mn} y_{mn}^2 \frac{y_{mn} J_{m-1}(y_{mn}) J_m g - g J_{m-1}(g) J_m y_{mn}}{g^2 - y_{mn}^2}$$

For a single dot, we therefore get a block diagonal equation in m which can be diagonalized to get the eigenmodes, or inverted easily to calculate the response to incident fields of various frequencies.

Since broadening is important in many applications for example biosensing[39] or emission studies[40] of the plasmons, we would like to characterize the broadening observed. We distinguish between process specific and process independent broadening. Process independent broadening include processes such as electron phonon coupling[41], electron electron scattering[42] and defects in the material itself[43]. Whereas process dependent broadening here refers to broadening due to edge

roughness[44], doping variations, coupling between neighboring resonators[45], size distribution of the individual resonators, defects and grain boundaries[46] in the self assembled block copolymer film.

We first examine the disorder due to defects and grain boundaries in our self-assembled block copolymer film. The presence of impurities on the surface of the silicon oxide layer may generate nonuniformities in the surface energy as well as block the adhesion of the random copolymer brush which gives rise to defects in the block copolymer film. In order to mitigate this effect, we spun Acetone and isopropyl alcohol on the silicon oxide film before applying the random copolymer brush. Due to the size of the polymer chains there is limited mobility even at high annealing temperatures and this causes the formation of grains and grain boundaries. In order to account for the disorder in our film we extract the positions of the individual dots from our SEM data and set the $s(\vec{r})$ function in our model to 1 where graphene is present and 0 otherwise assuming dots of uniform radii. We perform simulation of our resonators assuming uniform doping and a block copolymer film with perfect translation and orientation correlation and observe that for such an array of resonators, the broadening is 10cm^{-1} while for a sample with our disorder again assuming uniform doping we have a broadening of 57cm^{-1} .

Next we examine the effect of coupling between neighbouring dots, which arises because the depolarization field due to each dot is non-zero at its neighbours, and analyze the resulting resonant frequency shifts and coupled mode shapes. In the cylindrical basis derived above, the depolarization field matrix elements between dots of radii R_1 and R_2 centered at \vec{r}_1 and \vec{r}_2 generalizes straightforwardly using the spatial Fourier transform to

$$(5.11) \quad F_{\vec{r}_1 m_1 n_1, \vec{r}_2 m_2 n_2} = (2\pi)^2 e^{i(m_1 - m_2)\phi_{21}} \int_0^\infty dk \beta_{m_1 n_1}(kR_1) \beta_{m_2 n_2}(kR_2) J_{m_1 - m_2}(kr_{21})$$

where (r_{21}, ϕ_{21}) are the polar coordinates of the separation vector $\vec{r}_2 - \vec{r}_1$. Since we still only need to calculate a one-dimensional integral numerically, we can easily construct and solve the discrete matrix governing the response of a collection of thousands of dots, whose positions and sizes we directly obtain from the SEM images.

To consider the effects of various types of imperfections in the structure, we consider several combinations of the possible non-idealities: size variation, coupling, positional disorder and doping variation.

Assuming uniform doping of the dots we see a shift in our resonance frequency of 129 cm^{-1} wavenumber and a broadening of 10.3 cm^{-1} vs 1.8 cm^{-1} for the isolated dot.

The third contribution to broadening is dopant distribution. Ideally a disk geometry should provide the lowest number of modes and hence the lowest broadening, the trade-off is that since the disk is an isolated structure we are unable to use electrostatic doping as any metals above or below will cause substantial damping, hence the use of chemical doping in our case, although surface doping may be a promising direction for future work. To account for the contribution of doping, we compare an array of resonators without defects or grain boundaries with a poisson doping distribution and with a uniform doping distribution. In the former case, the calculated broadening is 10 cm^{-1} and in the latter case the broadening is 16 cm^{-1} .

Lastly we would like to check for size dispersion of our individual resonators. Size dispersion in our devices can be caused by a nonuniform BCP film thickness but by positioning the 1 inch by 1 inch graphene sheet in the middle of the 50 cm by 50 cm

wafer we can minimize this effect. As mentioned previously we also maintained the cleanliness of the wafer backside so that the sample stays flat during plasma processing. We extract the size dispersion from our SEM data and assume a uniform dopant distribution as well as an array without defects or grain boundaries. Here we again employ the $s(\vec{r})$ function but we incorporate the actual size dispersion of the dots not just the positions. The broadening in our array assuming uniform doping is 60 cm^{-1} . Finally we look at the cumulative effect of these contributions to broadening. The broadening observed in this case is 55.8 cm^{-1} .

5.4 Contribution to Damping from Phonon Coupling

Now we turn our attention to the fundamental damping mechanisms for graphene plasmons in the mid-IR which will form a lower bound on the quality factor of graphene plasmonic devices. Similarly to the approach we used previously we start from the current density equation

$$(5.12) \quad \frac{\partial^2 \vec{K}(\vec{r}, t)}{\partial t^2} + \frac{1}{\tau} \frac{\partial \vec{K}(\vec{r}, t)}{\partial t} = \frac{\sigma(\vec{r}, \omega=0)}{\tau} \frac{\partial}{\partial t} [\vec{E}_{inc}(\vec{r}, t) + \vec{E}_d(\vec{r}, t)]$$

where $\vec{K}(\vec{r}, t)$ is the current density, τ is the relaxation time, $\sigma(\vec{r}, \omega = 0)$ is the graphene DC conductivity and $\vec{E}_{inc}(\vec{r}, t)$ and $\vec{E}_d(\vec{r}, t)$ are the incident excitation field and depolarization field from the dipole built up respectively. We first relate the depolarization field to the current density using charge continuity, where $\bar{f}(\vec{r} - \vec{r}')$ is the green's function relating field to the polarization density

$$(5.13) \quad \frac{\partial \vec{E}_d(\vec{r}, t)}{\partial t} = \frac{-1}{4\pi\epsilon_{avg}} \int d^2\vec{r}' \bar{f}(\vec{r} - \vec{r}') \cdot \vec{K}(\vec{r}', t)$$

and note that in order to have plasmon oscillation we must have

$$(5.14) \quad \frac{\sigma(\vec{r}, \omega=0)}{\tau} \frac{\partial \vec{E}_d(\vec{r}, t)}{\partial t} = -\omega_p^2 \vec{K}(\vec{r}, t)$$

then by combining everything we obtain an eigenvalue equation describing the plasmon modes in graphene,

$$(5.15) \quad \frac{\sigma(\vec{r}, \omega=0)}{4\pi\epsilon_{avg}\tau} \int d^2\vec{r}' \vec{f}(\vec{r} - \vec{r}') \cdot \vec{K}(\vec{r}) = \omega_p^2 \vec{K}(\vec{r})$$

Next we can expand the current density in terms of the modes of the graphene disk as follows

$$(5.16) \quad \vec{K}(\vec{r}, t) = \sum_m a_m(t) \vec{K}_m(\vec{r})$$

where for a sinusoidal incident field we have

$$(5.17) \quad \vec{E}_{inc}(\vec{r}, t) = \vec{E}_{inc}(\vec{r}, \omega) e^{-i\omega t}$$

$$(5.18) \quad a_m(t) = a_m(\omega) e^{-i\omega t}$$

Solving for $a_m(\omega)$ we obtain

$$(5.19) \quad a_m(\omega) = \frac{i\omega\tau}{\omega^2 - \omega_{pm}^2 + i\omega\tau} \frac{\int d^2\vec{r} \vec{K}_m(\vec{r}) \cdot \vec{E}_{inc}(\vec{r}, \omega)}{\int d^2\vec{r} \frac{\vec{K}_m(\vec{r}) \cdot \vec{K}_m(\vec{r})}{\sigma(\vec{r}, \omega=0)}}$$

where $a_m(\omega)$ is the amplitude of the plasmon eigenmode and when $\omega = \omega_{pm}$ we obtain a pole at the plasmon frequency. We fit this equation to different graphene structures and obtain a good fit in terms of the resonance frequency as well as the width of the resonance. The fitting parameters are the size of the plasmon cavity, the conductivity, the relaxation time and the doping. The cross section SEM of the devices is shown in figure 5.3 and the fitting is shown in the figures 5.4 and 5.5.

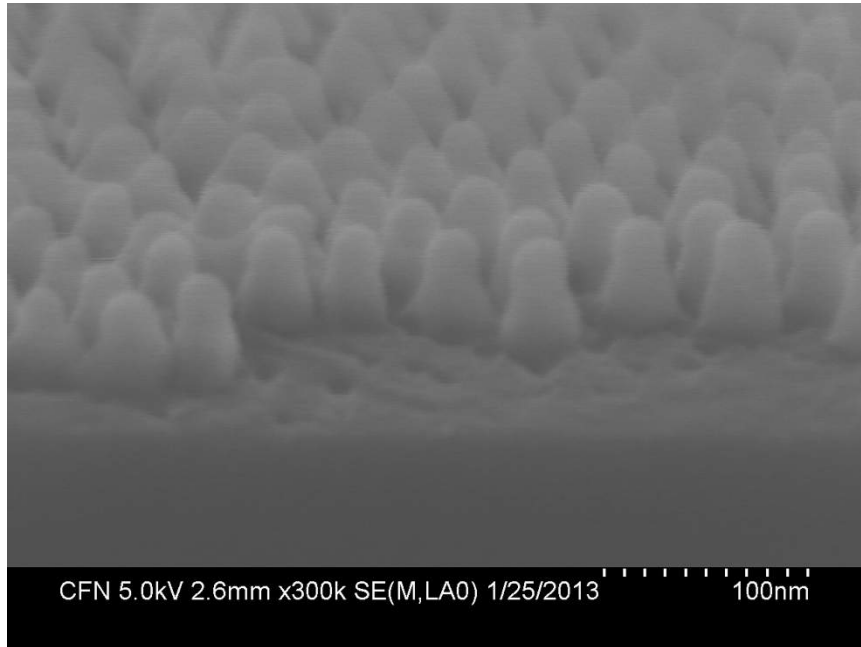


Figure 5.3: Cross section of the sample showing the etched through pillars containing the graphene dot. The dot is located between the light and dark regions of the pillar since below the dot is SiO_2 and on top is Al_2O_3 , as a result the dot might be 1-2nm smaller or larger depending on the etch conditions.

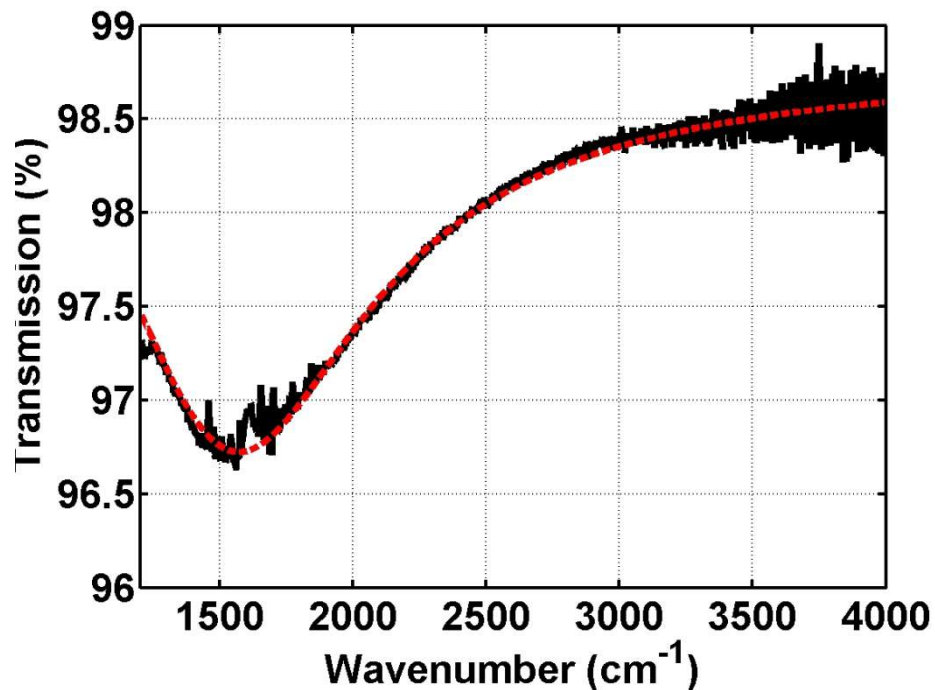


Figure 5.4: Absorption spectra of 23nm radius dots. The black curve is data and the red curve is theory. The extracted conductivity $\sigma(\omega = 0)$ is 0.4mS and the extracted scattering time τ is 4.7fs. The estimated fermi level is 225meV

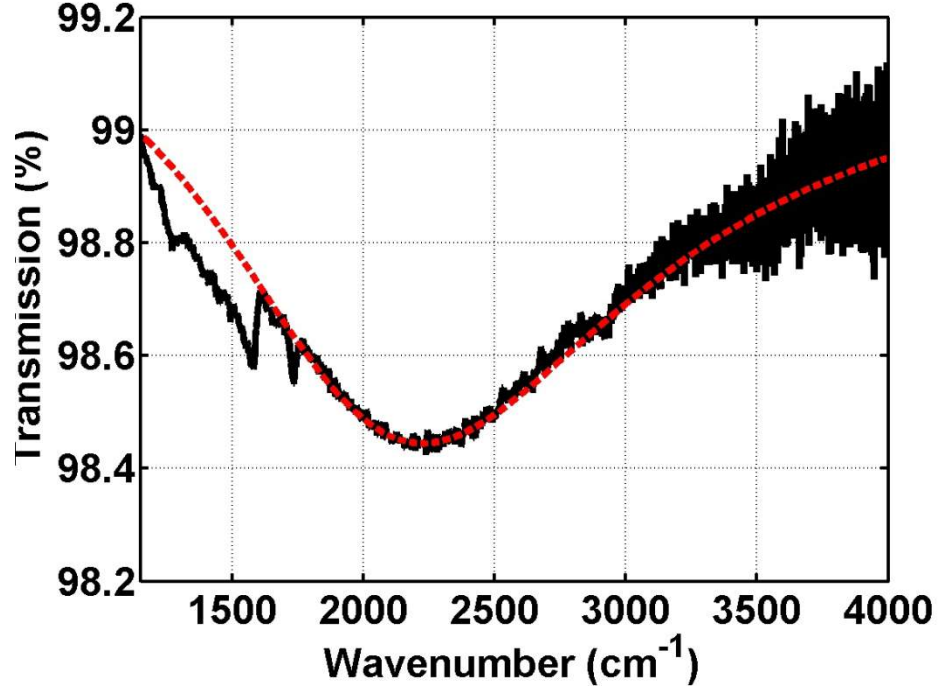


Figure 5.5: Absorption spectra of 16nm radius dots. The black curve is data and the red curve is theory. The extracted conductivity $\sigma(\omega = 0)$ is 0.55mS and the extracted scattering time τ is 2.75fs. The estimated fermi level is 225meV

Using the expression for carrier concentration,

$$(5.20) \quad n(E_f) = \frac{1}{\pi} \left(\frac{E_f}{\hbar V_f} \right)^2$$

where $\hbar = 6.58 \times 10^{-16} \text{ eVs}$ and $V_f = 1.0 \times 10^6 \text{ ms}^{-1}$, we estimate that each dot has only 200-300 carriers which implies that we are in the few electron regime where a small change in doping will result in a large shift in resonance frequency so that few electron plasmonics are possible. To investigate the origin of the plasmon damping further we plot the damping time as a function of frequency in figure 5.6,

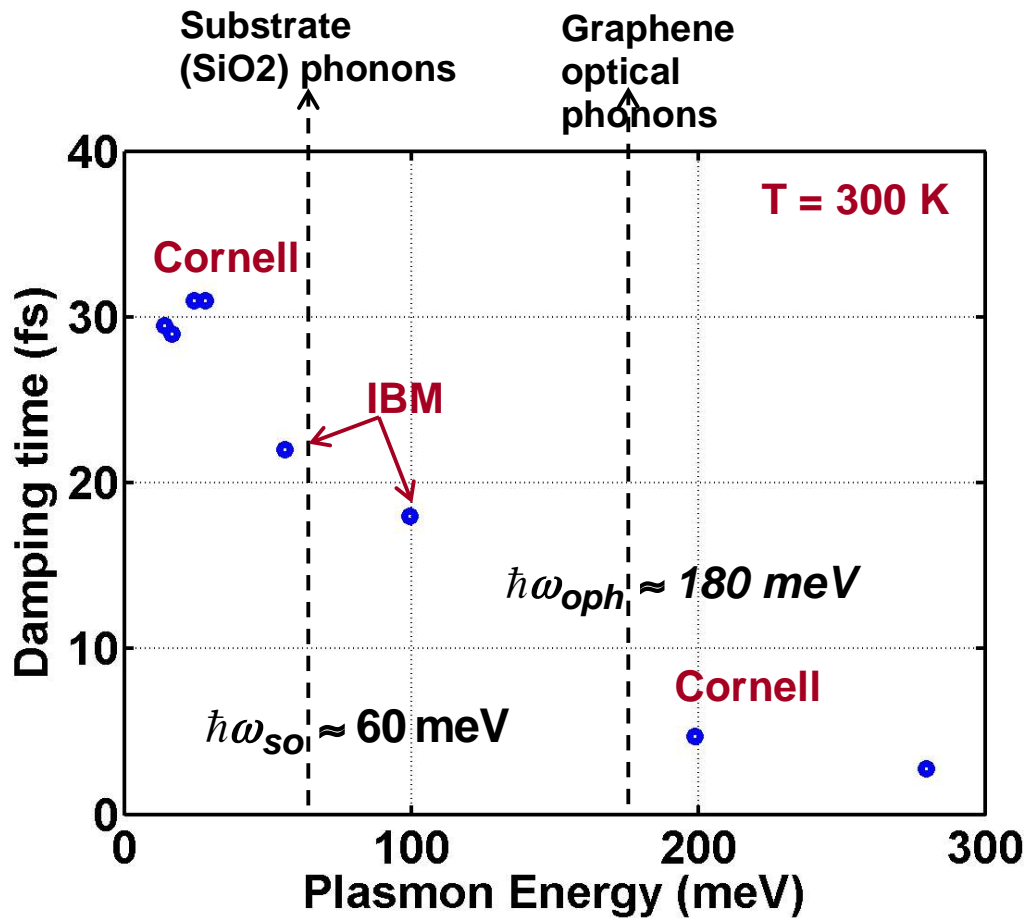


Figure 5.6: Plot of damping time as a function of plasmon resonance frequency. Damping time is increasing with frequency pointing to fabrication challenges or loss mechanisms that increase with frequency

We see that the plasmon losses increase dramatically at higher frequencies and this points to phonon-coupling losses, substrate surface optical phonon losses, edge roughness scattering, size dispersion or Landau damping due to plasmon confinement as possible loss mechanisms.

5.4.1 Damping from Substrate Phonons

If we look back at our transmission spectra for our dots, we see that there is a fairly large feature observed around 1100 cm^{-1} near where the silicon oxide optical phonon is located as shown in figure 5.7,

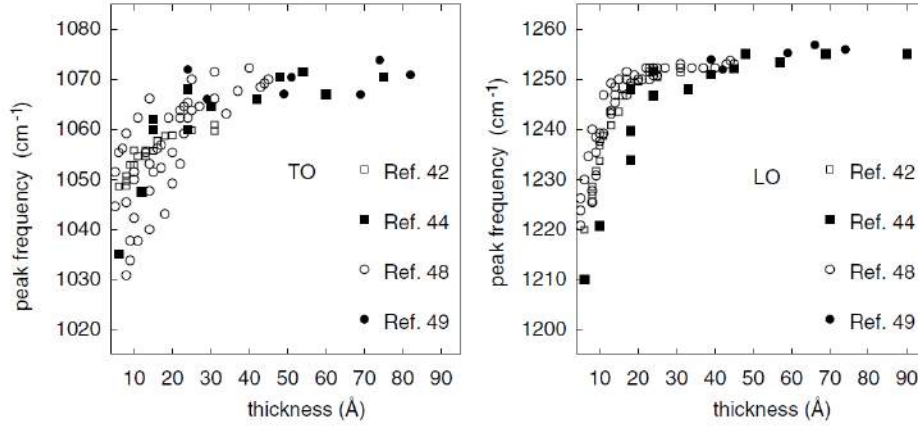


Figure 5.7: Location of SiO₂ optical phonons as a function of oxide film thickness[47]

So we ask whether it is the case that the plasmon in the graphene dot is interacting with the silicon oxide optical phonon. The physical picture is that the depolarization field extends into the silicon oxide, this field is screened by the frequency dependent oxide permittivity and as a result the effective dielectric constant surrounding the plasmon becomes frequency dependent. We describe the substrate permittivity using the expression below,

$$(5.21) \quad \epsilon_S(\omega) = \epsilon_S(\infty) \left[\frac{\omega^2 - \omega_{LO}^2 + i\omega\gamma}{\omega^2 - \omega_{TO}^2 + i\omega\gamma} \right]$$

The average dielectric constant felt by the plasmons is then given by

$$(5.22) \quad \epsilon_{avg}(\omega) = \frac{\epsilon_0 + \epsilon_S(\omega)}{2} = \frac{\epsilon_0}{2} + \frac{\epsilon_S(\infty)}{2} \left[\frac{\omega^2 - \omega_{LO}^2 + i\omega\gamma}{\omega^2 - \omega_{TO}^2 + i\omega\gamma} \right]$$

We can incorporate this into our model for the plasmon by introducing a frequency dependent oxide permittivity from the previous equation into the eigenvalue expression,

$$(5.23) \quad iw\vec{E}_d(\vec{r}, \omega) = \frac{1}{4\pi\epsilon_{avg}(\omega)} \int d^2\vec{r}' \vec{f}(\vec{r} - \vec{r}') \cdot \vec{K}(\vec{r}, \omega)$$

The original plasmon response equation now becomes,

$$(5.24) \quad a(\omega) = \frac{i\omega/\tau}{\left[\omega^2 + i\frac{\omega}{\tau} - \frac{\epsilon_{avg}(\infty)}{\epsilon_{avg}(\omega)} \omega_p^2 \right]} \frac{\int d^2\vec{r} \vec{K}(\vec{r}) \cdot \vec{E}_{inc}(\vec{r}, \omega)}{\int d^2\vec{r} \frac{\vec{K}(\vec{r}) \cdot \vec{K}(\vec{r})}{\sigma(\vec{r}, \omega=0)}}$$

We fit this to our data using the fitting parameters $\gamma_{LO} = 8 \text{ ps}^{-1}$ and $\gamma_{TO} = 2 \text{ ps}^{-1}$ and obtain a good fit to the feature around 1100 cm^{-1} as shown in the figure 5.8

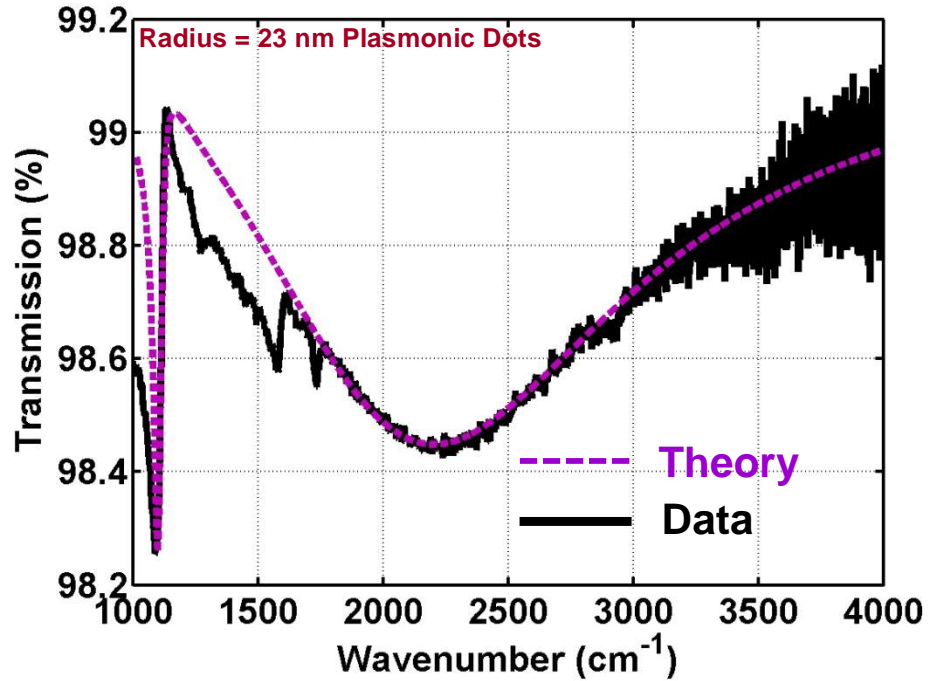


Figure 5.8 Fit of longitudinal and transverse optical phonon decay rates to the absorption spectra for 23nm radius plasmonic dots. The transverse optical decay rate is 2 ps^{-1} and the longitudinal optical phonon decay rate is 8 ps^{-1} [48,49]

5.4.2 Damping from Graphene Phonons

Referring back to the transmission spectrum above, we also observe another smaller feature around 1500 cm^{-1} and recalling our raman spectrum of graphene the G-peak and the D-peak are located in the vicinity of this wavenumber so it could be that the plasmon is also coupling to the graphene optical phonon since we observe this feature in all our samples and the disorder peak varies from sample to sample.

We start from the idea that the moving electrons cause a local lattice distortion, since the lattice consists of overlapping orbitals and nuclei, which are charge clouds. The local

lattice distortion results in a deformation potential that is then felt by another electron.

We show a cartoon of this effect in figure 5.9,

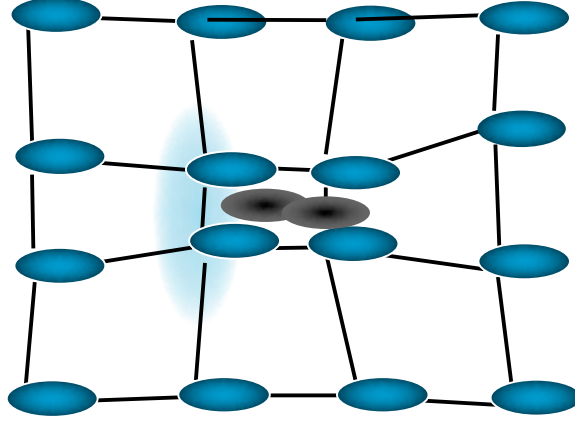


Figure 5.9: Cartoon showing phonon mediated scattering between electrons

We can account for this effect in our model by observing that the interaction between transverse optical phonons and electrons can be expressed in terms of the electron current,

$$(5.25) \quad \hat{H}_{e-ph} = \frac{1}{A} \sum_{\vec{q}} g \left(\hat{b}_{\vec{q}} + \hat{b}_{-\vec{q}}^{\dagger} \right) K(-\vec{q}) = -\frac{1}{A} \sum_{\vec{q}} A_{L-ph}(\vec{q}) K(-\vec{q})$$

where the b's are the phonon creation and annihilation operators and A_{L-ph} is the vector potential description for TO phonons while K remains the current as before. The total vector potential experienced by the electron is then the sum of three parts:

$$(5.26) \quad \vec{A}_{Total} = \vec{A}_{inc}(\vec{q}, \omega) + \vec{A}_{depol}(\vec{q}, \omega) + \vec{A}_{L-ph}(\vec{q}, \omega)$$

We can find the resulting electric field using the total vector potential by

$$(5.27) \quad \vec{E} = -\nabla V - \frac{\partial \vec{A}}{\partial t}$$

where V is the scalar potential and then the original plasmon response equation becomes

$$(5.28) \quad a(\omega) = \frac{i\omega\tau}{\left[\omega^2 + i\frac{\omega}{\tau} \frac{\epsilon_{avg}(\infty)}{\epsilon_{avg}(\omega)} \omega_p^2 - \frac{\sigma(\omega=0)g^2\omega_{TO}^2}{\tau} \frac{2\omega_{TO}}{e^2\hbar v^2} \frac{2\omega_{TO}}{\omega^2 - \omega_{TO}^2 + i\omega\tau} \right]} \frac{\int d^2\vec{r} \vec{K}(\vec{r}) \cdot \vec{E}_{inc}(\vec{r}, \omega)}{\int d^2\vec{r} \frac{\vec{K}(\vec{r}) \cdot \vec{K}(\vec{r})}{\sigma(\vec{r}, \omega=0)}}$$

where the term

$$\frac{\epsilon_{avg}(\infty)}{\epsilon_{avg}(\omega)} \omega_p^2$$

accounts for the screening by substrate phonons and the term

$$\frac{\sigma(\omega = 0)}{\tau} \frac{g^2 \omega_{TO}^2}{e^2 \hbar v^2} \frac{2\omega_{TO}}{\omega^2 - \omega_{TO}^2 + i\omega\tau}$$

accounts for the phonon mediated electron electron interaction or the coupling with graphene transverse optical phonons. We fit this equation to our data using the fitting parameter $\gamma = 5 \text{ ps}^{-1}$ and plot the results in figure 5.10

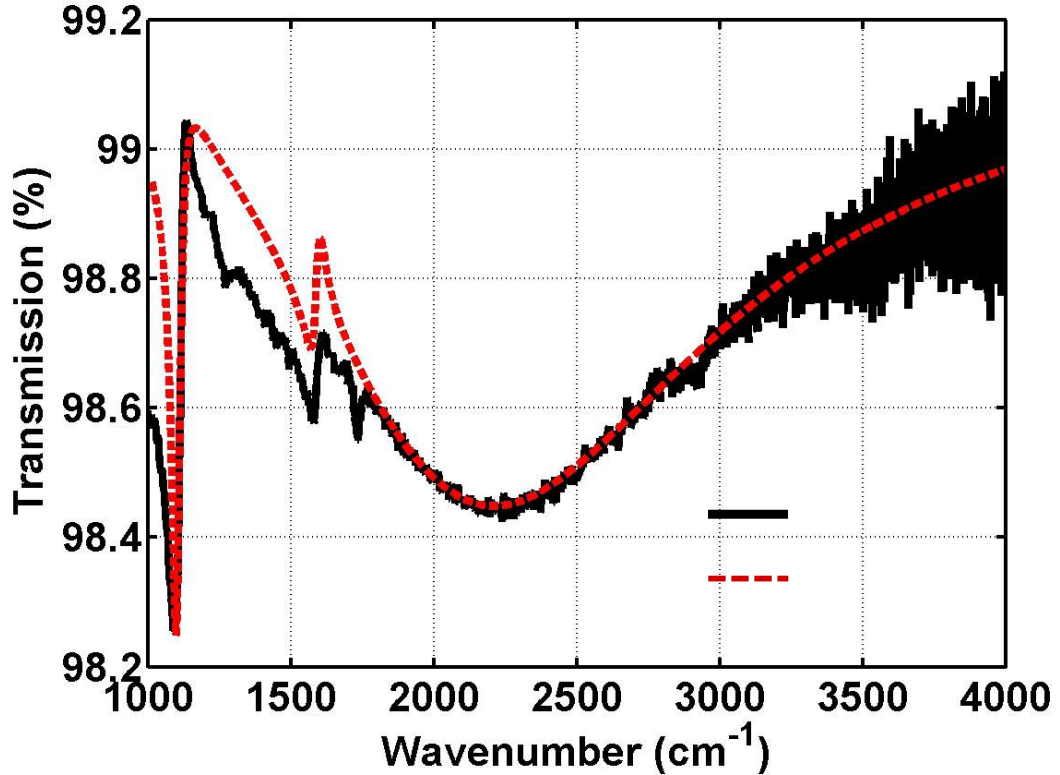


Figure 5.10: Fitting of model including graphene phonon scattering to the absorption spectra of 23nm radius dots. The extracted phonon damping rate is 5 ps^{-1}

Here we have accounted for all the features in our data so we can say that two damping channels that are significant are the phonon mediated electron electron coupling as well as the substrate phonon coupling.

5.5 Phonon Induced Transparency in Graphene

Now we wish to make an observation about the plasmon response equation. When the plasmon resonance frequency matches the graphene optical phonon frequency we obtain

$$(5.29) \quad a_m(\omega) \approx \frac{i}{2\tau} \frac{(\omega - \omega_p) + i\gamma/2}{\left[(\omega - \omega_p) + i\frac{1}{2\tau}\right] \left[(\omega - \omega_p) + i\frac{\gamma}{2}\right] - \frac{\sigma(\omega=0)g^2\omega_T^2}{\tau} \frac{\omega_Q^2}{2e^2\hbar v^2}}$$

The expression for susceptibility in quantum optics for a three level atom interacting with fields of frequency ω_{12} and ω_{13} is given by

$$(5.30) \quad \chi(\omega) \propto \frac{(\omega - \omega_{13} + i\gamma_{12})}{(\omega - \omega_{13} + i\gamma_{13})(\omega - \omega_{13} + i\gamma_{12}) - (\Omega_{23}/2)^2}$$

A cartoon picture of the configuration is shown below

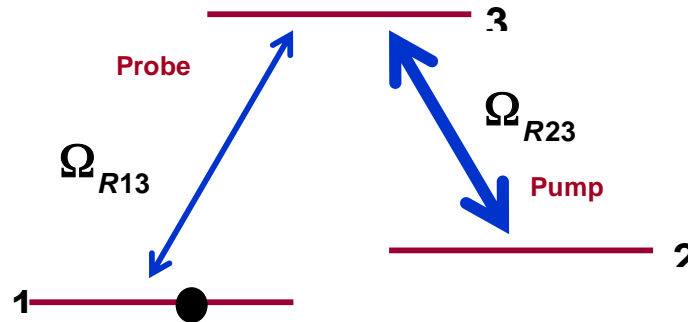


Figure 5.11: Picture showing the 3 level system consisting of graphene phonon oscillator as well as the plasmon oscillator

The figure describes three level system with a strong pump beam that couples level 2 and 3 and a weak probe beam that couples levels 1 and 3. Here Ω_{23} is the Rabi frequency of the laser that couples levels 2 and 3 and γ_{13}, γ_{23} are the linewidths of the 1 to 3 and 2 to 3 transitions respectively. Quantum interference between the two transitions result in the probability amplitude of state 3 to be very small. Comparing the two expressions above we would expect a phonon induced transparency dip in our spectra. We plot the absorption of the graphene dots and we can see this dip in the plasmon response below

where the transparency dip increases as the phonon damping term γ increases and the width increases as the electron phonon coupling term g increases.

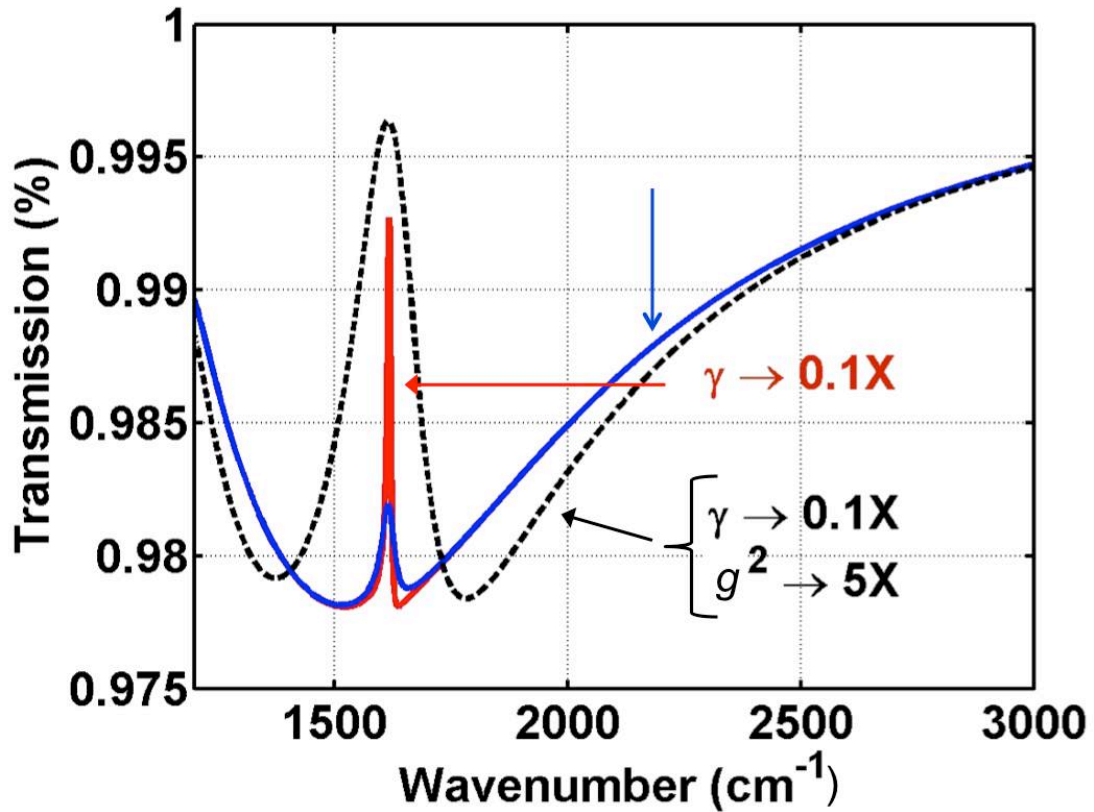


Figure 5.12: Absorption curve of 16nm radius dot, the blue curve is experimental data and the red and black curves are from theory. There is a transparency dip, the damping due to transverse optical phonons γ determines the height and the electron phonon coupling g^2 determines the width.

Finally, we model our data for the 16 nm radius dots and see that it is in good agreement with the experimental data in figure 5.13.

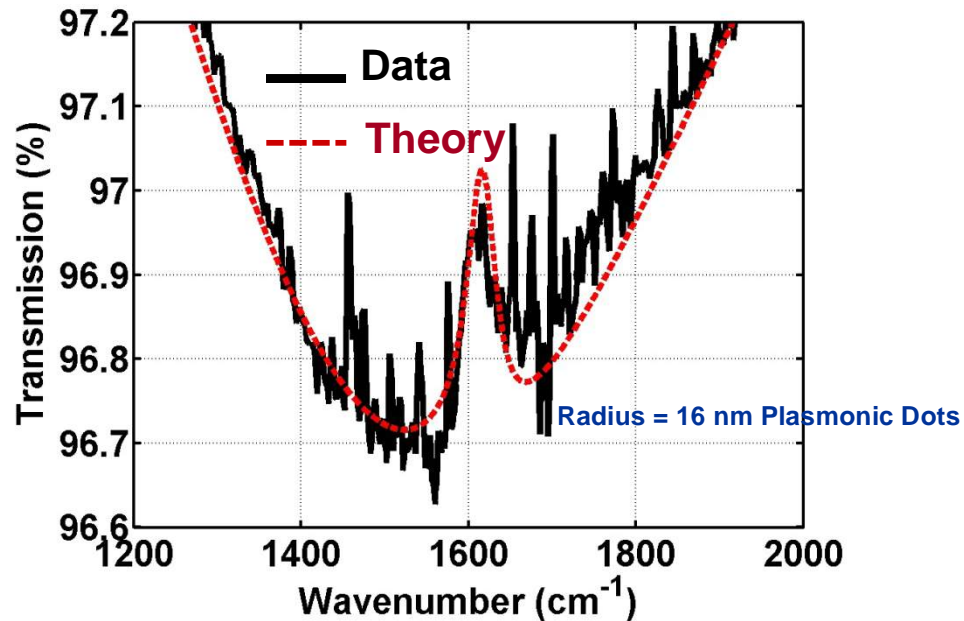


Figure 5.13: Absorption spectra of 16nm radius dots with fitting to the transparency dip. The extracted transverse optical phonon damping time in graphene, γ is 5 ps^{-1} which is shorter than in bulk which is $0.5 - 1 \text{ ps}^{-1}$ maybe due to edge roughness scattering or confinement of the phonons.

5.5 Plasmon modes in graphene due to symmetry breaking

We also examine whether plasmon-phonon collective modes are possible in single or bilayer graphene because from chapter 3 we see that there is a plasmon current in both K and K' valleys and they excite phonons in both valleys with opposite signs. If there is some symmetry they should cancel out but we observe some symmetry breaking in our samples so the current in different valleys are different as shown in the figure 5.14

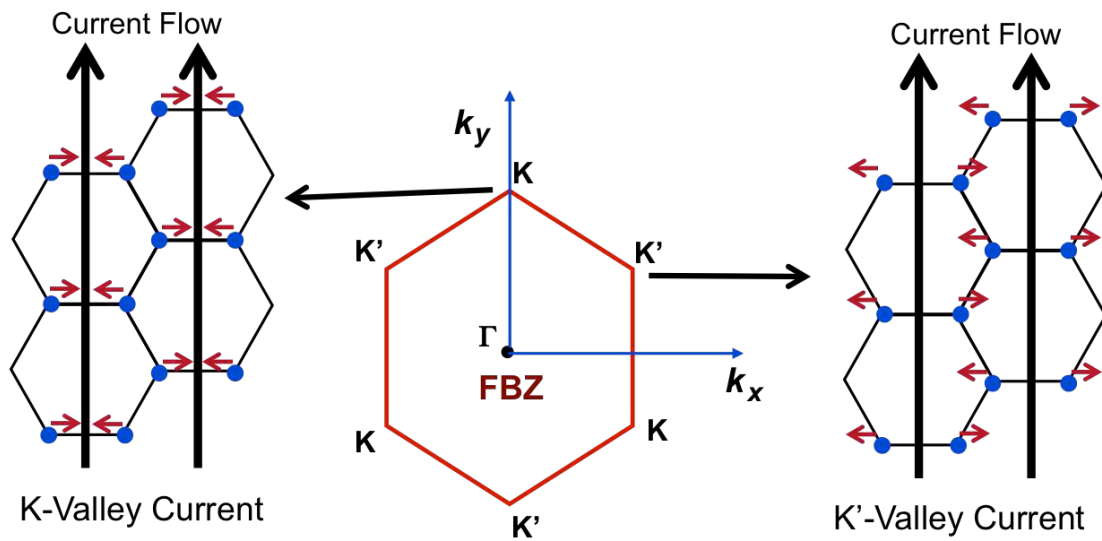


Figure 5.14: Plasmon current in the K and K' valleys in monolayer graphene

We know that one possible origin of this symmetry breaking is by applying an electric field to bilayer graphene. We first quantify the amount of bilayer in our CVD graphene as 10% using an optical image and counting the pixels.

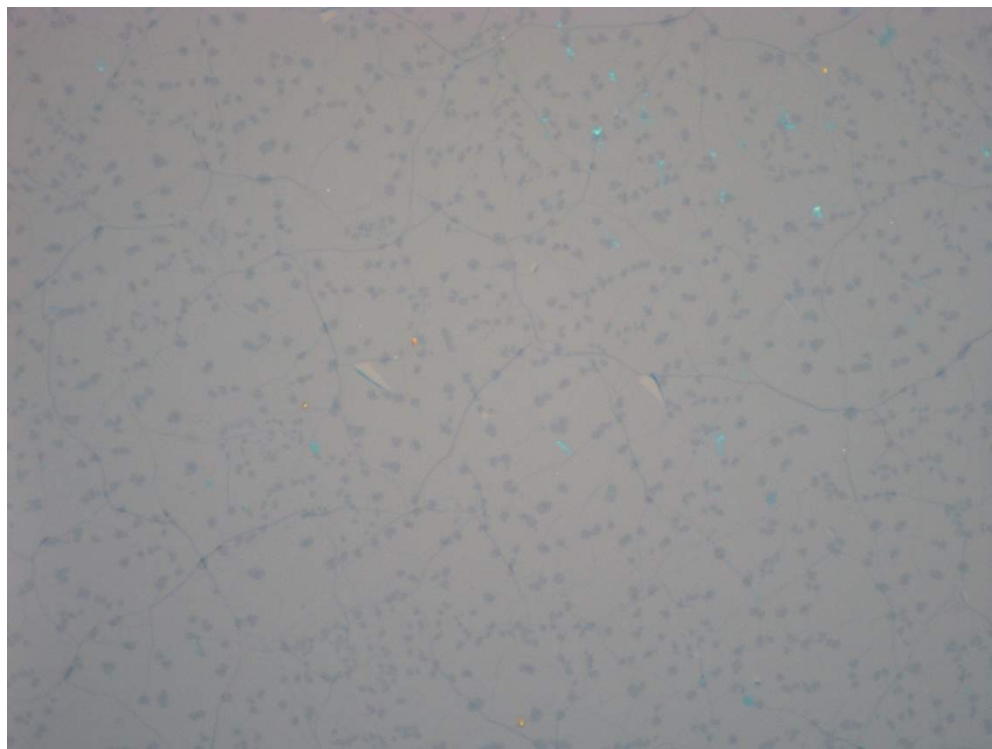


Figure 5.15: Optical image of graphene on 90nm SiO₂. The lighter regions are single layer graphene and the darker areas are bilayer graphene

Next, we repeat the whole experiment using graphene with lower amount of bilayer graphene and plot the data in figures 5.16,

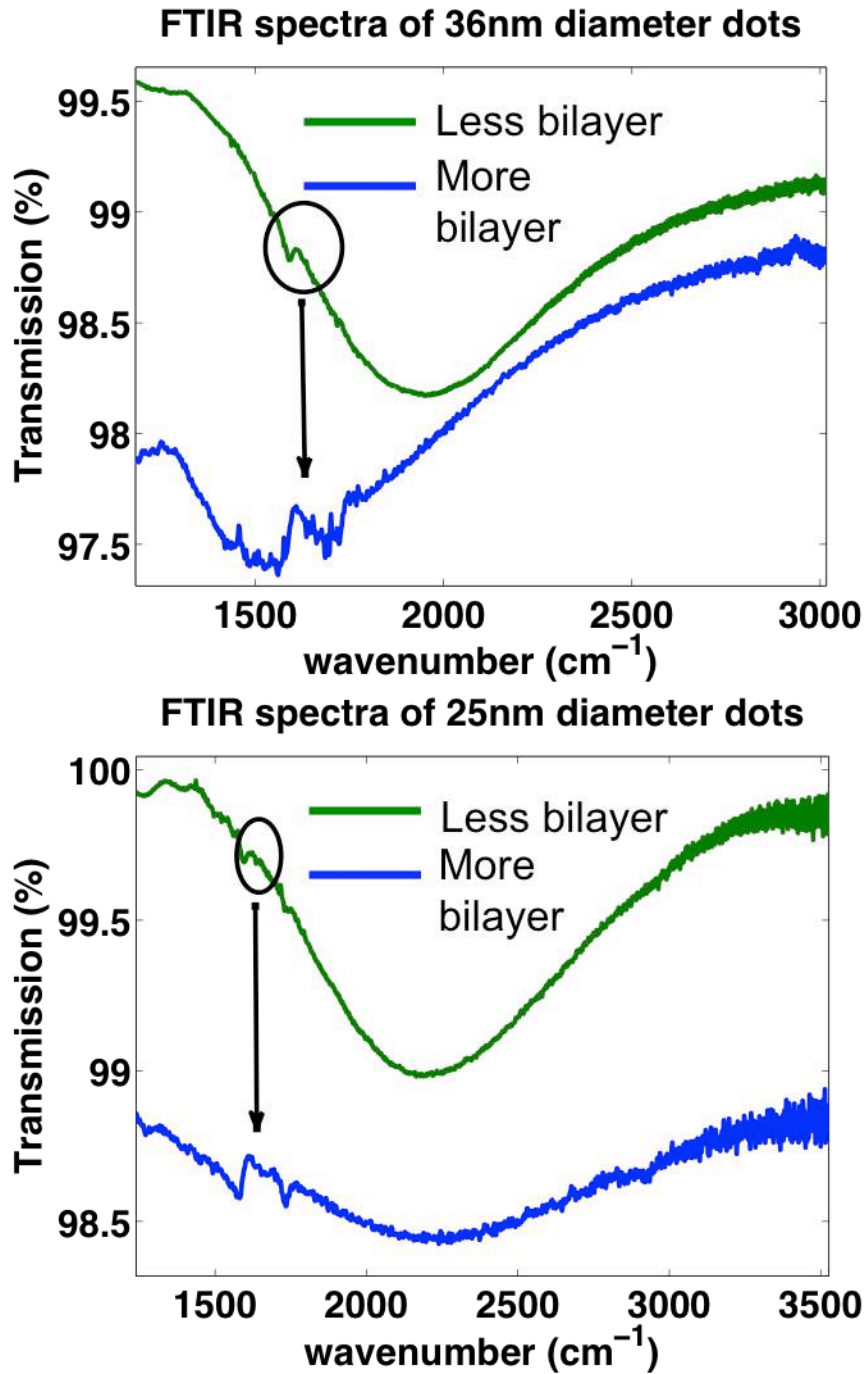


Figure 5.16: The top plot show absorption spectra for 36nm diameter dots and the bottom plot shows absorption spectra for 25nm diameter dots with two different bilayer densities. As the amount of bilayer increases the absorption increases and the features corresponding to the coupling also increase in size

We see that as the amount of bilayer is reduced, the coupling between the graphene plasmons and the optical phonons are reduced as well indicating that the stacking of the layers causes a dipole in the charge distribution breaking the valley symmetry.

In conclusion, we have constructed an eigenvalue equation model for graphene plasmons which agrees well with the measured data. We have also demonstrated self-assembly as a viable route to mid-IR resonator arrays. The coupling of the graphene phonons to the substrate phonons arises due to the dispersion of the optical phonons in silicon oxide and the coupling of graphene plasmons to graphene optical phonons mediates electron electron scattering in graphene plasmons. Finally in the mid-IR region we see that the coupling of the plasmons to the graphene transverse optical phonons gives rise to phonon induced transparency which is a novel phenomenon not previously observed in other materials.

CHAPTER 6

TIME RESOLVED MEASUREMENTS OF MOLYBDENUM DISULPHIDE

6.1 Introduction

During the course of the thesis, frequency resolved spectroscopy was extensively used. However there are some properties that frequency resolved spectroscopy is not suited to, for example if two species were emitting at the same frequency, we would be unable to separate the two. However if their dynamics are different we can use the fact that their relaxation rates will be different to distinguish them. This brings us to time resolved spectroscopy. Several FET devices were fabricated using the methods described in previous chapters for back-gated and temperature dependent pump probe and photoluminescence measurements to understand recombination processes in molybdenum disulphide (MoS_2), however at this point it is not yet clear what the exact mechanisms are, except that Auger recombination is one of them. This is due to the presence of sulfur vacancies in the material and the effect of the SiO_2 interface, which varies even within one sample despite trying to control them via processing[50].

Instead here we try to determine the performance limits of a molybdenum disulphide (MoS_2) photodetector. Monolayer molybdenum disulphide is a 2D material consisting of 3 layers, a layer of molybdenum sandwiched between two layers of sulfur in a trigonal structure. Bulk MoS_2 has an indirect bandgap but Monolayer MoS_2 has a 1.8eV direct bandgap.

6.2 TPCC Measurement

We use the two pulse cross correlation technique (TPCC) first described by Weller at IEDM[51,52]. A ~80-fs, 905-nm (1.37 eV) centre wavelength, optical pulse from a

~83-MHz repetition rate Ti-Sapphire laser is frequency doubled to 452 nm (2.74 eV, ~150 fs) by a beta-BaB₂O₄ crystal, then mechanically chopped at 1.73 KHz and then split into two pulses by a 50/50 beam splitter. The time delay between these two pulses is controlled by a translation stage and the pulses are sent to the metal/MoS₂ junction of the photodetector. The position is chosen based on the position of the schottky junction at the contact.

The measurement setup is shown in figure 6.1. The circuit model shown can be derived from a high-frequency circuit model. If the time-dependent short circuit current response of the illuminated junction to a single optical pulse is $I_1(t)$, and to two optical pulses separated by time Δt is $I_2(t, \Delta t)$, and the external resistance R_{ext} is much larger than the total device resistance, then the measured d.c. voltage $V_c(\Delta t)$ is approximately equal to

$$(6.1) \quad (R_j/T_R) \int I_2(t, \Delta t) dt$$

where T_R is the pulse repetition period, R_j is the resistance of the metal-MoS₂ junction, and the time integral is over one complete period. As the time delay Δt becomes much longer than the duration of $I_1(t)$, one expects $V_c(\Delta t)$ to approach $(2R_j/T_R) \int I_1(t) dt$.

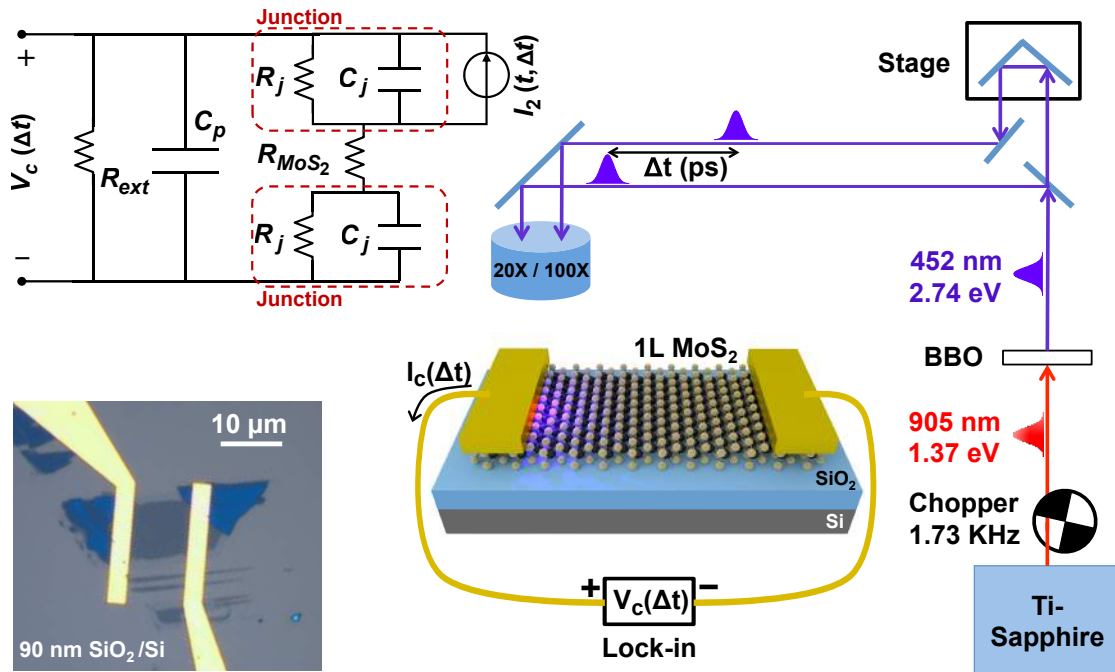


Figure 6.1: Upper left image shows the circuit schematic of the device under measurement. The lower left is an optical microscope image of the fabricated device and the right shows the experimental setup

Figure 6.2(a) shows the measured two-pulse photovoltage correlation signal $V_c(\Delta t)$ plotted as a function of the time delay Δt between the pulses. The substrate temperature is 5 K, the gate bias is 0 V, and the pump fluence is $8 \mu\text{J cm}^{-2}$. $V_c(\Delta t)$ is minimum when the two pulses completely overlap in time (that is, when $\Delta t=0$). This implies, not surprisingly, that the photovoltage response of the detector to an optical pulse is a sublinear function of the optical pulse energy. As Δt increases from zero, $V_c(\Delta t)$ also increases from its minimum value at $\Delta t=0$. As Δt becomes much longer than the duration of the response transient of the detector to an optical pulse, $V_c(\Delta t)$ approaches a constant value. The timescales over which $V_c(\Delta t)$ goes to the constant value are related to the timescales associated with the response transient of the detector to an optical pulse. These timescales are better observed in the measured data if the magnitude of $\Delta V_c(\Delta t)$,

defined as $V_c(\Delta t) - V_c(\infty)$, is plotted on a log log scale, as shown in Fig. 2b. The plot in Fig. 2b shows two distinct timescales: (i) a fast timescale of ~ 4.3 ps and (ii) a slow timescale of ~ 105 ps. In different devices, the fast timescales were found to be in the 3–5 ps range, and the slow timescales were in the 90–110 ps range. The fast timescales imply (8 dB) current modulation bandwidths wider than 300 GHz.

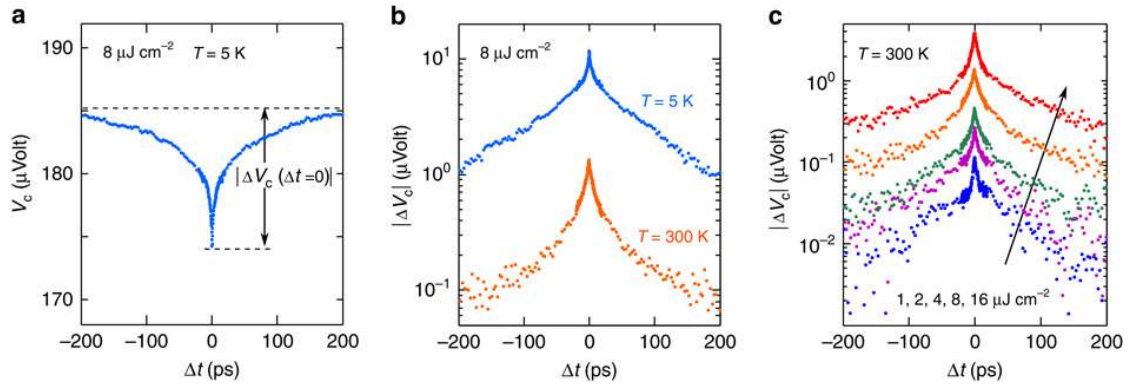


Figure 6.2: (a) The measured two-pulse photovoltage correlation (TPPC) signal $V_c(\Delta t)$ is plotted as a function of the time delay Δt between the pulses. (b) $|\Delta V_c(\Delta t)|$ is plotted on a log scale as a function of the time delay Δt between the pulses to show the two distinct timescales exhibited by $V_c(\Delta t)$. (c) The measured TPPC signal $|\Delta V_c(\Delta t)|$ is plotted as a function of the time delay Δt between the pulses for different pulse fluences: 1, 2, 4, 8 and $16 \mu\text{J cm}^{-2}$

Measurements were performed at different temperatures and using different pump pulse fluences to understand the mechanisms behind the photoresponse and the associated dynamics. The response of the photodetector did not vary significantly based on fluence and temperature. The internal and external detector quantum efficiencies were estimated from the measured values of $V_c(\infty)$ and the junction resistance R_j to be in the 0.008–0.016 and 0.001–0.002 ranges, respectively. The two different timescales observed in our two-pulse photovoltage correlation experiments match well with the two different timescales observed previously in ultrafast optical/THz pump–probe studies of carrier

dynamics as well as in ultrafast photoluminescence studies of MoS₂ monolayers described in the first paragraph.

6.3 Model of MoS₂ Junction

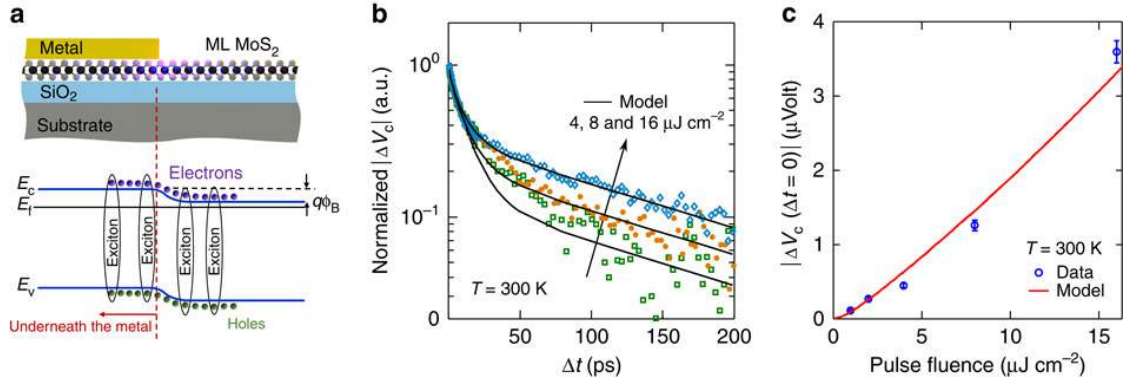


Figure 6.3: (a) Energy band diagram of MoS₂ after excitation with laser pulse. (b) Measured (dots) and computed (solid lines) of photovoltage correlation signal from the photodetector. (c) Measured (dots) and computed (lines) scaling of the photovoltage correlation signal as a function of pump fluence

Figure 6.3(a) depicts the band diagram of the metal-MoS₂ junction (plotted in the plane of the MoS₂ layer) after photoexcitation with an optical pulse. Given the Schottky barrier height of 100–300 meV [53], the width of the MoS₂ region near the metal with a non-zero lateral electric field is estimated to be to ~100–300 nm [54]. As a result of light diffraction from the edge of the metal contact, light scattering from the substrate, and plasmonic guidance, a portion of the MoS₂ layer of length equal to a few hundred nanometres is photoexcited even underneath the metal. In our MoS₂ samples, the carrier mobilities and diffusivities are 2–3 orders of magnitude smaller than in graphene and the time period in which most of the photoexcited carriers recombine and/or are captured by defects is in the few picoseconds range[55]. Assuming similar mobilities and diffusivities of electrons and holes in MoS₂, the photoexcited carriers, both free and bound (excitons), move, either by drift in the junction lateral electric field or by

diffusion, less than ~ 10 nm in 5 ps before they recombine and/or are captured by defects. The photoexcited carrier distributions therefore do not change significantly in space during their lifetime. Separation of electrons and holes either by the junction lateral electric field or at the metal-MoS₂ interface will contribute to the integral $\int I_2(t, \Delta t) dt (\propto V_c(\Delta t))$. We assume that the integral $\int I_2(t, \Delta t) dt$ is approximately proportional to the integral $\int [p'(t, \Delta t) + n'(t, \Delta t)] dt$. Here, $p'(t, \Delta t)$ and $n'(t, \Delta t)$ are the time-dependent photoexcited electron and hole densities in the junction, including carriers both free and bound (excitons). This assumption, although simple, allows one to relate the measured photoresponse to the carrier dynamics and, as shown below, the results thus obtained are in excellent agreement with the experiments.

The strong electron and hole Coulomb interaction in monolayer TMDs makes defect capture via Auger scattering very effective. The time constants observed in this work in the photovoltage correlations are also temperature independent (figure 6.2b) and also match well with the time constants observed previously in optical/THz pump–probe and photoluminescence measurements[56]. We therefore use the model for carrier capture by defects via Auger scattering in MoS₂ published previously to model our TPPC experimental results. After photoexcitation, electrons and holes thermalize and lose most of their energy on a timescale much shorter than our experimental resolution (~ 0.5 – 1.0 ps) and, therefore, thermalization is assumed to happen instantly in our model[57]. Most of the photoexcited holes (both free and bound), followed by most of the electrons, are captured by the fast defects within the first few picoseconds after photoexcitation. During the same period, a small fraction of the holes is also captured

by the slow defects. This rapid capture of the photoexcited electrons and holes is responsible for the fast time constant observed in our photovoltage correlation experiments. The remaining photoexcited electrons are captured by the slow defects on a timescale of 65–80 ps and this slow capture of electrons is responsible for the slow time constant observed in our photovoltage correlation experiments. We should point out here that the two time constants observed in the photovoltage correlation signal $\Delta V_c(\Delta t)$ are always slightly longer than the corresponding two time constants exhibited by the carrier densities in direct optical pump–probe and measurements, as is to be expected in the case of correlation measurements. Finally, the superlinear dependence of the carrier capture rates on the photoexcited carrier densities in the model, and therefore on the optical pulse energy, results in the experimentally observed negative value of the photovoltage correlation signal $\Delta V_c(\Delta t=0)$ at zero time delay. The comparison between the data and the model are shown in figure 6.3(b) which plots the measured and computed photovoltage correlation $|\Delta V_c(\Delta t)|$ as a function of the time delay Δt for different pump fluence values: 4, 8 and 16 $\mu\text{J cm}^{-2}$

6.4 Conclusion

In most semiconductor photovoltaic detectors with large carrier mobilities and long recombination times (for example, group III–V semiconductor photodetectors[58]), the transit time of the photogenerated carriers through the junction depletion region determines the detector bandwidth[58]. Given the relatively small carrier mobilities and diffusivities in MoS₂, the fast carrier recombination times determine the speed in our metal-MoS₂ detectors. The price paid for the the fast response time is the small internal quantum efficiency: most of the photogenerated carriers recombine before they make it

out into the circuit. We expect that by better controlling the defects in our devices we should be able to obtain photodetectors with higher quantum efficiency.

BIBLIOGRAPHY

- [1] Clemens J. Först, Christopher R. Ashman, Karlheinz Schwarz & Peter E. Blöchl, The interface between silicon and a high-k oxide, *Nature* **427**, 53-56 (1 January 2004)
- [2] Tennant, D. M. in *Nanotechnology* (ed. Timp, G.) Ch. 4, 161–205 (Springer, 1999).
- [3] Chau, R., Doyle, B., Datta, S., Kavalieros, J. & Zhang, K. Integrated nanoelectronics for the future. *Nature Mater.* 6, 810–812 (2007).
- [4] Christian Wagner & Noreen Harned, EUV lithography: Lithography gets extreme, *Nature Photonics* 4, 24 - 26 (2010)
- [5] Density Multiplication and Improved Lithography by Directed Block Copolymer Assembly, Ricardo Ruiz, Huiman Kang, François A. Detcheverry, Elizabeth Dobisz, Dan S. Kercher, Thomas R. Albrecht, Juan J. de Pablo, and Paul F. Nealey, *Science* 15 August 2008: 321 (5891), 936-939.
- [6] Rachel A. Segalman, Patterning with block copolymer thin films, *Materials Science and Engineering: R: Reports*, Volume 48, Issue 6, 28 February 2005, Pages 191–226
- [7] Controlling Polymer-Surface Interactions with Random Copolymer Brushes; P. Mansky, Y. Liu, E. Huang, T.P. Russell, C. Hawker. *Science* 275, 1458-1460 (1997)
- [8] Pattern coarsening in a 2D hexagonal system; C. Harrison, D.E. Angelescu, M. Trawick, Zhendong Cheng, D.A. Huse, P.M. Chaikin, D.A. Vega, J.M. Sebastian, R.A. Register and DH Adamson, *Europhysics Letters* 67 (5)
- [9] Effect of structural anisotropy on the coarsening kinetics of diblock copolymer striped patterns”; R. Ruiz, J. K. Bosworth and C. T. Black, *Physical Review B* 77, 054204(2008)
- [10] Epitaxial self-assembly of block copolymers on lithographically defined nanopatterned substrates”; Sang Ouk Kim, Harun H. Solak, Mark P. Stoykovich, Nicola J. Ferrier, Juan J. de Pablo, and Paul F. Nealey, *Nature* 424, 411-414 (24 July 2003).
- [11] Polymer self assembly in semiconductor microelectronics, Black C.T., Ruiz, R. Breyta, G, Cheng, J.Y., *IBM Journal of Research and Development* (Volume 51, Issue 5)
- [12] Lee, J.-K.; Chatzichristidi, M.; Zakhidov, A. A.; Taylor, P. G.; DeFranco, J. A.; Hwang, H. S.; Fong, H. H.; Holmes, A. B.; Malliaras, G. G.; Ober, C. K., Acid-sensitive semiperfluoroalkyl resorcinarene: an imaging material for organic electronics. *J. Am. Chem. Soc.* 2008, 130, 11564-11565.
- [13] Directed Patterning for Electronics Using Multiple Block Copolymers Orthogonally, Wei Min Chan, Sandip Tiwari, Evan Schwartz and Christopher Ober, Cornell University, EIPBN 2012, Session 10
- [14] Tight-binding description of graphene, S. Reich, J. Maultzsch and C. Thomsen, *Phys Rev B* 66, 035412 (2002)
- [15] V. N. Popov and Ph. Lambin, *Phys. Rev. B* **73** (2006) 085407.

- [16] Andrew Kozbial, Zhiting Li, Caitlyn Conaway, Rebecca McGinley, Shonali Dhingra, Vahid Vahdat, Feng Zhou, Brian D'Urso, Haitao Liu, and Lei Li, *Langmuir*, 2014, 30 (28), pp 8598–8606
- [17] The origins and limits of metal–graphene junction resistance Fengnian Xia, Vasili Perebeinos, Yu-ming Lin, Yanqing Wu and Phaedon Avouris, *Nature Nanotechnology* 6, 179–184 (2011)
- [18] Making graphene visible, P. Blake, E.W. Hill, A.H. Castro Neto, K.S. Novoselov, D. Jiang, R. Yang, T.J. Booth, and A.K. Geim, *Applied Physics Letters* 91, 063124 (2007)
- [19] Large-Area Synthesis of High Quality and Uniform Graphene Films on Copper Foils, Xuesong Li, et al. *Science* 324, 1312 (2009)
- [20] Andrea C. Ferrari & Denis M. Basko, *Nature Nanotechnology* 8, 235–246 (2013)
- [21] Graphene Field-Effect Transistors with High On/Off Current Ratio and Large Transport Band Gap at Room Temperature, Fengnian Xia, Damon B. Farmer, Yu-ming Lin and Phaedon Avouris, *Nano Lett.*, 2010, 10 (2), pp 715–718
- [22] Realization of a high mobility dual-gated graphene field-effect transistor with Al₂O₃ dielectric, Seyoung Kim, Junghyo Nah, Insun Jo, Davood Shahrjerdi, Luigi Colombo, Zhen Yao, Emanuel Tutuc and Sanjay K. Banerjee, *Appl. Phys. Lett.* 94, 062107 (2009);
- [23] Graphene Terahertz Plasmon Oscillators, F Rana, *IEEE TRANSACTIONS ON NANOTECHNOLOGY*, VOL. 7, NO. 1, JANUARY 2008
- [24] Controlling inelastic light scattering quantum pathways in graphene, Chi-Fan Chen, *Nature* 471, 617–620 (31 March 2011)
- [25] Chemical Doping of Large-Area Stacked Graphene Films for Use as Transparent, Conducting Electrodes, Amal Kasry et al, *ACS Nano*, 2010, 4 (7), pp 3839–3844
- [26] J. H. Strait, P. A. George, M. Levendorf, M. Blood-Forsythe, F. Rana, and J. Park, *Nano Letters* 9, 2967 (2009).
- [27] E. H. Hwang and S. Das Sarma, *Phys. Rev. B* 75, 205418 (2007)
- [28] J. M. Dawlaty, S. Shivaraman, J. Strait, P. George, M. Chandrashekar, F. Rana, M. G. Spencer, D. Veksler, and Y. Chen, *Applied Physics Letters* 93, 131905 (2008)
- [29] A. Taflove and S. C. Hagness (Artech House, 2005), 3rd ed., ISBN 1-58053-832-0
- [30] J. L. Tomaino et al *Opt. Express* 19, 141 (2011).
- [31] S. Thongrattanasiri, F. H. L. Koppens, and F. J. Garcia de Abajo, *Phys Rev. Lett.* 108, 047401 (2012).
- [32] D. Mittleman, ed., *Sensing with Terahertz Radiation*, 1st ed. (Springer-Verlag, 2003) pp. 39, 107.
- [33] L. Ju, B. Geng, J. Horng, C. Girit, M. Martin, Z. Hao, H. A. Bechtel, X. Liang, A. Zettl, Y. R. Shen, and F. Wang, *Nat Nano* 6, 630 (2011).

- [34] H. Yan, T. Low, W. Zhu, Y. Wu, M. Freitag, X. Li, F. Guinea, P. Avouris, and F. Xia, *Nat Photon* 7, 394 (2013).
- [35] Z. Fang, Y. Wang, Z. Liu, A. Schlather, P. M. Ajayan, F. H. L. Koppens, P. Nordlander, and N. J. Halas, *ACS Nano* 6, 10222 (2012)
- [36] V. W. Brar, M. S. Jang, M. Sherrott, J. J. Lopez, and H. A. Atwater, *Nano Letters* 13, 2541 (2013)
- [37] Y. Liu, R. Cheng, L. Liao, H. Zhou, J. Bai, G. Liu, L. Liu, Y. Huang, and X. Duan, *Nat Commun* 2, 579 (2011)
- [38] D. E. Johnston, M. Lu, and C. T. Black, *Journal of Micro/Nanolithography, MEMS, and MOEMS* 11, 031306 (2012)
- [39] V. G. Kravets, et al, *Sci. Rep.* 4 (2014).
- [40] V. W. Brar, et al, *arXiv* (2014), arXiv:1405.4145 [cond-mat.mes-hall].
- [41] A. Principi, M. Carrega, M. B. Lundeberg, A. Woessner, F. H. L. Koppens, G. Vignale, and M. Polini, *Phys. Rev. B* 90, 165408 (2014)
- [42] S. Das Sarma, S. Adam, E. H. Hwang, and E. Rossi, *Rev. Mod. Phys.* 83, 407 (2011).
- [43] J.-H. Chen, W. G. Cullen, C. Jang, M. S. Fuhrer, and E. D. Williams, *Phys. Rev. Lett.* 102, 236805 (2009).
- [44] T. Fang, A. Konar, H. Xing, and D. Jena, *Phys. Rev. B* 78, 205403 (2008).
- [45] P. Nene, J. H. Strait, W.-M. Chan, C. Manolatou, S. Tiwari, P. L. McEuen, and F. Rana, *Applied Physics Letters* 105, 143108 (2014)
- [46] H. J. Dai, N. P. Balsara, B. A. Garetz, and M. C. Newstein, *Phys. Rev. Lett.* 77, 3677 (1996)
- [47] Feliciano Giustino, EPFL thesis (2005)
- [48] Lifetimes of optical phonons in graphene and graphite by time-resolved incoherent anti-Stokes Raman scattering, Kwangu Kang, Daner Abdula, David G. Cahill, and Moonsub Shim, *Phys. Rev. B* 81, 165405
- [49] Hugen Yan et al, *Phys. Rev. B* 80, 121403(R)
- [50] Absorption of light by excitons and trions in monolayers of metal dichalcogenide MoS₂: Experiments and theory, Changjian Zhang, Haining Wang, Weimin Chan, Christina Manolatou, and Farhan Rana *Phys. Rev. B* 89, 205436
- [51] Picosecond Optical Autocorrelation Experiments on Fast Photodetectors, T.F. Carruthers and J.F. Weller, *IEDM* 1985
- [52] 2 ps InGaAs photoconductors and their speed-of-response evaluation by optical pulse mixing at inherent nonlinearities, R. Loepfe et al, *Appl. Phys. Lett.* 52, 2130 (1988)
- [53] Sundaram, R. S. *et al.* Electroluminescence in single layer MoS₂. *Nano Lett.* 13, 1416–1421 (2013)
- [54] Petrosyan, S. G. & Shik, A. Ya. Contact phenomena in low-dimensional electron systems. *Zh. Eksp. Teor. Fiz.* 69, 1261 (1989)
- [55] Wang, H. *et al.* Fast exciton annihilation by capture of electrons or holes by defects via Auger scattering in monolayer metal dichalcogenides. *Phys. Rev. B* 91, 165411 (2015)

- [56] Wang, H., Zhang, C. & Rana, F. Ultrafast dynamics of defect-assisted electron-hole recombination in monolayer MoS₂. *Nano Lett.* 15, 339–345 (2015)
- [57] Kaasbjerg, K., Bhargavi, K. S. & Kubakaddi, S. S. Hot-electron cooling by acoustic and optical phonons in monolayers of MoS₂ and other transition-metal dichalcogenides. *Phys. Rev. B* 90, 165436 (2014) .
- [58] Donati, S. *Photodetectors: Devices, Circuits and Applications* 1st ed. Prentice Hall (1999)